CantiClever
Planar fabrication of probes for magnetic imaging

Promotiecommissie

Voorzitter, secretaris:	Prof. dr. W.H.M. Zijm	Universiteit Twente, EWI
Promotor:	Prof. dr. J.C. Lodder	Universiteit Twente, EWI
Assistent promotor:	Dr. ir. L. Abelmann	Universiteit Twente, EWI
Leden:	Prof. dr. M.C. Elwenspoek	Universiteit Twente, EWI
	Dr. ir. H.J.W. Zandvliet	Universiteit Twente, TNW
	Prof. dr. C.D. Wright	University of Exeter, UK
	Prof. dr. J. de Boeck	IMEC, Technische Universiteit Delft

The research described in this thesis was funded by the Dutch Technology Foundation (STW) project TEL. 4562, ”Magnetic field probe microscope for research, development and production of magnetic recording media and heads”. The research was carried out at the Systems and Materials for Information storage group (SMI) of the MESA$^+$ research institute at the University of Twente.

Twente University **Press**

Publisher:
Twente University Press,
P.O. Box 217, 7500 AE Enschede, the Netherlands,
http://www.tup.utwente.nl

Cover design:
The cover shows a row of CantiClever probes,
with an MFM image of a hard disk medium on the background,
measured with the CantiClever probe.
The photograph of the probes was taken by Casper Doppen.

Print: Océ Facility Services, Enschede

© A.G. van den Bos, Enschede, 2003
No part of this work may be reproduced by print,
photocopy or any other means without the permission
in writing from the publisher.

ISBN 90-365-1988-8

CantiClever
Planar fabrication of probes for magnetic imaging

PROEFSCHRIFT

ter verkrijging van
de graad van doctor aan de Universiteit Twente,
op gezag van de rector magnificus,
Prof. dr. F.A. van Vught,
volgens het besluit van het College voor Promoties
in het openbaar te verdedigen
op vrijdag 14 november 2003 om 15.00 uur

door

Arnout Gerbrand van den Bos

geboren op 10 december 1974

te Oosterhout (NB)

Dit proefschrift is goedgekeurd door

de promotor:	Prof. dr. J.C. Lodder
de assistent promotor:	Dr. ir. L. Abelmann

Contents

Chapter 1

Introduction

This introductory chapter is meant to provide a background of the research presented in this thesis. It starts with an overview of the field of scanning probe technology and its applications, and concludes with the outline of the thesis.

1.1 Scanning probe microscopy

A scanning probe microscope has four unique elements compared to other microscopes. First, the use of a very small tip, that is kept close to the surface of the sample that is being investigated; second, a property of the sample surface is detected that changes rapidly in proximity of the surface, such as forces or a tunnelling current; third, the use of a feedback system to control the distance or contact between the tip and the sample; and fourth the ability to move the tip over the sample surface with very high (less than 1 nm) resolution.

The first successful scanning probe microscope was the Topografiner, developed by Young *et al.* between 1966 and 1971 [1], shown schematically in figure 1.1. A constant tip to sample distance was maintained by a feedback system that adjusted the voltage on the vertical piezo, thereby moving the tip (called emitter in figure 1.1) up and down. Piezos mounted in the x– and y–direction deflected a flexible post on which the tip was mounted, providing the scanning motion in the sample plane. No computerized data acquisition systems were available at that time, so the data was acquired with a x–y recorder and a storage oscilloscope. One of the results is depicted in figure 1.1. The estimated resolution was 3 nm in the vertical direction, and 400 nm in the plane.

Besides images taken using field emission, also initial metal–vacuum–metal tunnelling experiments were carried out with the Topografiner. However, due to instabilities in the feedback loop and noise due to poor vibration isolation, the instrument was not able to take any images of surfaces using direct tunnelling. Such an instrument, the Scanning Tunnelling Microscope (STM), was invented

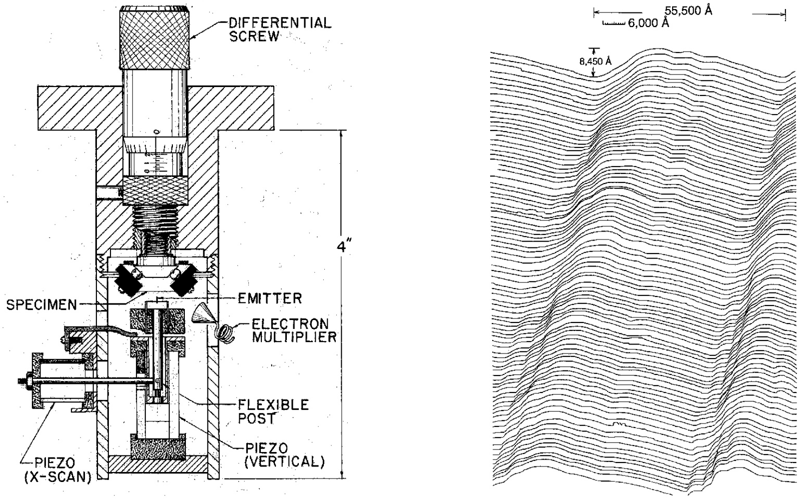

Figure 1.1: *Left: schematic drawing of the Topografiner. Right: Topographic map of a 180 lines per mm diffraction grating replica, obtained with the Topografiner. Taken from [1].*

in 1982 by Binnig *et al.*. Using their STM, they presented topographic images of $CaIrSn_4$, gold [2] and silicon [3] surfaces with atomic resolution for the first time. For this invention, Gerd Binnig and Heinrich Röhrer were awarded with the Nobel prize in Physics in 1986.

The STM was capable of resolving the surface structure with atomic resolution, but only on conducting samples. An instrument that could image the surface of insulating samples with very high resolution, the Atomic Force Microscope, was presented a few years later by Binnig, Quate and Gerber, in 1986 [4]. The first AFM used a gold foil as a cantilever spring on which a diamond tip was glued. The deflection of the cantilever was detected with an STM. This resulted in a vertical resolution of less than 1 Å and a lateral resolution of 30 Å. In later AFM's the STM was replaced by optical systems to detect the deflection of the cantilever [5]. It was not until 1992 that AFM with true atomic resolution was demonstrated [6].

1.1.1 Magnetic force microscopy

Binnig *et al.* envisioned that their AFM would be modified to measure other forces near sample surfaces, such as magnetic forces [4]. These modifications were carried out by Martin *et al.* [7] and Saenz *et al.* [8] in 1987, who almost simultaneously invented the Magnetic Force Microscope (MFM) that can de-

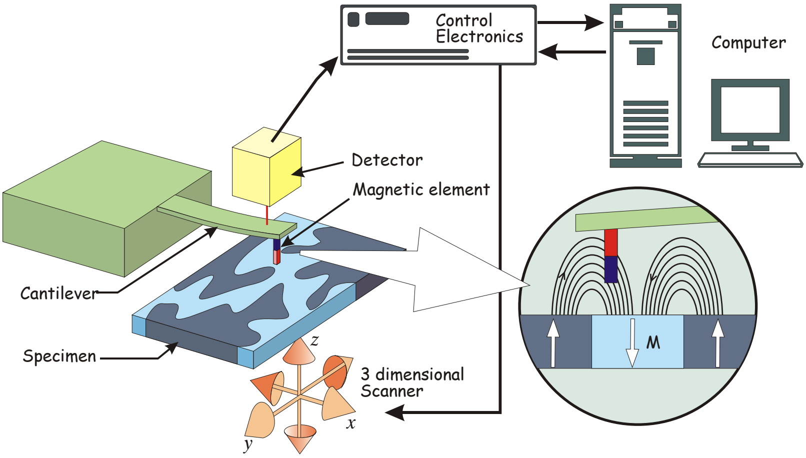

Figure 1.2: *Principle of magnetic force microscopy. The inset shows the stray field of the sample and the magnetization of the tip.*

tect magnetic forces above a very flat sample. This is done by placing a small magnetic tip, mounted on a cantilever spring, very close to the surface of the sample. The interaction between the stray field of the sample and that of the tip makes that the tip is either attracted or repelled by the sample. The resulting force on the tip can be detected by measuring the displacement of the end of the cantilever, usually by optical means. The principle of MFM is schematically depicted in figure 1.2, showing the computer used for data aquisition, the control electronics, the optical displacement detector and the cantilever with the magnetic tip scanning over the sample. The dark areas on the sample have a magnetization pointing upwards, the brighter areas downwards. The cantilever is usually around 200 μm in length, equipped with a tip that is 4 μm long and 50 nm in diameter. The distance between the tip and the sample surface is around 30 nm. The forces measured in typical MFM applications are in the order of 30 pN, with typical cantilever deflections on the order of nanometers. An image of the magnetic stray field is obtained by slowly scanning the cantilever over the sample surface, in a raster–like fashion. Typical scan areas are from 1 up to 200 μm with imaging times in the order of 5 to 30 minutes.

Compared to other techniques that can be used to image magnetic stray fields with very high resolution, such as Lorentz microscopy [9] or spin polarized STM [10], MFM has the advantage that it is a non–destructive technique that doesn’t require exhaustive sample preparation or extremely clean surfaces. Because of these properties, and because MFM is a relatively cheap technique, the MFM is widely used in the magnetic recording industry. Moreover, in magnetic recording the media and heads are designed in such a way that the surfaces are very smooth and the external stray fields are very high. Also, the recording media are very resistant to the influence of external fields, so tip/sample interaction is not really a problem. All these aspects make MFM the method of choice. It is therefore not coincidental that reference samples for MFM originate from the magnetic recording community (such as the NIST hard disk [11] or the magneto–optic disk used for the CAMST reference sample [12]).

1.2 Probe recording

The magnetic recording industry has come a long way since the introduction of the first hard disk, the IBM RAMAC (Random Access Method of Accounting and Control), in 1956. This system could store 5 MB of information on fifty 24–inch discs, giving it an areal density of 2 kilobits per square inch. Present day hard disks have an areal density of around 30 Gb/inch^2, a nearly 16 million time increase in areal density. Even higher areal densities have been shown in several laboratory demos. Recently a 145 Gb/inch^2 areal density has been shown [13]. The development of the hard disk is illustrated in figure 1.3. From this figure can be seen that the roadmap for development of hard disk systems is very steep. The areal density growth rate increased from 25% per year in the early eighties up to 100% per year nowadays.

1.2.1 Limits of hard disk systems

It is not certain however, that the incredible areal density growth rate of hard disks will continue in the next decade. To do so, the hard disk industry has to overcome several limitations present in current hard disk systems. The most widely known limitation is that caused by the so–called superparamagnetic effect. This effect poses a fundamental limit to the areal density that can be achieved. If the density is increased above this limit, the magnetic grains, 100 of these grains make up a single bit, become so small that they become thermally unstable and the information stored is lost. Several tricks are already being applied in commercial products to solve this problem such as Anti Ferromagnetically Coupled (AFC) media [15]. Further down the road, options such as perpendicular recording [16, 17], heat assisted recording [18] or the use of patterned media, where the magnetic layer is patterned in a regular matrix of dots [19, 20], may be applied to push the superparamagnetic limit to higher recording densities. That this process is already going on can be seen from figure 1.3: the lab demos and even the commercial available hard disks have an areal density that lies in the 'super paramagnetic effect' zone.

Other limitations are access time and data rate. Whereas the areal density increases with 100% per year, the access time decreases by only 7% per year [14].

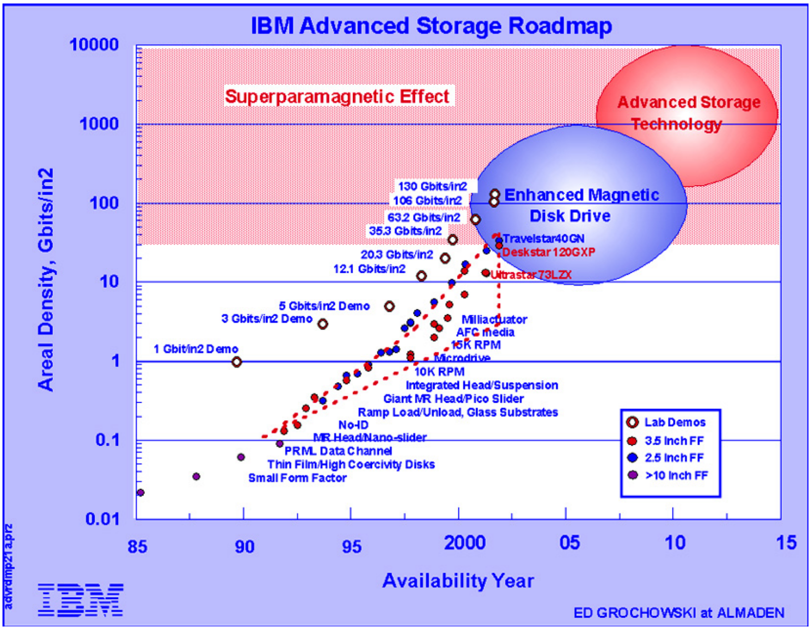

Figure 1.3: *Development of IBM hard disks since 1985. The white dots mark the lab demos and the black and gray dots commercial products. Taken from [14].*

This is caused by the fact that the conventional (Winchester–type) hard drive has only one head per disk. The access time is determined by the time it takes to move the head to the required radial position on the disk and the rotational speed of the disk. The latter of the two is dominant; a state of the art hard disk that spins at 15,000 rpm has an average rotational latency of 2 ms. To decrease the access time one must increase the rotational speed. Because latency and data rate are coupled, this also increases the data rate. The read and write heads must be capable to deal with these high speeds. The finite rise and fall times of the heads will limit the maximum rotational speed. Mechanical issues such as bearings and motor vibrations and other issues such as heat, power consumption and noise will prevent an unlimited increase of the rotational speed. A solution to this problem is to decouple the access time and the data rate. This requires a completely different architecture. A probe recording system is an example of such an architecture that might provide a solution to the limitations in density, latency and data rate of current hard disk systems. A probe recording system may very well be part of the "advanced storage systems" that successes the hard disk drive as pictured in figure 1.3.

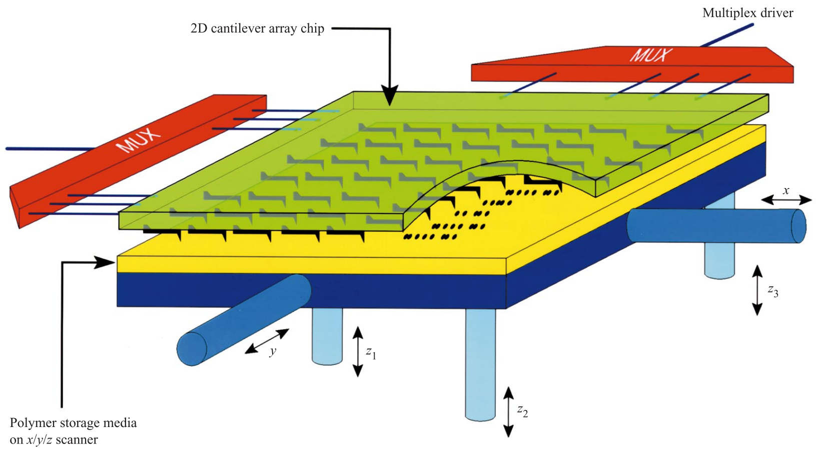

Figure 1.4: *General concept of a probe recording system, in this case that of the Millipede. The probe array (2D cantilever chip), the (polymer) storage medium, the displacement actuator and the electronics (MUX) are shown. Taken from [21].*

1.2.2 Probe recording systems

The general concept of all probe recording systems is depicted in figure 1.4. Four main components can be identified: the 2D array of read/write heads (probes), the medium, the array displacement actuator that moves the medium and the electronics needed for control, multiplexing and data channel. In contrast to the hard disk drive, where one recording head needs to address the complete media, in a probe recording system numerous probes each address only a small area of the medium. The distance the probe array needs to move to address the complete medium is approximately equal to the distance between the probes in the array. This is a very small distance compared to the distance the head in a hard disk needs to move. Not only does the use of a probe array greatly reduce the latency, it also decouples the latency from the data rate. Now it is possible to seek the data very fast and read at lower speeds. The use of a probe array has another advantage: by making use of the huge parallelism that can be achieved by using thousands of probes simultaneously, high data rates can be reached while the data rate per probe is relatively low. This parallelism will be a requirement for a probe recording system to be successful, as the data rate per probe is liable to be low, limited by the resonance frequency of the probes.

The best developed probe recording system at the moment is the Millipede from IBM [21, 22, 23]. The Millipede uses a thermomechanical writing scheme, where small pits are melted in a polymer [24]. The probes consist of a highly

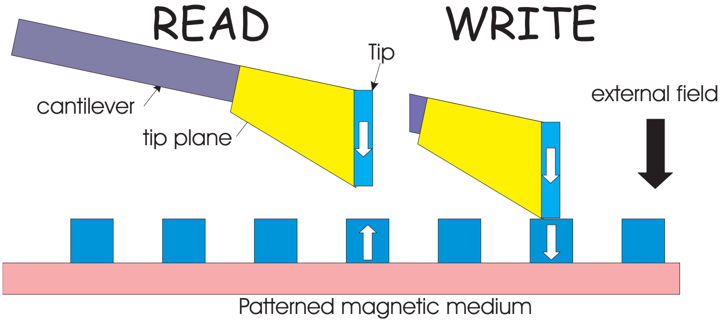

Figure 1.5: *Reading and writing in MFM mode on a patterned magnetic medium.*

conducting cantilever and a resistive area (the heater) with very sharp tip on top [25]. When the tip is brought into contact with the medium, a small force is applied and the tip is heated. This combination causes an indentation to be made into the medium. The data is read back by measuring the thermal conductance between the heater and the medium. The thermal conductance increases when the tip “sinks” into an indentation. Erasing can be done by heating the complete medium, erasing all the bits at the same time, or by heating a row of bits, by writing a bit just adjacent to the bit to be erased. At the end of the row, only one will remain. With the Millipede, bit densities as high as 200 Gb/inch^2 are demonstrated at a data rate of 1 kb/s per tip [23]. As this low data rate is not due to fundamental limits, data rates of several megabits per second are estimated in the future [26]. In reading and writing experiments with a single lever, reading speeds up to a few Mb/s and writing speeds of 100 kb/s have been achieved, while the maximum density, although achieved at lower speeds, lies currently around 1 Tb/inch^2 [23].

Also probe recording systems using a magnetic medium are being investigated by Carley *et al.* at the Carnegie Mellon University [27, 28, 29, 30] and by the SMI group at the University of Twente. The medium of such systems would be a continuous medium as developed at CMU or a patterned medium with perpendicular anisotropy as developed by the SMI group. Reading and writing of bits on a patterned medium was first demonstrated by Kong *et al.* in 1997, who could write bits using an MFM tip at a density of 7.5 Gb/inch^2 in an array of soft–magnetic nickel bars [31]. This is an example of MFM probe recording, as depicted in figure 1.5. When the tip is reading the bits from the medium, the tip is kept at a certain height above the magnetic dot, and the system operates in the same way an MFM does. For writing, the tip is brought close or in contact with the dot. Subsequently, an external field is applied such, that this field alone is not sufficient to switch the magnetization of the highly coercive dot. However,

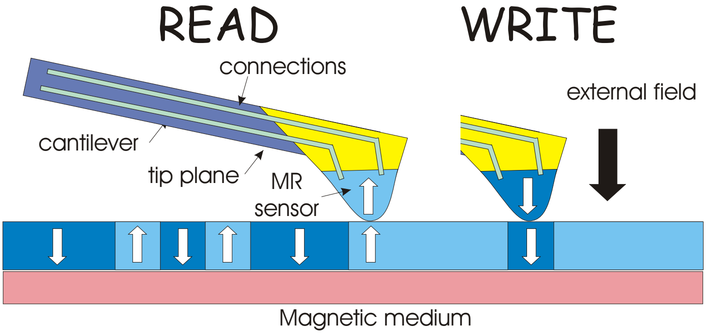

Figure 1.6: *Reading and writing in MRM mode.*

the sum of the stray field from the tip and the external field is sufficiently high to switch the magnetization of the dot under the tip, while all other dots don't switch.

Another way of reading and writing in a magnetic probe recording system is the Magneto Resistive Microscopy (MRM) mode, as depicted in figure 1.6. In this mode, an MR sensor, integrated on the probe, is used to read the magnetization direction of the dots. When writing, an external field is applied and the magnetically soft MR sensor is used as a flux guide, locally increasing the magnetic field, thereby switching the magnetization of the dot under the tip. The MRM mode has the advantage that the probes can run at a constant height (or even in contact) with the medium. This doesn't require complex systems to control and vary the tip to sample distance per probe. Moreover, as the data rate is not limited in this case by the resonance frequency of the probes, the data rates per tip can be much higher compared to operation in MFM mode [27]. An example of such a system is the micro Scanning Probe Array Memory (μSPAM), that is being developed at the University of Twente [32]. A schematic drawing is shown in figure 1.7. The tip array and the tile holding the medium can be seen, along with an MFM image of a real patterned medium. Interesting to note is that the medium tile consists of a number of small media, that can be moved independently from each other. This provides additional flexibility regarding access time, data rate, power consumption and concurrency.

1.3 Motivation and outline of the thesis

As discussed in the previous section, the magnetic recording industry is on an incredible steep roadmap. The MFM is a very powerful imaging technique that greatly contributes to the development of both heads and media. With increasing areal density, the MFM must be capable of resolving ever smaller magnetic

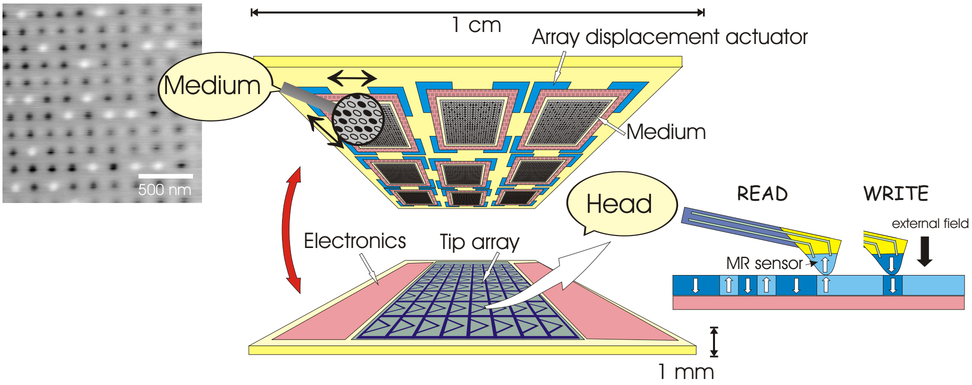

Figure 1.7: *Schematic drawing of a magnetic probe recording system, the μSPAM.*

details. However, the resolution of MFM increases much slower than the bit length in hard disk systems. The initial resolution gap is melting away very fast, as can be seen in figure 1.8 where the bit length of hard disks and resolution of MFM is plotted against time. Already in 1991 a resolution as low as 40 nm was obtained [38], and it took ten years to bring this down to 25 nm (see figure 1.8). In the meantime the bitlength in experimental hard disks has decreased from 700 nm in 1990 to 33 nm in 2001. With the instrumentation and tips we have today, it is very difficult to measure these small bits, and very soon the use of MFM in magnetic recording research could become limited.

The resolution of the MFM is amongst other factors, greatly affected by the geometry and the size of the magnetic tip [39, 40, 41]. Great effort has been put in developing tips that are suitable for high resolution MFM, as we will see further on. However, the best resolution could be obtained with hand–made tips, but also these tips leave something to be desired in terms of shape, size and reproducibility. The aim of the research, presented in this thesis, was to develop a new probe for magnetic force microscopy that could be manufactured in large quantities while being capable of sub 30 nm resolution. In terms of linear bit density in hard disk recording, the new probe should be able to image bit patterns on tracks with a density of at least 900 kFCI (28 nm bit length).

Chapter 2 gives an introduction into MFM tips. It provides an analysis of the influence of the MFM tip on the resolution that can be obtained, and introduces the design of the new probe. Chapter 3 describes the fabrication process of the new probe and the results that are obtained, along with measurements of the mechanical properties. The magnetic tip of the probe is the subject of chapter 4, where an analysis of the magnetic properties and the performance in MFM measurements is presented. To explore the capability of the new probe for

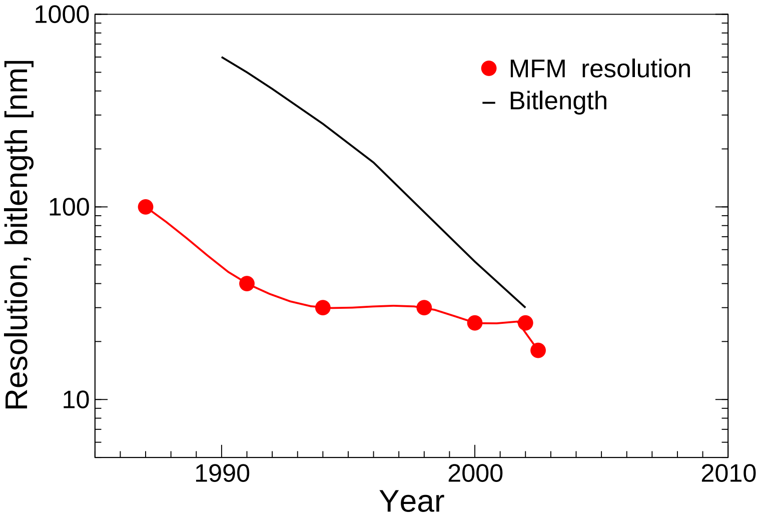

Figure 1.8: *The progress of magnetic recording and the progress in MFM resolution. The bitlength is taken from hard disc laboratory resolution is taken from literature [7, 33, 34, 12, 35, 36, 37].*

integration of other sensors besides an MFM tip, an investigation was done in chapter 5 on the integration of a magneto resistive sensor on the tip plane. The conclusions and recommendations for further research can be found in chapter 6.

Chapter 2

Tips for magnetic force microscopy

This chapter describes one of the key components of an MFM: the probe with the magnetic tip. The influence of the tip on the resolution that can be achieved with the MFM will be discussed, where special attention will be paid to the influence of the very end of the magnetic tip. Furthermore, an overview will be given of the development of the magnetic tip towards the ultimate MFM tip since the invention of the MFM in 1987 [7, 8]. Despite the efforts in micromachined tips, most of the tips suited for very high resolution MFM are still made by hand. Here, a novel design of a cantilever and tip for MFM, called the CantiClever, will be presented. This novel design enables the fabrication of a nearly ideal shaped tip for MFM in a batch fabrication process, while at the same time enables the integration of other sensors at the end of a cantilever.

2.1 MFM image formation and resolution

To determine the resolution that can be achieved in MFM and the influence of the magnetic tip, one has to study the image formation process. The formation of MFM images can be divided in three categories [42]: first, the hard magnetic case, where the magnetization of both the tip and the sample remain unchanged during scanning; second, the hysteresis free, soft magnetic case, where the magnetization of the tip or the sample is uniquely defined by the position of the tip above the sample; and third the intermediate case where the magnetization of the tip and the sample change in a discontinuous, hysteretic manner. For MFM the first case would be ideal. This can be achieved by using a hard magnetic tip with a small enough volume such that the stray field from the tip doesn't influence the magnetization of the sample. The discussion in this section will be limited to the hard magnetic case.

Several approaches have been used to model the contrast formation in MFM. For simple tip and sample magnetization structures, the response is calculated analytically in real space [43, 44, 45, 46, 47, 39, 48]. The contrast formation process for more complex magnetization structures of both tip and sample has been modelled by micromagnetic simulations [49, 50, 51, 52].

2.1.1 MFM transfer functions

Another approach to modelling of the contrast formation process is based on Fourier transformation methods and the use of transfer functions [42]. The magnetization pattern **M**(x, y, z) of a thin film is Fourier transformed in the xy–plane of the film only. The resulting complex vector $\widehat{\boldsymbol{M}}(k_x, k_y, z)$ can be used to calculate the Fourier transform of the stray field at a height z above the sample having a thickness t [53]:

$$\begin{pmatrix} \widehat{H}_x(k_x, k_y, z) \\ \widehat{H}_y(k_x, k_y, z) \\ \widehat{H}_z(k_x, k_y, z) \end{pmatrix} = \begin{pmatrix} -ik_x/|\boldsymbol{k}| \\ -ik_y/|\boldsymbol{k}| \\ 1 \end{pmatrix} (1 - e^{-|\boldsymbol{k}|t})\, e^{-|\boldsymbol{k}|z} \widehat{E}_\sigma(\boldsymbol{k}) \tag{2.1}$$

where $\boldsymbol{k} = (k_x, k_y)$ the wave vector $[m^{-1}]$ and $\widehat{E}_\sigma$ is the effective surface charge distribution $[A/m]$. The effective surface charge distribution can be seen as a sheet of charges at the sample surface, that causes the same stray field as the more complex charge distribution within the sample itself. For thin films with perpendicular anisotropy, $\widehat{E}_\sigma$ can be written as: $\widehat{E}_\sigma = \frac{1}{2}\widehat{M}_z$. The relation between $\widehat{H}_z$ and $\widehat{E}_\sigma$ is known as the field transfer function (HTF) [54]:

$$\widehat{H}_z = \mathrm{HTF} \cdot \widehat{E}_\sigma. \tag{2.2}$$

The force acting on the magnetic tip is expressed by the force transfer function (FTF), that relates the force on the tip F_z to the sample stray field:

$$\widehat{F}_z = \mathrm{FTF} \cdot \widehat{H}_z. \tag{2.3}$$

The FTF depends on the shape and the magnetization configuration of the tip. The total transfer function from the effective surface charge distribution $\widehat{E}_\sigma$ to the force acting on the magnetic tip $\widehat{F}_z(\boldsymbol{k}, z)$ is given by the tip transfer function (TTF):

$$\widehat{F}_{z,magn}(\boldsymbol{k}, z) = \mathrm{HTF} \cdot \mathrm{FTF} \cdot \widehat{E}_\sigma(\boldsymbol{k}) = \mathrm{TTF} \cdot \widehat{E}_\sigma(\boldsymbol{k}) \tag{2.4}$$

When the magnetic tip has the shape of an elongated bar, as depicted in figure 2.1, with magnetization M_t, thickness b, width S and length Δl, the total transfer

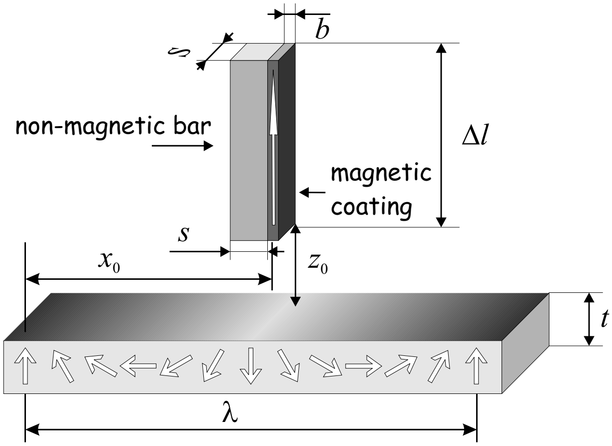

Figure 2.1: *The bar shaped MFM tip with the magnetization fixed along its axis as used to derive the TTF of equation 2.5.*

function becomes:

$$\widehat{F}_{z,magn}(\boldsymbol{k},z) = -\mu_0 M_t \cdot b\,\mathrm{sinc}(\frac{1}{2}k_x b) \cdot S\,\mathrm{sinc}(\frac{1}{2}k_y S) \\ \times(1-e^{-|\boldsymbol{k}|\cdot t})(1-e^{-|\boldsymbol{k}|\cdot\Delta l})\,e^{-|\boldsymbol{k}|\cdot z}\widehat{E}_\sigma(\boldsymbol{k}) \quad (2.5)$$

From equation 2.5 it can be seen that the force acting on the tip is proportional to the tip magnetization and the effective surface charge distribution $\widehat{E}_\sigma$ of the sample, combined with a number of geometrical loss factors. For most situations in magnetic data storage research, the films under investigation are thin and the film thickness loss term $(1-e^{-|\boldsymbol{k}|\cdot t})$ will dominate over the tip height term $(1-e^{-|\boldsymbol{k}|\cdot\Delta l})$.

Furthermore, when the tip cross–section $(b \times S)$ can be considered smaller that the smallest features in the charge distribution, equation 2.5 can be simplified to:

$$\widehat{F}_{z,magn}(\boldsymbol{k},z) = -\mu_0 M_t\, b\, S\,(1-e^{-|\boldsymbol{k}|\cdot t})\,e^{-|\boldsymbol{k}|\cdot z}\widehat{E}_\sigma(\boldsymbol{k}) \quad (2.6)$$

This approximation is called the monopole approximation, because it assumes that all magnetic charges $(M_t\, b\, S)$ are located at one point at the end of the tip, while all other charges are very far away from the sample surface. The only loss terms that remain are the film thickness loss and the tip-sample distance loss, which usually is dominant. This also shows that for a good signal to noise ratio (SNR) in the image, the tip to sample distance has to be as small as possible.

When the details in the image start to approach the tip dimensions, the sinc functions have to be taken into account as well. For the bar shaped tip, the

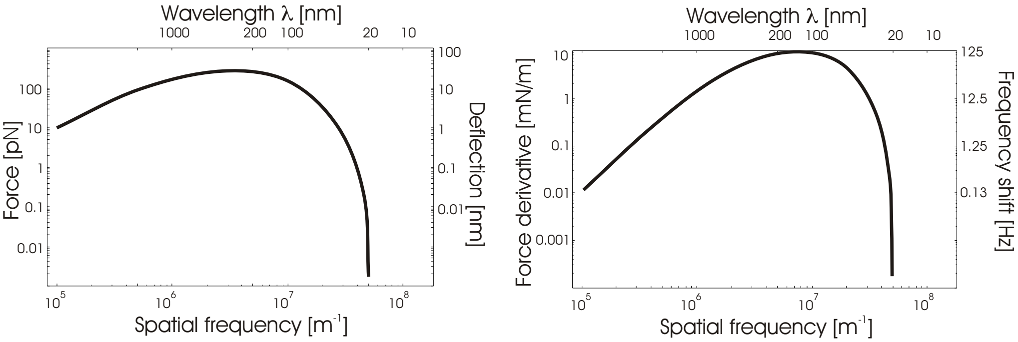

Figure 2.2: *Tip transfer functions for a typical situation calculated from equation 2.5. Left: TTF for static mode operation. Right: TTF for dynamic mode operation.*

force becomes zero when the wavelength of the surface charge distribution in the x–direction equals $k_x = n\frac{2\pi}{b}$ and in the y–direction equals $k_y = n\frac{2\pi}{S}$. This is analogue to the situation in magnetic recording, where at the gap zero the bitsize is half the gap-size of the recording head.

A typical example of TTFs for the static and dynamic mode and the resulting deflection and resonance frequency shift is given in figure 2.2. Here it is assumed that the sample has a perpendicular magnetization, only magnetic surface charges and the magnetization pattern changes only in the x–direction, so $k_y = \infty$.

The Fourier method has the advantage over the previous two because, assuming the hard magnetic case, it can be used for arbitrary samples and tips while requiring much less computing power. Besides its use for quantitative analysis of MFM data [42] it can also be used to estimate the spatial resolution that can be obtained with a certain tip–sample geometry [54] as discussed in the next section.

2.1.2 Resolution in MFM

The resolution that can be achieved by MFM depends on a combination of many factors such as the size and geometry of the tip, the tip to sample distance, the minimal measurable force and the properties of the sample.

In literature, different approaches for calculating the resolution of an MFM can be found [44, 55, 40]. The down sides of these methods are that they either are not normalized for their signal, making them difficult to apply for a comparison of different tips or they do not take the properties of the sample into account. Another method is to use the MFM transfer functions, described earlier [56].

When an imaging system has high resolution, it usually means that the system is capable of separating two closely spaced objects. It does not mean that the system can detect one single small object: this has to do with sensitivity. Resolution can therefore be defined as the minimum spacing between two objects that can still be observed. By using an array of objects, spaced equally close to each other, the definition of resolution can quite naturally be transferred to the spatial frequency domain as the minimum spatial wavelength that can still be observed. This minimum spatial wavelength is called the critical wavelength λ_c, and is defined as the point where the tip transfer function drops below the noise level [54].

Noise in an MFM originates from many sources: thermal agitation of the cantilever, electronic cross-talk, mechanical vibrations etc. Most of these noise sources can be eliminated by proper design of the detection system and operation in vacuum. In the ideal situation, the only source of noise left is the thermal vibration of the cantilever. This provides a kind of fundamental limit to MFM resolution. For dynamic mode MFM, the signal due to the thermal vibration of the cantilever is given by [57]:

$$\left(\frac{\partial F_z}{\partial z}\right)_{th,rms} = \sqrt{\frac{4kTc\,\Delta B}{\omega_n Q < z_{osc}^2 >}} \tag{2.7}$$

where k is the Bolzmann constant, T the temperature, c the spring constant of the cantilever, ΔB the measurement bandwidth, ω_n the resonance frequency of the cantilever, Q the sharpness of the cantilever resonance (quality factor) and $< z_{osc}^2 >$ the mean square amplitude of the self oscillating cantilever.

Using the tip transfer function and the expression for the thermal noise level, the resolution can be determined from figures like figure 2.3 by calculating λ_c from the intersection point of the tip transfer function and the noise level.

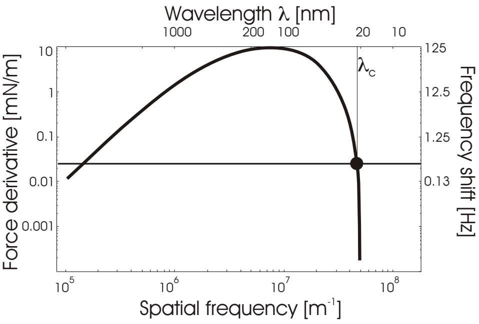

Figure 2.3: *Using the background noise level, the limit of resolution can be defined by means of a critical wavelength* λ_c.

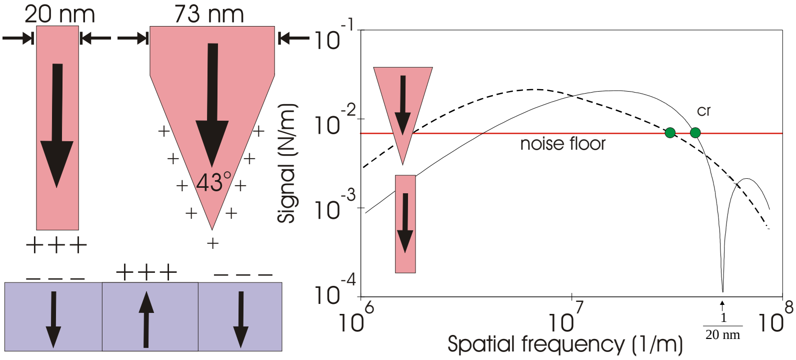

Figure 2.4: *Sharply pointed versus bar type MFM tips, graph taken from [54]. The width of the base of the triangular tip is adjusted in such a way that the maximum signals of both tips are equal.*

2.2 The ideal tip shape

Most scanning probe microscope tips are pointed and very sharp: STM and AFM tips are atomically sharp, most SNOM tips are tapered optical fibres. One might therefore assume that an MFM tip should also have the shape of a sharp needle. Techniques such as STM, AFM and SNOM however measure very short-range effects, whereas MFM measures long range magnetostatic forces. In STM and AFM only the last atom determines the signal, but in MFM a much larger part of the tip takes part in the image formation [39]. Therefore the optimum tip shape is not a sharp needle but a bar or cylinder with a flat front end [54], analogue to a single pole hard disk head for perpendicular magnetic recording.

By considering the magnetic charge distribution in a tip with an ideal uniform magnetization as depicted in figure 2.4, it can be seen why the bar shape is the optimum shape for an MFM tip. In a bar shaped tip all magnetic charges are located at the front surface of the bar, as close as possible to the sample surface. Therefore all magnetic charges contribute equally well to the signal. In a pointed MFM tip, the charge is distributed over the complete tip. The charges located further away from the sample still contribute to the signal, but their effect is stronger at longer wavelengths. If we set the maximum signal of a pointed tip and a bar type tip equal, the bar type tip will perform better at high spatial frequencies, and therefore show a better resolution. However, when the wavelengths approach the gap zero of the bar tip, the pointed tip performs better. But the bar type tip can be tailored in such a way that this happens at wavelengths above the critical wavelength. If we try to increase the signal of the pointed tip by increasing the length of the tip, only the signal at lower spatial frequencies

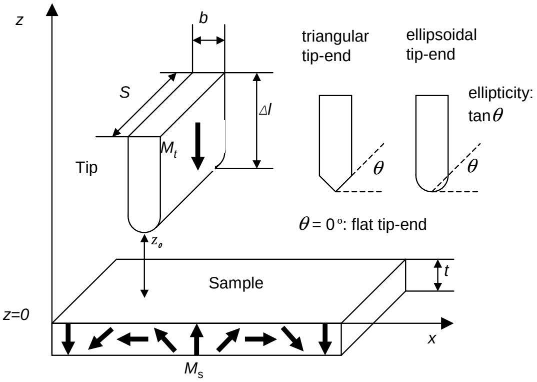

Figure 2.5: Calculation model that was used in the simulations. Taken from [58].

increases while the signal for high spatial frequencies does not increase significantly. In all cases the signal close to the critical wavelength will be highest for the bar type tip.

2.3 Simulations of the tip end shape

The shape of the magnetic tip that gives the highest signal at high spatial frequencies is that of a needle with a flat end as pointed out in the previous section. In this section we investigate how deviations of the tip–end from this optimal shape influence the sensitivity in MFM measurements and the resolution that can ultimately be obtained [58].

Three different tip–end shapes will be considered here: a needle–shaped tip with a flat tip–end (the flat tip), with a triangular shaped tip–end that resembles somewhat the shape of conventional sharp pointed MFM tips (the triangular tip) and with an ellipsoidal shaped tip–end (the ellipsoidal tip).

2.3.1 Calculation model

The model that was used in the calculations is depicted in figure 2.5. The tip used in the calculations has a magnetization M_t oriented perpendicular to the sample surface. The tip has a thickness b (thickness of the magnetic layer), width S (thickness of the tip plane) and length Δl. The sample used has a perpendicular magnetization $M_z = M_s \cos(k_x x)$ and a thickness t. No changes of the magnetization of the tip or the sample are taken into account. For each tip–end

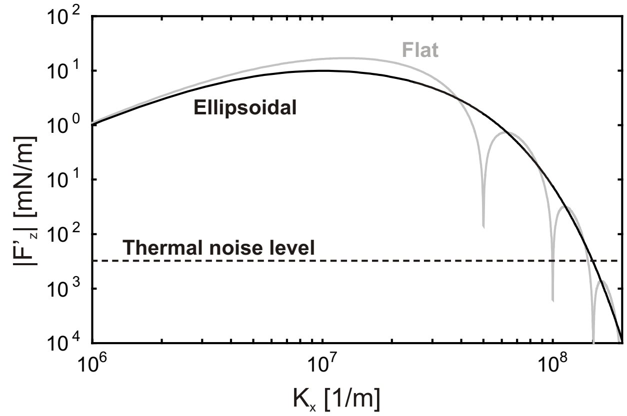

Figure 2.6: *Transfer functions of magnetic tips with a flat and an ellipsoidal tip–end shape. Taken from [58].*

shape, the tip transfer function was calculated from the following equation of the dynamic mode MFM signal for a sample with a periodic magnetic surface charge density, that is infinitely extended in y–direction [42]:

$$\frac{\partial F_z}{\partial z} = -\frac{\partial^2}{\partial z^2} U = -\frac{\partial^2}{\partial z^2} \mu_0 \int_{tip} M_t \, H_{sample} \, dV_{tip} = \tag{2.8}$$

$$-\frac{\partial^2}{\partial z^2} \mu_0 M_t S \frac{M_s}{2} \int_{tip} \cos(k_x x)(1 - e^{-k_x t}) \, e^{-k_x z} \, dx dz$$

In the calculations the following values were used: $M_t = 1422$ kA/m (the saturation magnetization of cobalt), $b = 20$ nm, $S = 100$ nm, $\Delta l = 1$ μm, $M_s = 295$ kA/m, $t = 70$ nm and the tip–sample distance z_0 was set at 10 nm.

2.3.2 Tip transfer functions

The tip transfer functions of the three different tip shapes, resulting from the simulation model described above are shown in figure 2.6.

As expected, the MFM tip that has a flat tip–end ($\theta = 0°$), has the highest sensitivity of the three shapes. Only when an integer multiple of the wavelength of the periodic magnetic stray field fits within the tip thickness b, the magnetic signal drops to zero. Moreover, the sign of $\frac{\partial F}{\partial z}$ changes alternately when the spatial frequency crosses a zero–signal frequency point. In figure 2.6, the signal is shifted by 180° in the frequency region between first and second zero–signal frequency. When the tip is used in the frequency region below the first zero–signal frequency, reducing the thickness of the tip will improve the resolution.

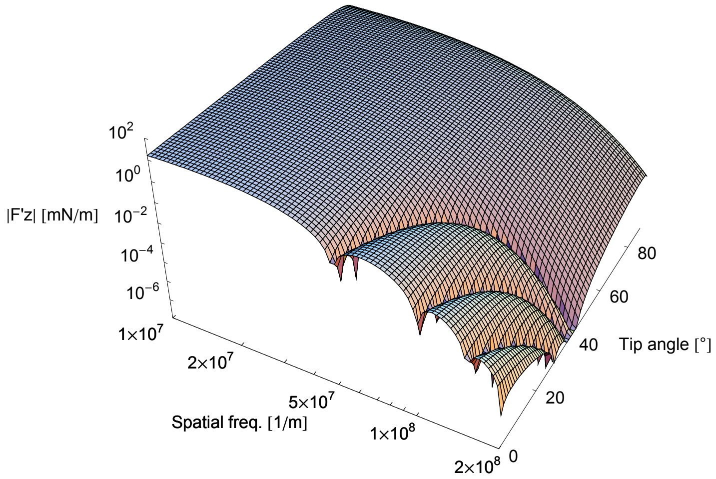

Figure 2.7: *Dependence of the tip transfer function of ellipsoidal tips on the ellipticity. Taken from [58].*

The zero–signal frequencies can be eliminated in case of an ellipsoidal shaped tip–end. When the angle is increased above 45°, the zero–signal frequencies disappear from the tip transfer function, as shown in figure 2.7. The sensitivity of the tip is at maximum when the angle θ is chosen at 80°.

2.3.3 Resolution limit

Now that the transfer functions of the tips are calculated, the ultimate resolution that could be achieved with the tips in MFM measurements can be estimated by considering the noise due to thermal vibrations of the cantilever and determining the critical wavelength λ_c as described in section 2.1.2. From figure 2.6 can be seen that at the thermal noise level, the ellipsoidal tip ($\theta = 80°$) has the smallest λ_c of the three tips when all tips have a thickness of 20 nm.

The dependence of λ_c on the thickness of the tip is depicted in figure 2.8 for the flat and the ellipsoidal tip. The ellipsoidal tip shows a much smaller dependence of λ_c on the thickness of the tip than the flat tip. The value of λ_c for the ellipsoidal tip is smaller when the thickness of the tip is above 5 nm. The reason for this is that only the center part of the tip-end mainly contributes to the signal in case of the ellipsoidal tip. Only at very high resolution, at a critical wavelength of about 7 nm, the flat tip–end is more sensitive. It should be noted, however, that the above results are valid at the thermal noise limit. In reality additional noise sources, such as electronic noise, thermal drift etc., will increase the noise level. This will shift the cross–over point in figure 2.8

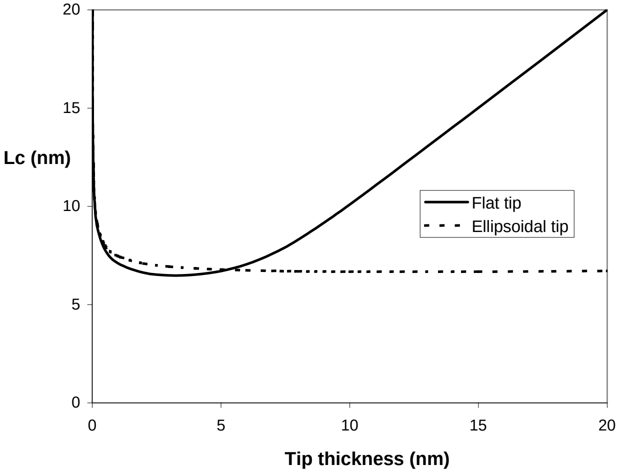

Figure 2.8: *Dependence of the critical wavelength on the diameter of the tip for ellipsoidal and flat tips. Taken from [58].*

towards thicker tips and higher critical wavelengths. Moreover, this analysis assumes that the magnetic spins in the tip are perfectly aligned. Micromagnetic simulations show however that at the very tip end, the magnetization rotates away from the tip surface. This effect decreases however with thinner tips [56].

2.4 Development of MFM tips

Knowing the optimum tip shape for MFM measurements is one thing, making such a tip is another. When realizing MFM tips, such small feature sizes are required that cannot be fabricated with conventional lithography as used in semiconductor industry. Instead we have to use tricks to obtain such small dimensions and we enter the area of nanotechnology. The first scanning probe microscope tips were hand–made, one at a time. The arrival of batch fabricated silicon and silicon nitride tips, reduced the costs of the tips while strongly improving the ease of use of the MFM. However, up till now, the best tips available are still made by hand. In the following an overview is given of the development of the MFM tips and the techniques used to fabricate them.

2.4.1 Magnetic wire tips

The first probes that were used in the MFM were iron wires [7, 59]. The iron wires were electrochemically etched to obtain a sharp point. The etched end of the wire was then bend using a pair of sharp knife edges. Although the iron cantilevers offered a high magnetic moment and thus provided a large signal, they suffered from corrosion. To overcome this problem, the probes were made from nickel [8, 60, 61], at the cost of a lower magnetic moment. The downside of all the etched ferromagnetic wire probes is that they are not very sharp and contained a lot of magnetic material. Resolutions down to 100 nm could be achieved with these tips [59].

2.4.2 Coated metal wire tips

An improvement over the etched ferromagnetic wire probes is to fabricate a sharp nonmagnetic tip and apply a thin magnetic coating [39, 62]. These probes consisted of an etched tungsten wire, fabricated in a similar way as the magnetic wire tips. On the side of these tips, the magnetic layer was deposited with thin film deposition techniques. In this way, the volume of the magnetic material could be reduced while keeping the same signal strength as the nickel wire tips. The resulting magnetic thin film was however not always smooth, due to the surface roughness on the tungsten point caused by the etching process. The resolution that could be obtained with these tips was around 50 to 100 nm.

2.4.3 Micromachined silicon tips

Most commercial available MFM probes are derived from batch fabricated silicon cantilevers with an integrated, very sharp, silicon tip [63, 64]. These probes were originally designed for AFM. To be able to measure magnetic forces, these tips are coated with a magnetic material. There is a large variety in magnetic coatings, making it impossible to list them all. The most common coating is a cobalt alloy with additions of chromium and platinum, derived from the coatings of the first tips made by Grütter *et al.* [65, 33]. These alloys are often derived from hard disk recording layer materials and have a high coercivity [66], making the tip resistant against reversal by the stray field of the sample. To achieve a high coercivity, the material is prepared in such a way that one gets magnetically separated grains. The exact location of these grains on the tip apex varies from tip to tip, which explains why some tips have higher resolution than others. Instead of alloys, also Co/Pt multilayers are used as a magnetic coating [67]. Compared to alloys, these tips provided more signal which varied only little with the tip to sample distance.

For some applications, the coercivity of the layers on the tips is not high enough, for instance when measuring stray fields from recording heads or permanent magnets. In that case very soft magnetic coatings can be used that switch in very small external fields. As a result however, the tip is always attracted and the information on the polarity of the field is lost. Materials used are for instance Co [33], NiFe [33], Fe [68] and granular Fe(SiO_2) films [69]. The perfectly soft MFM is a diamagnetic tip, that can be achieved for instance with a Pt coating. Of course the magnetic moment is much lower than in ferro- or superparamagnetic tips, and as a result, the signal is very low [70]. Although magnetically coated AFM tips are widely used for MFM, they are a bad approximation to the ideal tip shape, as pointed out in section 2.2.

2.4.4 Electron beam fabricated tips

A refinement of the tungsten tips coated with magnetic material is the use of contamination needles grown in an SEM which was accidently or deliberately contaminated with organic gasses. These so–called electron beam deposited (EBD) or electron beam induced deposition (EBID) tips, composed of carbon, oxygen and hydrogen, were first used for STM [71]. On the side of these carbon needles, a thin magnetic layer is deposited [72, 73, 34, 74]. After deposition of the magnetic layer, a carbon mask can be applied at the end of the needle to sputter etch away any unwanted magnetic material on the probe, thereby reducing the magnetic volume [41, 75]. Especially the tips made by Skidmore *et al.* are impressive, with a radius of the magnetic tip of less than 7 nm. Strangely enough, only a modest increase in the resolution of the images is obtained compared to conventional tips, the maximum resolution being 37 nm [76].

Instead of depositing a layer on the side of the EB(I)D tip, the contamination can also be used as an etch protection mask. In this way only a tiny disk of magnetic material is left at the top of an AFM tip. This MFM tip does not have the ideal shape for high resolution, but can be used for imaging of soft magnetic samples due to its very small magnetic volume [77, 78].

Another approach is to use the electron beam to deposit the magnetic needle directly using cobalt carbonyl ($Co_2(CO)_8$) as a precursor gas. On top of standard silicon AFM tips, a magnetic needle measuring 72 nm at the tip apex in diameter and 160 at the base and 1.7 μm long could be deposited. With these tips, 44.7 nm bit transitions could be resolved [79].

2.4.5 FIB modified tips

With the use of a focussed ion beam (FIB) system, it became possible to achieve a very small tip end radius by etching the end of the tip. Using this technique, tips for STM could be prepared with a radius of curvature of the tip end down to 3.5 nm [80]. This technique was also applied to standard silicon AFM tips. On the side of these sharpened tips, a magnetic layer was deposited. These tips provide a clear improvement in resolution over commercially available MFM tips [81].

Another approach is to use the FIB to partly etch the magnetic layer on commercial MFM tips (i.e. silicon AFM tips, coated with magnetic material). Folks *et al.* [35] use the FIB to etch a small hole at the apex of the tip. The tip is then magnetized in–plane (parallel to the cantilever), so that magnetic charges occur at the edges of the tip. In this way an in-plane tip can be obtained which is only sensitive to stray fields parallel to the sample in the direction of the tip magnetization. With this tip, written tracks with a bit length down to 50 nm could be resolved. In general one would like to measure the vertical component of the sample stray field, from which the x– and y–components of the fields can be derived. Such a tip is prepared by Philips [36], who etched away the unnecessary magnetic material to obtain a 8 μm long and 50 nm wide needle. Point–dipole tips have also been prepared with the help of FIB [82, 83]. In this case, most of the magnetic material on the tip is etched away, except for a small particle at the end of the tip. By controlling the easy axis of the magnetic material it is possible to define the preferred directional sensitivity (vertical or in–plane).

2.4.6 Carbon nanotube tips

A tip with a very small cross section and a high aspect ratio can also be made from a carbon nanotube [84]. These were again first used, mounted at the end of a standard silicon AFM tip, in AFM and STM measurements [85]. To be able to measure magnetic forces, Arie *et al.* [86] and Yoshida *et al.* [87] attached small ferromagnetic particles at the end of the carbon nanotube. The ultimate resolution that can be achieved with this type of tip still has to be determined. More recently, convenient and fast methods have been discovered to attach the carbon nanotubes to the AFM tip [88, 89], even on wafer scale. These techniques would make batch fabrication of such tips possible.

2.5 The CantiClever concept

As mentioned earlier, a magnetic tip that is suitable for high resolution MFM should be shaped like a bar magnet with lateral dimensions (tip cross section) in the nanometer regime, as depicted in figure 2.9. One would like these dimensions to be reproducible, controllable and variable to be able to customize the MFM tip for different types of measurements or samples. None of the methods to fabricate high resolution MFM tips, described in the previous section, is able to fabricate such a tip with precise control over the tip dimensions in large numbers.

2.5.1 The magnetic tip

The CantiClever concept presented in this thesis can accomplish this by defining both lateral dimensions of the magnetic tip by thin film deposition techniques. The magnetic tip is made by deposition of magnetic material on the side of a free hanging, non magnetic, very thin layer called the tip plane. The width and thickness of the magnetic tip are defined by the thickness of the tip plane and the magnetic layer respectively. The length of the tip is defined using photolithography to make a very high aspect ratio of the magnetic tip possible. A schematic drawing of the structure is shown in figure 2.9.

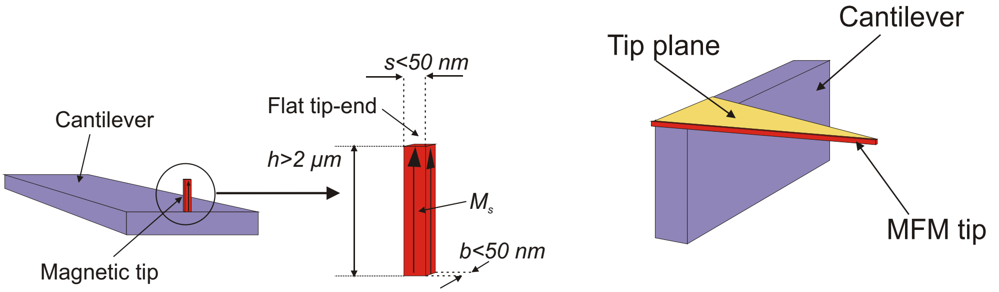

Figure 2.9: *Left: Ideal tip shape for an MFM tip. Right: the realization of the ideal tip shape with the CantiClever design.*

Two factors play an important role in realizing a high resolution MFM tip that resembles the ideal tip shape as closely as possible. First, the freestanding tip plane should be very thin, as this defines the width of the tip, but strong enough for contact imaging and at the same time should have low stress to prevent bending. Second, the tip plane should have a well defined and very sharp cut–off corner as illustrated in figure 2.10. This ensures that the front surface of the tip is minimized and approximately flat, resulting in the highest possible resolution. How this sharp cut-off corner is realized, is described in section 3.3.2.

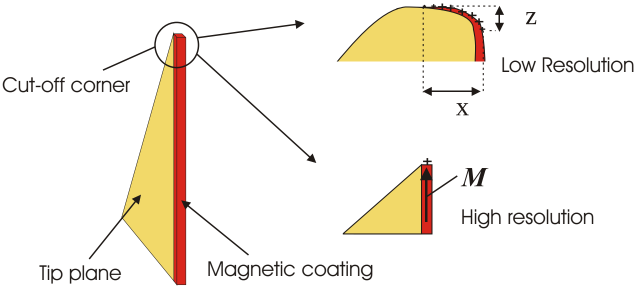

Figure 2.10: *Influence of the cut–off corner of the tip plane on the imaging resolution.*

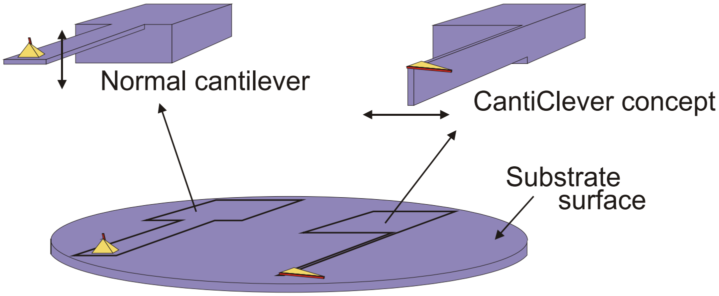

Figure 2.11: *Fabrication of the tip and the cantilever. Left: conventional approach with the cantilever vibration direction horizontally. Right: the new approach of the CantiClever concept.*

2.5.2 The cantilever

Realizing a freestanding tip plane on the side of a cantilever is very difficult when it has to be made in a fabrication process that is similar to that of conventional silicon cantilevers. During fabrication, the conventional cantilevers are situated such that the oscillation direction is perpendicular to the surface of the substrate, with the tips of the probes pointing out of the substrate surface. When we would use the same approach, we would have to fabricate the very thin tip plane as a freestanding layer perpendicular to the substrate surface. To avoid this, we propose a completely new approach to fabricate the cantilever. During fabrication, the cantilevers are tilted 90 degrees compared to the conventional cantilevers, such that the oscillation direction is now parallel to the substrate surface as shown in figure 2.11. This approach makes the fabrication of the cantilever more difficult compared to conventional cantilevers, but also enables precise control over the cantilever resonance frequency. This will be explained in more detail in section 3.1.2.

2.5.3 Integration of other sensors on the probe

Furthermore, standard deposition and etching techniques can be used to define the tip plane, as it is also oriented parallel to the substrate surface. The result is a reproducible planar manufacturing process that incorporates both the cantilever and the magnetic tip and allows for batch fabrication of the probes. The definition of the tip with planar fabrication process has another advantage. It provides the opportunity to integrate other sensing elements and the electrical connections that might be needed on the tip and cantilever with relative ease.

Many different applications using scanning probe microscopy can be found in literature that require cantilevers equipped with sensing elements. A probe with a single electrical contact to the end of the tip could for instance be used in scanning capacitance microscopy and –recording [90]. The integration of a thermocouple sensor on the tip enables high resolution thermal microscopy [91, 92, 93], that gained more interest recently because of its application for failure analysis of high speed integrated circuits. For this purpose, also probes with integrated Schottky diodes have been developed [94]. Other possibilities for integration are heaters [95], a pH sensor for use in a scanning probe potentiometer [96, 97], a waveguide and transparent aperture tip for combined atomic force/near–field optical microscopy [98] and a Hall sensor for qualitative measurement of magnetic stray fields [99, 100, 101, 102]. In this work, the possibilities of the CantiClever concept for the integration of sensors besides an MFM tip are investigated by the integration of a magnetoresistive sensor on the tip plane, that will be presented in chapter 5.

Chapter 3

Fabricating the CantiClever

The topic of this chapter is the realization of a probe based on the CantiClever concept shown in the previous chapter. The first section describes the design of the probe. In the following sections the development of the fabrication process to make the probes and the results that were obtained are presented. Finally a characterization of the mechanical properties of the probe is given.

3.1 The design of the probe

3.1.1 Parameter based mask design

The most common method to design structures of micromechanical devices is by drawing them in a mask design program. Small parts of a larger structure can be combined into a group and the group can be used to make up a complete device and eventually groups of devices can make up a complete mask. Although this is an intuitive and visual process, it has several disadvantages.

- Implementing several variations of a particular design mostly requires editing each single structure by hand. If adaptations influence the placement of other structures as well, these also have to be placed on a different position by hand. This re–drawing of structures often requires a lot of work. In case of the CantiClever, this would mean drawing each cantilever individually when probes with different resonance frequencies are required, because resonance frequency depends on the length of the cantilever.

- When flaws in the design force the mask to be adapted at a later stage the same situation occurs. Even small modifications on a single type of structure can result in many structures that need to be modified by hand.

- Designing a structure with certain properties involves almost always a number of calculations. When several similar structures are needed with differences in one of the properties, calculations have to be done for each structure individually. This generates a lot of calculations that need to be done by hand. The structures then have to be drawn by hand, leaving a lot of room for errors.

To design the CantiClever probe presented in section 2.5, a parameter based design method was used that doesn't suffer from the disadvantages mentioned above. The structures are not drawn, but programmed using a limited number of standard shapes. Each shape has its own set of parameters that determine what the shape is going to look like, i.e. its length or width. With the help of user definable variables the parameters can be given a certain value. This value can be calculated using a large number of mathematical functions. The resulting shapes are then combined into groups. A single device and eventually a complete mask can then be made out of a number of groups in the same way a program, written in a programming language, is made out of subroutines. Structures can also be combined into libraries that enable the programmed shapes to be easily re–used in other designs. The result of this is a hierarchical design that is highly flexible, easy to modify and has a great accuracy.

In this work, a program specially suited for designing micromechanical and integrated optical devices was used, called Odin [103]. Odin works following the principle described above. It was originally developed for designing and simulating waveguide structures used in integrated optics. The waveguide structures in Odin are constructed by connecting individual shapes together in a chain with the help of planes. A plane is defined by x– and y–coordinates and an angle. Every shape has at least one plane as its input and one as its output. The output plane of the first shape is connected to the input plane of the second shape and so on, as depicted in figure 3.1. This system proves very handy also in designing other devices besides integrated optics waveguides because it makes the positioning of the individual structures independent of the absolute coordinates.

In the program are also a large number of functions available known from programming languages that manipulate groups and variables, like a for–loop and an if–statement. This makes the automated generation of a large number of structures with varying dimensions possible.

3.1.2 The cantilever and the tip

Because the tip plane is oriented parallel to the substrate surface as described in section 2.5, the cantilever is rotated 90° with respect to a conventional cantilever design. The mask of the cantilever defines thus its length and thickness instead

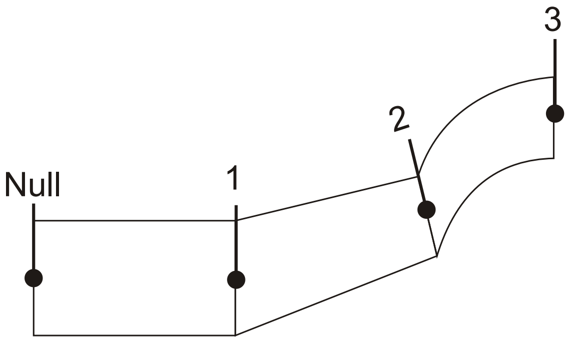

Figure 3.1: *Design of structures in Odin. The position of the center of a plane is indicated by the dot and the angle by the line. The Null–plane indicates the starting point. From left to right a straight, taper and bend are drawn.*

of its length and width as common in conventional probes. The resonance frequency of the cantilever is given by [104]:

$$f_0 = \frac{1}{2\pi} C_0^2 \frac{t}{l^2} \sqrt{\frac{E_{Si}}{12\rho_{Si}}} \tag{3.1}$$

where C_0 is the eigenvalue of the system corresponding to its fundamental frequency, having a value of 1.875, t the thickness of the cantilever, l its length, E_{Si} the Young's modulus of silicon in the $\langle 111 \rangle$ direction (186 GPa) and ρ_{Si} the density of silicon (2330 $\mathrm{kg/m^3}$).

In contrast to conventional cantilevers where the thickness is defined with an etch stop, here the thickness is defined by the mask and can be varied. For most of the cantilevers in the design, the thickness is kept constant at 6 microns and the length is calculated to match the desired resonance frequency according to equation 3.1. Another advantage of the rotated orientation of the cantilever is that it could enable the realization of tuning fork cantilever structures. An increase of the quality factor is expected because the base of the fork does not oscillate, resulting in a reduction of energy loss into the mounting of the cantilever (which is exactly the reasons why tuning forks are used). The cantilevers present in the final design are much longer than required to obtain a certain resonance frequency. This is done to compensate for under–etching effects that occur due to the nature of the fabrication process. This will be discussed more in detail in section 3.2.

The end of the cantilever facilitates the tip plane structures. The complete

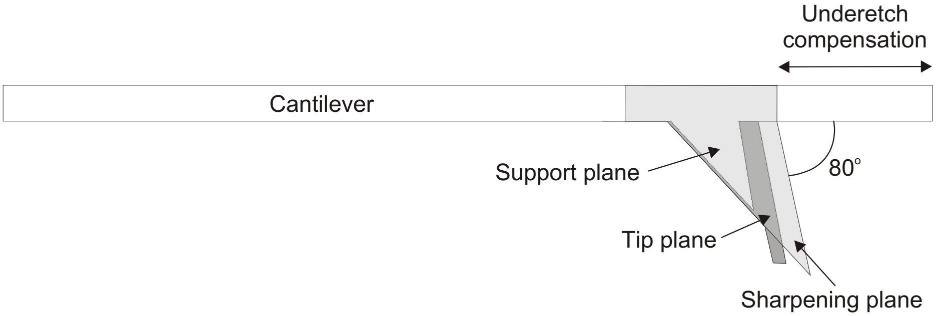

Figure 3.2: *Schematic drawing of the structures of the tip. The thicker support plane and the very thin tip plane are covered by the sharpening plane. Every part of the tip that is not covered by this plane will be removed at a later stage. The extra length of the cantilever, to compensate for under–etching effects, is also shown.*

structure consists of three parts. A relative thick layer, called the support plane, to provide strength and to prevent bending of the free hanging structures. On top of this layer the actual tip plane is defined, that extends past the support plane. The thickness of this plane determines the width of the magnetic tip, as discussed in section 4.3. The third part is the tip sharpening plane, that is used to cut off the blunt part of the tip. This is described in more detail in section 3.3. Furthermore, the planar fabrication process of the tip plane enables the tip plane to be shaped in such a way, that the front side of the tip is normal to the sample, when mounted in our commercial probe microscope. During scanning, the cantilever makes a 10° angle with respect to the sample surface [105]. Therefore, the angle between the side of the tip plane and the cantilever is at 80°. An overview of the cantilever and tip plane structures is depicted in figure 3.2.

3.1.3 The base of the probe

The base of the probe is the part where the probe is held using tweezers during handling and that is placed into the probe holder of the microscope during measuring. These two functions place two demands on the design of this base.

- The first demand is that it must be possible to measure with the probe in most existing probe microscopes. The base must be shaped in such a way that the end of the cantilever is at exactly the same position as a the one of

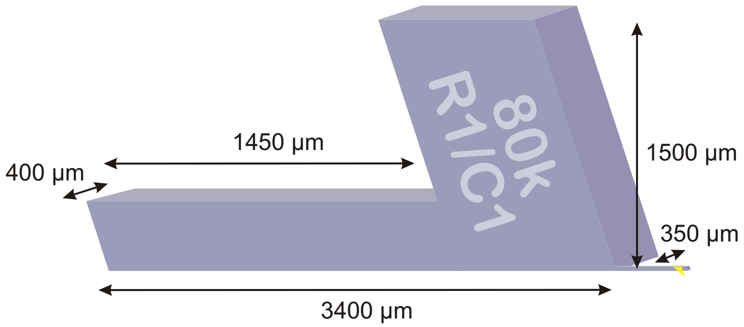

Figure 3.3: *The designed base of the CantiClever probe. Note that the cantilever and tip plane are magnified for clarity.*

a conventional probe would be, to avoid problems with focussing of the laser used in the optical detection system of most probe microscopes.

- The second demand is ease of handling. As a result of the rotated cantilever concept, the probes must always be rotated when picked out of the wafer before they can be mounted in a microscope for measuring. The holder must make this task as easy as possible, minimizing the chance of damaging the probe during handling.

The dimensions of a typical conventional probe are used as a guideline in designing the base of the CantiClever probe. The base of such a probe has a rectangular shape that is around 3400 μm long, 1600 μm wide and 315 μm thick [106]. The base of the CantiClever probe is depicted in figure 3.3. The length and thickness of the narrow part of the base is chosen such that the cantilever is at the same position as that of a conventional probe, while the width is as large as possible to ensure a stable mount in the microscope, limited by the thickness of the wafers that are used. The wide part of the base is as big as possible to facilitate an easy handling of the probe. Note that the skewed shape of the base is a result of the fabrication process, that is described in detail in sections 3.2 and 3.3. On this part of the base an identification is also present that indicates from which part of the wafer it came from and the resonance frequency of the cantilever. This is a typical example of something that can very easily and automatically be done using a parameter based design method.

3.1.4 The mask layout

The fabrication process of the complete probe requires 6 masks, of which 5 had to be designed and one was already available. The mask that defines the base,

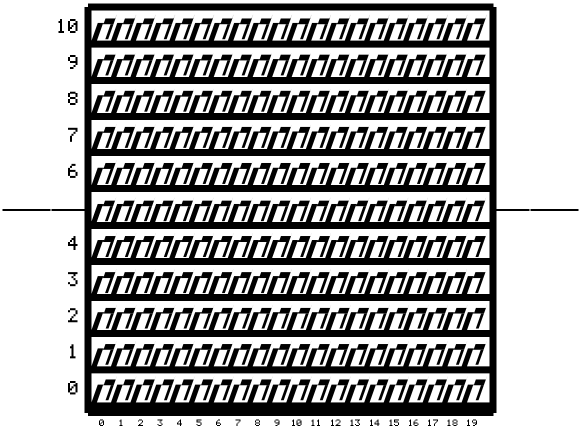

Figure 3.4: *The mask layout for a wafer of CantiClever probes.*

the cantilever and the support plane of the probe is shown in 3.4. It gives a good impression of how a finished wafer with CantiClever probes is going to look like. On the mask, a square array of probes is defined. The 100 mm sized wafers used in this work can facilitate 11 rows, each containing 20 probes. More probes could be packed onto a single wafer, but a relative large distance between the probes makes taking one of the probes out a lot easier. The probes had a number of different resonance frequencies: 60 probes with an 80 kHz resonance frequency, 20 ranging from 80 to 500 kHz, 40 with 500 kHz and 20 with 1 MHz. Two other types of probes are also present on the wafer; one row with as low as possible spring constants and a row containing preliminary tuning fork type probes. The function of the other masks and a detailed description of the fabrication process will be given in the following sections.

3.2 Fabrication of the cantilever

The CantiClever probe will be made out of single–crystal silicon substrates, as single–crystal silicon is a good choice as the cantilever material. It has low intrinsic mechanical loss that is beneficial for achieving a high quality factor of the cantilever. This will be treated in more detail in section 3.5.2. Furthermore single–crystal silicon has a very low internal stress, allowing for long, thin structures to be fabricated without unwanted curling [107, 108]. Finally, as this is one of the most common substrates used in micromachining, it has the advantage that numerous processing methods and a lot of experience with the processing is available.

The use of a tip plane that is oriented parallel to the wafer surface forces the cantilever to be defined with its oscillation direction parallel to the wafer surface as well. This poses several demands on the etching process that will be used to etch the cantilevers out of the substrate. First, a strong anisotropic etching process has to be used to etch the cantilever structures out of the silicon substrate. Otherwise the mask will be under–etched, damaging or even breaking the cantilevers. Second, the width of the cantilever will be much smaller than the thickness of the silicon wafer. This means that the wafer has to be thinned down from the backside to meet the required width of the cantilever. The etching process must be capable to etch large depths with high uniformity as well. The third demand has to do with the tip plane. As proposed in section 2.5, the tip plane is a free hanging thin film from the side of the cantilever. A silicon etching process is thus required that is capable of removing the silicon beneath the tip plane.

3.2.1 Anisotropic etching of silicon

There are two commonly used processes that can be used to anisotropically etch silicon: dry etching and wet chemical etching. Both methods can be applied in numerous variations. Described in this section are only a very few of them that were investigated as a possible candidate for etching of the cantilever structures.

Dry etching

The two main anisotropic dry etching methods used are physical ion beam etching (IBE) and synergetic reactive ion beam etching (RIE) [109]. The IBE process is not very suitable for the etching of cantilever structures. Vertical sidewalls are hard to obtain due to the positively tapered etch profile of the IBE process. Moreover, the physical nature of the etching process gives relatively low etching rates (several nanometers per minute) and a poor selectivity, leading to quick corrosion of the etch mask regardless of the mask materials used [110, 111, 112].

Much better results can be obtained by RIE methods. The plasma used in RIE provides three elements that are needed to achieve a highly anisotropic etch profile: a chemical etchant for etching of the substrate, a passivator for preventing the etching of the sidewalls of a trench and an ion source for removing the passivation layer at the bottom of the trench. An RIE process for anisotropic etching of silicon is described in [113]. Here the silicon is etched in a fluorine–based plasma consisting of SF_6, O_2 and CHF_3 gasses. The SF_6 produces the F* radicals for the etching of silicon, the O_2 gas the O* radicals, needed to form the passivation layer, and the CHF_3 the ions, needed to etch the passivation. The etching process is schematically depicted in figure 3.5. A problem with this etching technique is the formation of very high aspect ratio spikes (“grass”) on the silicon surface due to micro masks deposited or grown on the silicon. Sur-

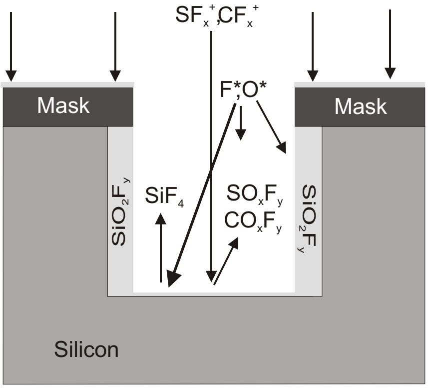

Figure 3.5: *The chemistry of the black silicon method, taken from [114].*

faces with this grass appear black to the eye. Because of this phenomenon, the etching method is also known as the Black Silicon Method (BSM). The etch profile can be controlled by changing the flow rate of one or more gasses. When the CHF_3 flow is increased, a slightly negative tapered etching profile occurs that prevents the formation of black silicon [114].

Wet chemical etching

One of the most used methods for anisotropic etching of silicon is wet chemical etching in aqueous alkaline solutions such as potassium hydroxide (KOH). When silicon is etched using these solutions, the etch rate of the exposed silicon surface depends very strongly on its crystal orientation [115]. Etch rate ratios between different crystal orientations as large as 400 times are reported in literature [116], the family of $\{111\}$ planes being the slowest etching. This highly anisotropic etching behavior is illustrated in figure 3.6. The $\{111\}$ planes will act as boundary planes with well defined angles to the substrate surface. This property can be used to fabricate vertical high deep aspect ratio trenches in silicon using $\langle 110 \rangle$ oriented substrates as shown by [116] and [117].

Two other factors that greatly influence the etch rate of silicon in KOH solutions are the temperature and concentration of the etchant. By making smart use of these dependencies, thin walls, perpendicular to the substrate surface could be made in the more common $\langle 100 \rangle$ oriented wafers when a highly concentrated KOH solution was used [118]. In that case, the $\{100\}$ planes etch slower than the surrounding planes, so that these can be used as boundary planes to define a wall perpendicular to the substrate.

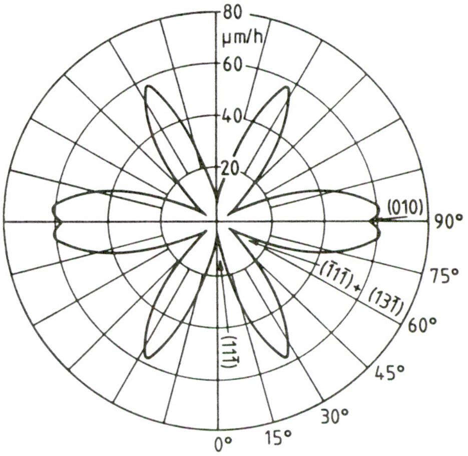

Figure 3.6: *Lateral under–etch rates as a function of orientation when etching* ⟨110⟩ *wafers. Close to the slowest etching* {111} *planes are etch rate maxima. This requires precise alignment of the masks to the orientations to prevent unwanted under–etching. Taken from [115].*

3.2.2 Choice of the etching process

From the etching methods described above, a choice was made for etching of the cantilevers. From the two dry etching methods, IBE proves not suitable for our purpose: its low etch rate, quick mask erosion and tapered etch profile prevent the vertical sidewalls and high aspect ratio trenches, needed to define a cantilever structure, to be made this way.

The black silicon method

RIE of silicon using the black silicon method is a much more promising candidate. The vertical etch profile ensures the accurate definition of the length and thickness of the cantilever. Very deep trenches up to 200 microns can also be made [119], so the definition of the cantilever width could be possible. There are also a number of disadvantages however. First, the etch rate and profile depend on the feature size. Small trenches are etched slower and their profile differs from those of wider ones [119]. Second, the materials suitable for masks in this process must not corrode, be conductive, have a high selectivity compared to silicon and not contribute to higher temperature of the trench walls if a vertical profile is to be achieved [119]. This prevents the use of photoresist, silicon oxide and silicon nitride as a mask material. Metal masks prove a good candidate with almost infinite selectivity, but require additional processing steps. Third,

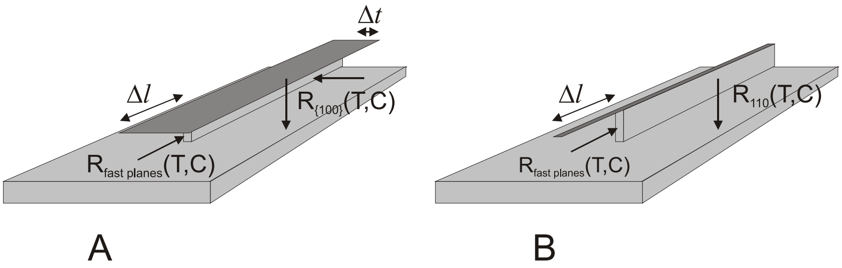

Figure 3.7: Under–etching of the cantilever mask during wet chemical etching in an aqueous KOH solution when ⟨100⟩ wafers (A) or ⟨110⟩ wafers (B) are used.

under–etching of the tip plane is not possible with this process. A separate etching step will be required to free the tip plane. This can't be an isotropic etching step, because that would etch the other parts of the cantilever as well. For this reason, this method is abandoned.

KOH etching of ⟨100⟩ wafers

Wet chemical etching using an aqueous KOH solution is capable of both etching great depths, needed to define the width of the cantilever, and defining vertical sidewalls, needed to define the thickness of the cantilever. A big advantage of an KOH etching process is that the silicon beneath the tip plane structures will be automatically etched away as long as the mask is not parallel with one of the {111} planes. When ⟨100⟩ oriented wafers are used, vertical sidewalls can be made but both the wafer surface and the vertical walls are defined by {100} planes. As these have the same etch rate, the structure will be undercut at the same speed as the vertical etching takes place. This is depicted in figure 3.7. This makes high aspect ratio structures of the cantilever very difficult to make. Moreover, the thickness of the cantilever is now dependent on its width, which is not desirable. Therefore, this method is discarded as well.

KOH etching of ⟨110⟩ wafers

The under–etching problem is solved when ⟨110⟩ oriented wafers are chosen as a substrate. The {111} planes that are oriented perpendicular to the substrate surface can be used to make vertical sidewalls. The etching of the cantilevers is done in two steps. First windows are etched from the backside of the wafer to thin the substrate down to the desired width of the cantilevers. When the etch mask is oriented parallel to the very slow etching {111} planes, large etch depths can be achieved with very little under–etching. Subsequently, a second etching step defines the thickness and length of the cantilevers from the front side of the substrate. The mask used to define the cantilever is again aligned parallel to the {111} planes oriented perpendicular to the surface, using them to define the sides of the cantilever. The tip plane structure will be under–etched automatically. To accurately etch the cantilevers in this second etching step, the backside windows have to be protected from the etchant, so that the etching only takes place at the front side. Unfortunately there are two drawbacks to this method. First, convex corners present on the mask will be under–etched because fast etching crystal planes are exposed to the etchant. This can happen at the edges of the base of the probe during the first etching step, but also during the second etching step to the cantilevers: the front side of the mask will certainly be under–etched, thereby shortening the cantilevers. This can be compensated for by making the cantilevers longer than they need to be according to the desired resonance frequency. Second, the bottom of the etched trenches is defined by one of the {110} planes. The roughness of these planes when etched in KOH is larger than that of the {100} planes. The roughness of the bottom surface can be in the order of several microns [117]. By making the width of the cantilever large compared to the width variations, the influences on the mechanical properties of the cantilevers can be kept small. Despite the drawbacks, the use of wet chemical etching using ⟨110⟩ oriented wafers as a substrate seems to be the best suitable etching method and will be used to fabricate the cantilevers and the base of the probe.

3.2.3 The fabrication process

Mask materials

To be able to define structures using an etching process, a suitable material has to be found for making a mask. All materials that etch slowly enough in the etching process that is used can be applied as mask materials. A number of metals is resistant against KOH. Among them are gold, silver, copper and chromium [112]. But the most commonly used mask materials in the case of KOH etching are silicon dioxide and silicon nitride. The etch rate of silicon dioxide is dependent on the KOH concentration and has a maximum of nearly 80 nm/hour at a 35% concentration [115]. Silicon nitride performs even better: almost no etching of the layer was observed by Seidel *et al*. They report an upper limit of less than 0.1 nm/hour [115]. This material will thus be used as a mask for the etching process of the cantilevers.

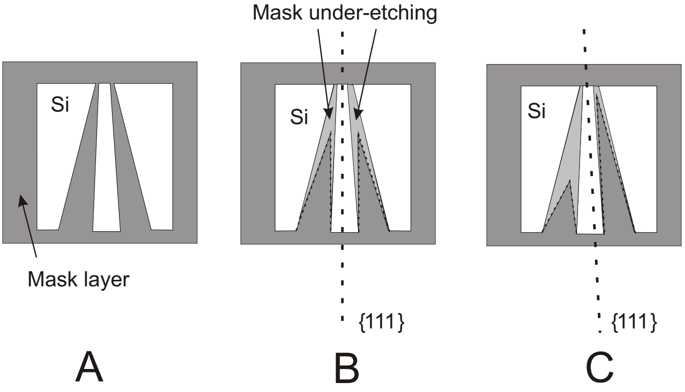

Figure 3.8: *The alignment fork pattern to determine the exact orientation of the {111} planes is shown in A. After etching, an under–etch profile occurs. A perfectly aligned structure is shown in B, misalignment results in an under–etching profile depicted in C.*

Mask alignment

Precise alignment of the mask to the crystal planes is crucial when the cantilevers are etched in KOH. A slight misalignment would cause serious under–etching of the cantilever mask. The flats that indicate the position of the {111} crystal planes on the wafers have an angle accuracy of around 1°. This is not precise enough to prevent undercutting of the mask. Therefore, a very accurate method was used to find the location of the {111} crystal planes. This method, described in [120], makes use of the symmetric under–etching behavior around the {111} planes. A large number of so called alignment forks are used that have a small angular offset between them. After a short etching step, the alignment fork oriented parallel will be symmetrically under–etched and the forks that have a misalignment with respect to the orientation of the {111} planes asymmetrically, as can be seen in figure 3.8. The correct alignment fork can then be used for aligning the subsequent masks.

The processing steps

Four of the six masks required in the fabrication process of the complete probe are needed to fabricate the cantilever and the base of the probe. A complete description of the fabrication process and pictures of the designed masks can be found in the appendix. An overview of the process is as follows:

- The first step is to find the exact location of the crystal planes, using the method described above. On the substrate a 50 nm layer of silicon nitride, deposited in a low stress LPCVD process is used as masking material. On the front side the layer is patterned using photolithography and an RIE step. The mask with the structures for this step is a copy of that designed by Vangbo *et al.* [120], and was already available. After a short KOH etch, the exact location of the {111} planes can be established.

- The alignment marks needed in the remainder of the fabrication process are defined in this step. For each subsequent mask a dedicated pair of marks is etched into the wafer. This minimizes the alignment errors. Furthermore, each set of marks is etched into the wafer with a different spacing between the left and right mark. This ensures that subsequent masks can only be aligned on top of the correct marks. This mask, called the 'alignment mark mask', is aligned using the symmetrical under–etched alignment fork found in the previous step. The marks are then covered with another layer of silicon nitride, to protect them from further etching.

- Subsequently, the width of the cantilever is defined by KOH etching of the wafer from the backside until the thickness that remains, corresponds to the desired width of the cantilever. This process takes several hours because almost the entire thickness of the substrate is etched away. For this process, windows are defined in the silicon nitride layer on the backside using the 'backside window mask'.

- In the last step the mask for etching of the cantilever patterns is defined out of the silicon nitride layer on the front side using the "cantilever and support plane mask". After the tip plane structures are defined, as described in the next section, the cantilevers can be etched free using the KOH wet chemical etching process described above. It is crucial that the back side of the wafer is protected from further etching in this step. Otherwise the cantilevers would be etched from all directions, and uncontrollable under–etching of the cantilever will occur.

3.3 Realization of the tip plane

3.3.1 The tip plane material and deposition method

The CantiClever concept, presented in section 2.5, defines the tip plane as a free standing thin film on the side of a cantilever. To realize such a structure that can be used for scanning in a scanning probe microscope the material from which the tip plane is made has to meet several requirements:

- The thickness of the tip plane must be controlled in the nanometer range. This limits the fabrication process to thin film deposition methods such as evaporation, sputtering or chemical vapor deposition (CVD) processes.

- Modes such as contact imaging or tapping mode imaging are frequently used in probe microscopy. Despite being a freestanding thin film, it still has to be strong enough to be used as the tip of a probe in a probe microscope that uses these modes.

- As the tip plane hangs unsupported for around 20 microns in free space from the side of the cantilever, while its thickness is in the nanometer range, the material has to have a low stress to avoid bending of the tip.

- The cantilever is fabricated using the KOH wet chemical etching method described earlier. The material must not be etched in the etchant that is used, or complicated protection methods have to be applied. As this is not desirable, the materials that can be used are limited to the masking materials used for KOH etching like a number of metals, silicon dioxide and silicon nitride.

From the requirements stated above it is obvious that the material has to be chosen out of the materials that can withstand the cantilever etching process. The most commonly used masking materials in KOH etching processes are silicon dioxide and silicon nitride. The latter has a clear advantage because of its negligible etch rate in an KOH etching process [115].

Moreover, its mechanical properties are also better than those of silicon dioxide. The material is stiffer than silicon dioxide, so less bending will occur when the tip plane comes in contact with the sample during scanning. This can be concluded from its higher Young's modulus of 310 GPa compared to 73 GPa of silicon dioxide. Silicon nitride is also more resistant against wear, as indicated by its higher value of the Knoop Hardness of 3.5×10^9 kg/m^2 compared to 0.8×10^9 kg/m^2, the value of silicon dioxide. This is only half of that of diamond, one of the hardest materials available [121].

Another requirement is that of low stress to prevent bending of the free hanging tip plane. The deposition method plays a vital role here. The silicon nitride layer commonly used as masking materials for wet chemical etching of silicon are usually grown in a low pressure chemical vapor deposition (LPCVD) process [122, 123]. Stochiometric silicon nitride layers have a large intrinsic stress. However, the LPCVD process can be adjusted such that the silicon content in the layer is increased. With the proper set of process parameters, a silicon nitride layer can be deposited that has a low residual stress without an unacceptable increase in nonuniformity across the substrate [124]. In the MESA$^+$ cleanroom, such a process is available and this was used to deposit the layers.

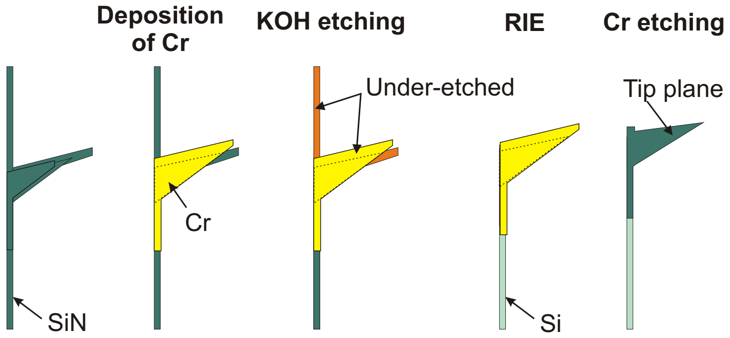

Figure 3.9: *Process for sharpening of the tip plane.*

3.3.2 Tip sharpening

To be able to achieve a high resolution when the probe is used for MFM measurements, the end of the tip plane must have a very small radius of curvature as described in section 2.5. When the tip plane is defined in a single step using photolithography techniques, the corner defined on the mask will be rounded off and will therefore not be sharp enough.

A very sharp tip end can be created however by cutting of the blunt end of the tip plane. The process is schematically drawn in figure 3.9. An extra masking layer has to be deposited on top of the tip plane. This layer has to meet several demands: it must be able to withstand KOH etching, has to have good masking properties when etching silicon nitride layers and must be removable without damaging the fragile tip plane. From the masking materials listed above, chromium is a suitable material for making the tip sharpening mask. It has a good resistance against KOH etching and the RIE process normally used to etch silicon nitride [119] and can be removed using a chemical etchant without damaging the silicon nitride layer below.

3.3.3 The processing steps

When the CantiClever is used as an MFM probe, the thickness of the tip plane determines one dimension of the cross section of the magnetic tip. One would like to vary the thickness of the tip plane without any further influences on the rest of the fabrication process. Moreover, the tip plane becomes very fragile when it extends for around 20 microns past the side of the cantilever if it has a thickness of only a few nanometers. Therefore most of the tip plane is much thicker to provide strength. This part is further referred to as ‘support plane’. The thin part of the tip plane, called ‘tip plane’ extends only a couple of microns

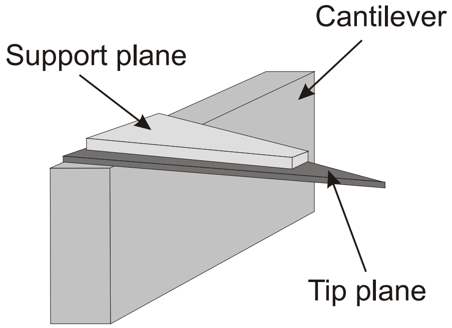

Figure 3.10: *The structures of the tip, showing the support plane and the tip plane extending past it.*

past the thick part as shown in figure 3.10. For use as an MFM probe, this is not a problem since the features usually observed in MFM are smaller than 1 micron. Therefore, a few micron distance between the support plane and the end of the tip plane is sufficient.

To realize such a tip structure, two depositions of silicon nitride are necessary. In a first deposition, the layer from which the support plane is defined is deposited. The actual tip plane is deposited in a second step. The process continues that of section 3.2.3 and looks as follows:

- The support plane is defined together with the mask for etching of the cantilevers in the same processing step. That means that the thickness of the support plane as well as the mask for etching of the cantilevers is the sum of the silicon nitride layer that was used as a mask in finding the location of the {111} planes and the layer that was deposited to serve as a mask for etching of the backside windows.

- The silicon nitride layer from which the tip plane is made is deposited next, using the same low stress LPCVD process as for all silicon nitride layers needed in the process. The patterns are defined using the ‘tip plane mask’ and an RIE step. The silicon nitride deposited on the back side of the wafer in this step forms the protection layer needed in the etching process of the cantilever described above.

- Next, the tip sharpening planes are defined. The chromium is deposited by evaporation and the layer is patterned using a lift–off process with the ‘sharpening plane mask’. Now the wafers are ready for etching of the cantilevers.

- After etching of the cantilevers, the blunt end of the tip plane is etched away using RIE. This also removes the now undesired silicon nitride layer on the side of the cantilever.

- The final step of the complete process is the removal of the chromium tip sharpening plane. This is done in a wet chemical etching process using a dedicated chromium–etchant.

3.4 Results

In this section the results that were obtained with the fabrication process described in the previous sections are presented. First the cantilever structure is discussed, followed by the tip plane structures.

3.4.1 The cantilever

Alignment to the crystal planes

As pointed out in section 3.2.3, one of the most crucial steps in the fabrication process of the CantiClever probe is the precise alignment of the mask, needed for etching of the cantilever structure, to the {111} crystal planes. With the alignment method described earlier, such a precise alignment could be achieved as can be seen from the symmetrical under–etching profile shown in figure 3.11. A 50 nm thick silicon nitride layer was used as a mask. The pattern was etched in a 25% KOH solution, that was kept at a constant temperature of 75°C, for 15 minutes. The arrows indicate the point to where the the structures are under–etched. Although it is difficult to see the difference between the two forks in figure 3.11, upon close inspection only one of the forks could clearly be pointed out as the best aligned structure. The small square on the left side of the symmetrically under–etched alignment fork was then used as one of the marks for aligning the subsequent 'alignment mark mask'.

Defining the width of the cantilever

After defining the alignment marks on the front side of the substrate, the next step in realization of the cantilever structure is the definition of the width of the cantilever. This is done as described in section 3.2. The wafers are thinned down to the desired width of the cantilever by etching a window at the backside of the wafer. The shape of this window is such that the base of the probe is shaped as depicted in figure 3.3, with the sides of the window aligned to the {111} crystal planes to obtain the vertical sidewalls.

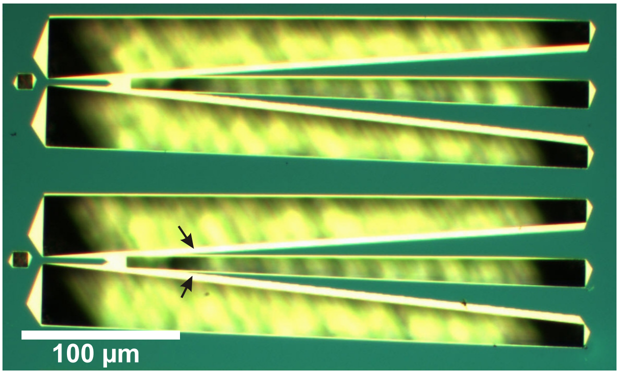

Figure 3.11: *Two under–etched alignment forks close to the* $\{111\}$ *crystal plane. The bright regions are the under–etched parts of the mask.*

The wafers that are used are around 400 microns thick. The width of the cantilever is set at 50 microns, so around 350 microns of silicon has to be etched away from the windows at the backside of the wafer. The same KOH process was used for etching the backside windows, but the silicon nitride mask was 200 nm thick. The masking layer consists of the layer used in the first etching step, covered with a 150 nm thick layer of silicon nitride that, at the front side, protects the alignment marks for the remaining processing steps from the KOH solution. The etch rate of the $\{110\}$ planes was 1.8 μm per minute, in agreement with the value obtained by Seidel *et al.* [115]. The process took more than three hours of etching. The final depth of the etched windows was determined by measurements with a Dektak profiler. The bottom surface showed a roughness of several microns as was expected from the experiments described in [117].

Etching of the cantilever

The final step in the fabrication of the cantilever structures is liberating the cantilever from the substrate by etching the remainder of the silicon wafer away from the front side. As pointed out in section 3.2, the sides of the cantilever mask should etch very slowly as they are being bound by the $\{111\}$ crystal planes. During the 50 minute etching process, hardly any undercutting of the sides of the mask was observed as can be seen from figure 3.12. This behavior is expected from the high etch rate ratio of $\langle 110\rangle$:$\langle 111\rangle$ reported in literature. Ratios of 50:1 to 160:1 are reported in [115] and even higher, up to 400:1, in [116].

An SEM image of the finished cantilever is shown in figure 3.13, showing the end of the holder part, the cantilever and the tip plane. If one looks carefully, one can distinguish the width variations of the cantilever due to the roughness of the bottom surface after etching from the back side. These variations should

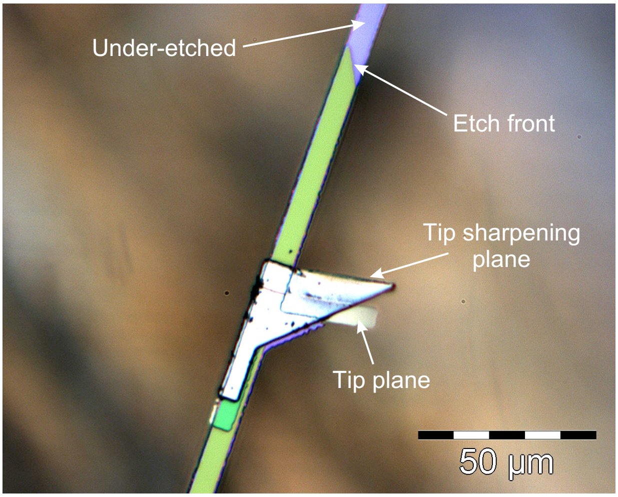

Figure 3.12: *The cantilever with the tip plane structures after 30 minutes of etching. Hardly any undercutting of the mask is visible at the sides. The under–etching profile at the front of the cantilever mask can clearly be seen.*

not have a major influence on the mechanical properties of the cantilever. The resonance frequency does not depend on the width of the cantilever, as shown earlier in equation 3.1. The variations in width also do limit the quality factor that can be achieved. When the cantilever vibrates in air, the quality factor is limited due to the damping by air [125]. Much higher quality factors can be achieved in vacuum. The quality factor in that case is independent of the cantilever width when the width is much larger than the thickness [108].

Zooming in on the end of the cantilever, as done in figure 3.14, reveals that the sides of the etched cantilever are also very smooth. No jumps can be seen, indicating that the alignment of the mask was very good.

In contrast with the sides of the cantilever mask, the front side is under–etched quite rapidly at a rate of nearly 4 μm per minute. The mask was corrected for this effect in such a way that the etching process could be stopped when the under–etch had reached the tip plane, resulting in the desired length of the cantilever.

3.4.2 The tip plane

As described in section 3.3, the total tip plane structure consists of a support plane and a tip plane. The support plane is made from the two masking layers that were used in the etching of the cantilever. The thickness of this plane is thus 200 nm. On top of this support plane, the silicon nitride layer from which the

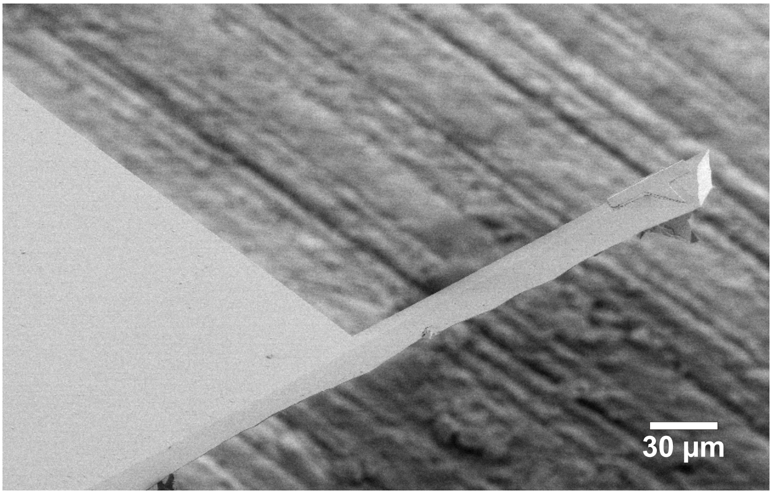

Figure 3.13: *The base of the probe with the complete cantilever and tip plane structures. The width variations due to the roughness of bottom surface can also be seen.*

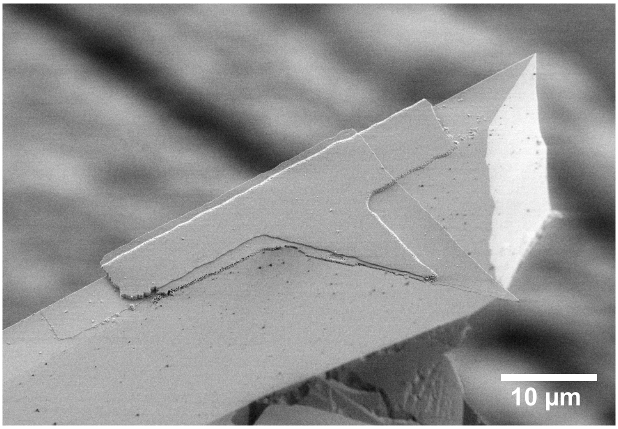

Figure 3.14: *SEM image the cantilever, showing the smooth sidewall and the front side as well as the tip plane structures.*

actual tip plane is made is deposited in the same low stress LPCVD process. A picture of the structure is shown in figure 3.15.

The next step is the sharpening of the tip plane using the chromium tip sharpening plane. This plane intersects the tip plane and any silicon nitride that sticks out under the sharpening plane is etched away. After the sharpening planes are defined the cantilever is etched free first, before any further process-

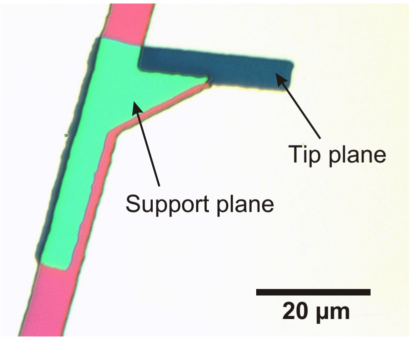

Figure 3.15: *Optical microscope image of the support plane and tip plane before the cantilever is etched free and the tip plane is sharpened.*

ing on the tip is carried out. This way, the chromium sharpening plane not only functions as a mask for sharpening of the tip plane, but also protects the fragile tip plane during the KOH etching of the cantilevers, as could already be seen in figure 3.12.

After the cantilever is etched free, an RIE process is used to etch away the blunt part of the tip. Also, the silicon nitride that was deposited on the back side of the wafer during the layer deposition for the tip plane is etched away. After the chromium is removed in a wet etching step with a dedicated chromium etchant, the structure looks like depicted in figure 3.16. The thicker support plane and the protruding tip plane are nicely defined. The stress in the layers deposited in the low stress LPCVD process proves to be low enough to prevent bending of the tip plane structures. Looking closer at the end of the tip plane in figure 3.17, the sharpening process proved to work very good as well. The estimated radius of curvature is around 30 nm, which is smaller than the tip plane thickness of 50 nm.

The support plane in the realized probes has a thickness of 200 nm. This value was kept constant for all of the probes. The thickness of the tip plane was varied from 100 nm downwards. Tip planes as thin as 37 nm have successfully been fabricated. This thickness of the silicon nitride layer proved to be sufficient to provide a good protection of the backside of the wafer and survival of the tip plane during the final cantilever etch.

3.5 Measurement of mechanical properties

In this section, the measurement of the mechanical properties of the cantilever of the CantiClever probe are described. The resonance frequency and the quality factor are measured in both air and vacuum. For this purpose, a dedicated

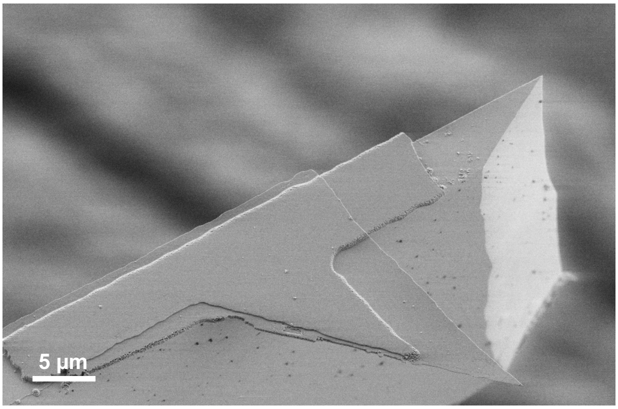

Figure 3.16: *The tip plane structures showing the support plane and protruding tip plane. The tip plane has a thickness of 50 nm.*

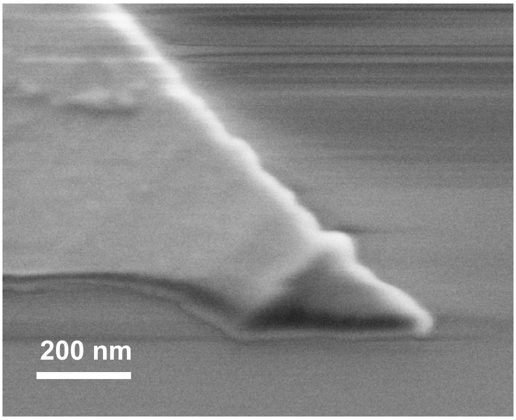

Figure 3.17: *Detail of the sharpened end of the tip plane. The radius of curvature is estimated to be less than 30 nm.*

setup was built, consisting of a small vacuum chamber with a rotary pump and a pressure gauge, an optical deflection detection system and an Agilent 4395A network– and spectrum analyzer. An image of the system is depicted in figure 3.18.

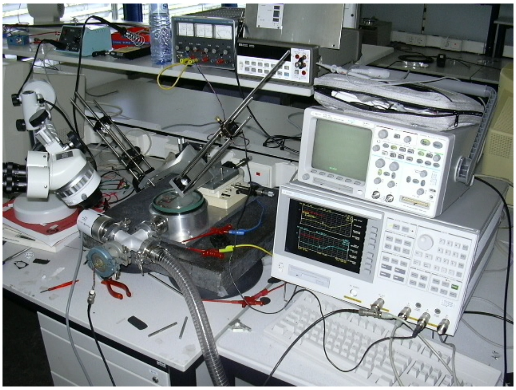

Figure 3.18: *Setup for measuring the resonance frequency and quality factor of the cantilever. In the center, the small vacuum system and the deflection measurement system can be seen.*

3.5.1 Resonance frequency of the cantilever

The resonance frequency of a cantilever beam is given by equation 3.1, that is repeated below for convenience:

$$f_0 = \frac{1}{2\pi} C_0^2 \frac{t}{l^2} \sqrt{\frac{E_{Si}}{12\rho_{Si}}}$$

The values of the resonance frequency were determined for two different cantilevers: the first one was designed to have a resonance frequency of 80 kHz and the second of 279 kHz. The dimensions of these two probes were measured using an optical microscope. The cantilever of the 80 kHz probe was measured to be 318 μm long and 4.7 μm thick. The resonance frequency of a cantilever with these dimensions, calculated from equation 3.1, is 67.6 kHz. Measurement of the resonance frequency of this probe in the setup resulted in value of 66.8 KHz. The cantilever of the 279 kHz probe was measured to be 175 μm long and 5.2 μm thick. This gives a calculated resonance frequency of 247.0 kHz. The measured value was however somewhat lower, at 210.0 kHz. The results are summarized in table 3.1.

From these measurements it can be concluded that the lower than designed value of the resonance frequency that was measured is due to the fabrication process. Although the etching process used to etch the cantilevers free from the substrate is highly anisotropic, a slight underetch still occurs. Furthermore, the frontside of the cantilever is underetched at a very high rate, as described in chapter 3.4.1. As the resonance frequency is stronly dependent on the length of the cantilever, a deviation of the resonance frequency will occur if the etching process is not stopped at the correct time, while a inhomogeneity in the etching process causes the resonance frequency to change over the wafer.

length	thickness	$f_{0,\text{ designed}}$	$f_{0,\text{ measured}}$	Q_{air}	Q_{vacuum}
318 μm	4.7 μm	80 kHz	67 kHz	600	50000
175 μm	5.2 μm	279 kHz	209 kHz	900	7000

Table 3.1: *Mechanical properties of the cantilever.*

3.5.2 Quality of resonance

As already pointed out in chapter 2.1.2, the thermomechanical noise of the cantilever sets a limit to the ultimate resolution that can be achieved in an MFM. This noise can be lowered by increasing the quality factor Q, as shown in equation 2.7. The quality factor is defined as [125]:

$$Q = \frac{2\pi U_i}{U_d} \tag{3.2}$$

where U_i is the vibration energy stored in the cantilever and U_d the dissipated energy per period. At atmospheric pressure, Q is limited by the damping caused by the surrounding air molecules. This can be overcome by measuring in vacuum. At pressures lower than $1 \cdot 10^{-2}$ to $1 \cdot 10^{-3}$ mbar, Q is no longer pressure limited [57, 108]. In that case, other dissipation phenomena become important in determining the value of Q, such as clamping losses (dissipation via coupling to the support structure) [126] and by internal friction. Internal friction results from various mechanisms such as thermoelastic dissipation (TED), volume and surface effects. The total value of Q can then be determined from [108]:

$$\frac{1}{Q} = \frac{1}{Q_{\text{clamping}}} + \frac{1}{Q_{\text{TED}}} + \frac{1}{Q_{\text{volume}}} + \frac{1}{Q_{\text{surface}}} + \frac{1}{Q_{\text{other}}} \tag{3.3}$$

The frequency response of the 67 kHz and the 210 kHz probe were measured at atmospheric pressure and at $2 \cdot 10^{-2}$ mbar, which was the lowest pressure that could be achieved with the setup. The value of Q was then calculated by fitting the theoretical transfer function of a damped harmonic oscillator (see for instance [57]) to the measurement points. The value of Q of the 67 kHz probe at atmospheric pressure was determined at approximately 600. When moving to vacuum, the value of Q increased to around 50000. The measured response and the fit are depicted in figure 3.19. While the 210 kHz probe had a larger value of Q than the 67 kHz probe at atmospheric pressure, that is approximately 900, the value under vacuum conditions was much lower at around 7000. The

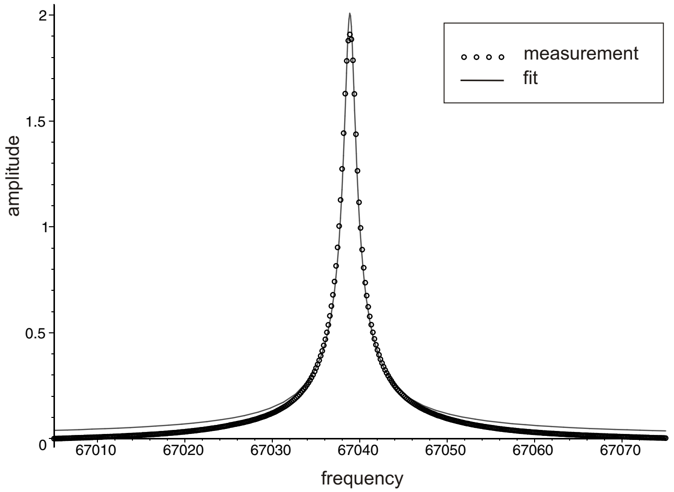

Figure 3.19: Measured frequency response and fit of a 67 kHz cantilever in vacuum.

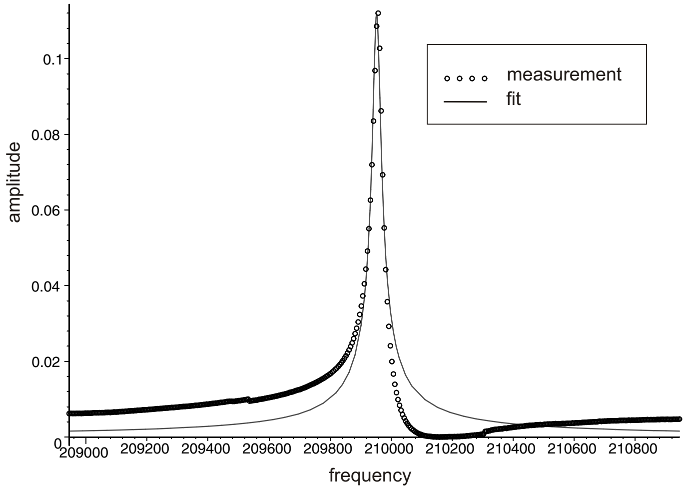

Figure 3.20: Measured frequency response and fit of a 209 kHz cantilever in vacuum.

measurement and fit of the response of the 210 kHz probe in vacuum are shown in figure 3.20. The results of the measurements are summarized in table 3.1.

The quality factor of the cantilever of the CantiClever probe are comparable to those of other silicon cantilevers. The high value of Q under vacuum conditions should allow very sensitive measurements with the CantiClever probe. It is however not quite clear why the quality factor of the 210 kHz probe is lower in vacuum than that of the 67 kHz probe. Although TED is more eminent at higher resonance frequencies [108], the values used here are well below the frequencies where TED becomes dominant. Also clamping loss is unlikely to be the dominant factor, as it is proportional to t^3/l^3 [126]. For the dimensions of the cantilevers measured here, the value of Q_{clamping} is much larger than the value of Q that was measured. More investigations will be necessary to determine the cause of the lower value of Q.

3.6 Conclusion

In this chapter, the fabrication process of the CantiClever probe has been described. The probe was designed with the use of a parameter based software package. This proved a convenient and accurate method to transform properties such as the cantilever resonance frequency into corresponding dimensions of the probe. The initial effort that was put in programming of the basic shapes of the probe paid off at a later stage as the design proved to be very flexible and easy to modify.

After a consideration of several fabrication processes, it was decided to etch the cantilever and base of the probe out of $\langle 110 \rangle$ oriented silicon wafers, using a two step KOH wet anisotropic etching process. Due to the highly accurate alignment of the mask to the crystal planes it was possible to precisely control the dimensions of the cantilever. No significant under–etching of the sides of the cantilever mask could be observed. The under–etching of the front side of the mask could be easily compensated for.

The tip plane was made from silicon nitride, deposited in a low–stress LPCVD process. This material proved to meet the demands placed upon the tip plane material: stiff in order to prevent bending during scanning with the tip, low stress to obtain a free hanging structure over a large range that does not bend and finally the ability to withstand the cantilever etching process. The very sharp cut-off corner of the tip plane needed to obtain high resolution tips for MFM could also be realized. By means of reactive ion etching using a Cr mask layer, the blunt end of the tip was removed and a radius of curvature as small as 30 nm could be achieved using a 2 micron lithography process. Tip planes as thin as 37 nm could be successfully fabricated.

The mechanical properties of the cantilever of the CantiClever probe were measured. It was found that they are comparable to those of other silicon cantilevers. The value of the resonance frequency was lower than designed, due to the fabrication process. The high value of Q, up to 50000 under vacuum conditions, should allow very sensitive measurements with the CantiClever probe.

Chapter 4

The integration of a magnetic tip

This chapter describes the integration of a magnetic tip on the tip plane of the CantiClever probe, characterization of its magnetic properties and the MFM measurements that were carried out with the probe. To be able to characterize the magnetic properties of the tip dedicated test structures, containing an array of tips, were made as described in the first section. In the second section, an analysis is presented of the magnetic properties of the tip, that are of importance for imaging and probe recording. The integration of a magnetic tip on the CantiClever probe itself is the topic of the third section. In the last section, the results that were obtained with the probe in magnetic imaging, when mounted in an MFM are presented.

4.1 Magnetic tips on a wafer scale

To obtain a better understanding of the behavior of the magnetic tip in magnetic imaging or probe recording applications, it is necessary to investigate the magnetic properties of the tip. Especially the domain state (when used for magnetic imaging) and the switching field (in probe recording applications) are of importance. Because the magnetic tip of the CantiClever probe is very fragile and the amount of magnetic material of a single tip is very small, measurement of these properties on the CantiClever probe itself is very difficult. Therefore, it was decided to fabricate test structures for this purpose that feature an array of many magnetic tips on a 100 mm wafer [127]. The design of these test structures and the results that were obtained are described in this section, the measurements of the magnetic properties in the next section.

4.1.1 Design of the test structures

Requirements

The objective is to fabricate an array of tips similar to those on the CantiClever probe, that can be studied using a number of different measuring instruments. Two sources of requirements on the array of tips can be distinguished:

- The design of the CantiClever probe is the first source of requirements. The probes feature a 20 microns long tip plane made of silicon nitride, that has a thickness below 200 nm. When magnetic material is deposited on the side of the tip plane, a magnetic tip is formed that has a length of 20 microns and a cross section in that is in the nanometer range. To ensure that the magnetic tips on the test structures are similar to those on the CantiClever probe, free hanging silicon nitride planes with a thickness in the nanometer regime need to be made on the test structures as well.

- The measuring instruments that will be used to study the magnetic properties of the magnetic tips are the second source. The instruments pose restrictions on the design of the test structures in terms of height differences, amount of total magnetic moment and size of the sample. The test structures will be measured with four different instruments. The MFM will be used to look at the domain structure of a single tip. Because the MFM has a slow response to steep and big height differences on the sample, these need to be as small as possible, but at least smaller than 1 micron [128]. A vibrating sample magnetometer (VSM) or a SQUID magnetometer will be used to study the switching behavior of an array of tips. These two instruments have a limited sensitivity and can accept only samples up to a certain size. The sensitivity and sample size of the VSM and SQUID are $1 \cdot 10^{-8}$ Am^2 and 1×1 cm^2 and $1 \cdot 10^{-11}$ Am^2 and 8×8 mm^2 respectively. The switching behavior of the magnetic tips can also be studied with the use of magneto–resistance (MR) measurements as described in literature [129, 130, 131]. This method enables the study of the switching behavior of an individual tip, but requires electrical connections to the individual tips. To be able to carry out MR measurements, some of the tips have to be equipped with electrical connections.

Tip placement

On the CantiClever probe, the magnetic material is deposited by means of evaporation on the side of a free hanging plane, described in more detail in section 4.3. An identical process, using the same magnetic material (cobalt), will be used on the test structures, but here the deposition is done under a small angle

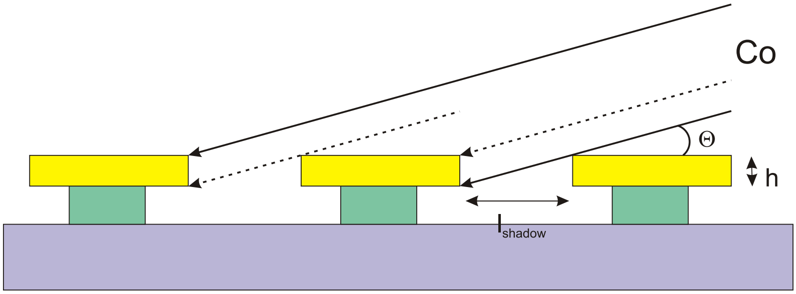

Figure 4.1: The shadow effect in the deposition of cobalt under an angle.

of approximately 3° instead of perpendicular to the side of the plane. If the deposition would be done perpendicular to the side of the plane, the shadow of adjacent elements would prevent the cobalt to be deposited on all the planes. This is illustrated in figure 4.1.

The length of the shadow, where no material will be deposited, depends on the angle between the evaporation source and the substrate and the thickness of the silicon nitride planes:

$$l_{shadow} = \frac{t_{planes}}{\tan\theta} \tag{4.1}$$

Where l_{shadow} is the length of the shadow, t_{planes} the thickness of the silicon nitride planes and θ the angle of evaporation. The length of the shadow is the minimum distance that the islands must be separated in the direction of evaporation. With a deposition angle of 3° and a maximum thickness of the silicon nitride planes of 200 nm the length of the shadow becomes 3.82 μm. The separation must thus be larger than 3.82 μm and is set at 5 μm. As the material is evaporated under an angle instead of perpendicular to the side of the planes, the cobalt is also deposited on the top of the planes. This film is very thin compared to the film present on the sides of the planes. If the evaporation source is assumed to be a point source, i.e. all material originates out of one point, the thickness can be calculated from the following formula [132]:

$$t = \frac{m}{4\pi\rho} \cdot \frac{\cos(90-\theta)}{r^2} \tag{4.2}$$

Where t is the thickness of the evaporated layer per unit time (m/s), m the evaporation rate (kg/s), ρ the density of the evaporated material (kg/m^3), θ the angle of evaporation and r the distance between the point source and the substrate

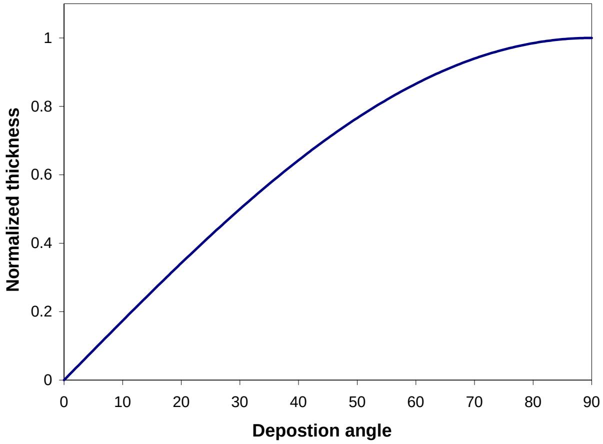

Figure 4.2: *Relation between the thickness of the evaporated film and the angle of evaporation.*

(m). The dependence of the (normalized) film thickness on the angle of evaporation calculated using equation 4.2 is plotted in figure 4.2. From this figure it can be seen that if a small angle of evaporation is used, the thickness of the layer deposited on the top of the planes will be very small compared to the thickness of the tips, that are deposited on the side of the planes. In case of an angle of 3°, the thickness on the top of the planes is only 5% of the thickness of the tips.

As it is the aim of the test structures to study the behavior of only one magnetic tip, there should not be any magnetic dipolar interactions between the tips in the array. Research on arrays of ferromagnetic nanowires shows that the wires are magnetically uncoupled when the ratio between the separation between the wires and their width is at least 1:1 [133, 134]. The separation between the tips in the direction of evaporation is large enough to prevent magnetic dipolar interactions due to the shadow effect. Using the 1:1 separation–width ratio as a rule of thumb, the distance between the ends of the tips is set at 20 microns, the same as their length. Therefore it is assumed that the magnetic dipolar interactions between the tips in the array can be neglected.

With the density of the tips resulting from the arguments given above, the total saturation magnetization of the array of tips can be calculated to see if the sensitivity requirements of the VSM can be met. The magnetic moment of a test sample can be calculated from:

$$M_{sample} = A_{sample} \cdot D_{sample} \cdot V_{tip} \cdot M_{s,cobalt} \tag{4.3}$$

Where A_{sample} is the area of an array of tips, set at 8×8 mm^2, D_{sample} the density of tips on the sample, V_{tip} the volume of a single tip and $M_{s,cobalt}$ the saturation magnetization of cobalt: 1440 kA/m. For tips with a square cross–section of 200×200 nm^2 and 50×50 nm^2 the expected magnetic moment is $18.2 \cdot 10^{-8}$ Am^2 and $1.1 \cdot 10^{-8}$ Am^2 respectively. This should be just sufficient to measure the samples on the VSM.

Layout

The layout of one sample with test structures is shown in figure 4.3. On a 100 mm wafer, there are 64 of these samples. Each sample measures 8×8 mm^2 and contains around 160,000 tips. The silicon nitride planes are always 5 microns wide, but the length is varied from 14 up to 35 μm. On each sample, there are 16 electrodes present that connect to 4 of the tips at the edge of the sample. This enables MR measurements to be done with a 4 point measurement method.

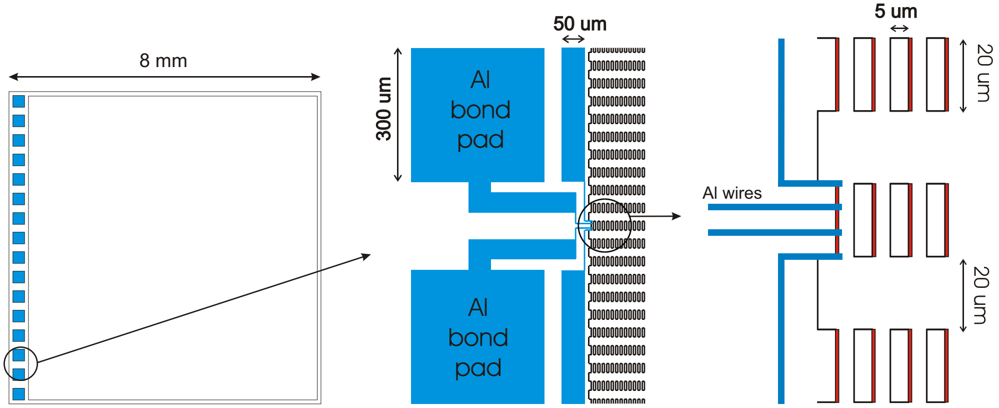

Figure 4.3: The design of a single sample with test structures. Left: top view of the complete 8×8 mm^2 sample. The white area is completely filled with tips. Middle: the bondpads and electrodes. Right: connection of the electrodes to the tips. The tips are located at the right side of every island.

4.1.2 Fabrication process

The test structures are fabricated using a four mask process. The masks were designed using the method described in chapter 3.1.1. Only an overview of the process is given in this section, the complete description of the process can be found in the appendix. A cross section of the sample during the fabrication process is schematically depicted in figure 4.4. The numbered steps in the following section all refer to this figure.

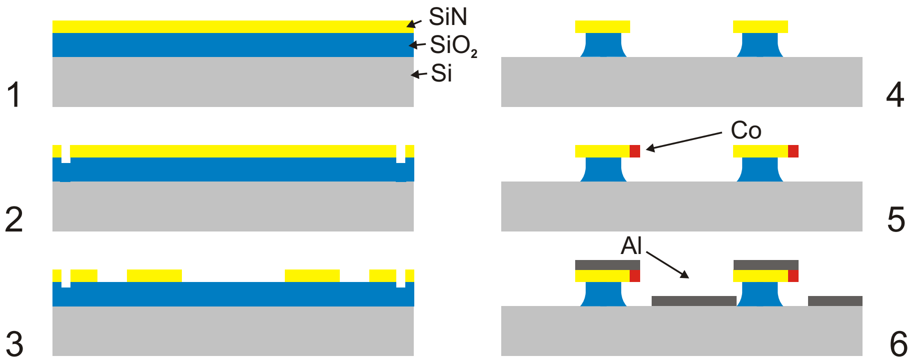

Figure 4.4: *Processing steps of the test structures.*

The process starts by growing a 400 nm thick silicon dioxide layer by wet oxidation at 1150°C on a 100 mm wafer. On top, a layer of non stochiometric low stress silicon nitride is deposited using the same LPCVD process as was used to make the tip planes of the CantiClever described in chapter 3.3. The cross section of the sample then looks like depicted in step 1. Two series of test structures were made, with thicknesses of 200 and 50 nm respectively. Subsequently, the alignment marks and dicing lines are defined using the first mask (step 2). The silicon nitride layer is then patterned into islands in two steps. First, the second mask is applied to pattern the continuous silicon nitride layer into strips over the complete length of the sample using RIE with photoresist as the masking material. The strips are then cut into islands with a similar process. However, instead of photoresist, a chromium mask is used during the RIE step that is deposited in a lift–off process using the third mask. This ensures that the side edge of the silicon nitride plane is completely vertical. The same process was used to obtain a flat tip end on the CantiClever probe described in the previous chapter. The resulting islands have square corners and two vertical side edges (step 3). After that, the silicon dioxide layer is partly etched away using a 50% HF solution. As this is an isotropic etching process, the silicon nitride layer is under–etched, leaving the edges of the islands hanging free, as can be seen in step 4. When subsequently the magnetic material is deposited on the side of the islands (step 5), the shape of the magnetic tip will be the same as those present on the CantiClever probes. With the fourth mask the electrodes are defined. The aluminum that is patterned by a lift-off process is evaporated under an angle of 60° to avoid shortcuts to the silicon substrate (step 6). When MR measurements are done, contacts to the tips can be made using wirebonding.

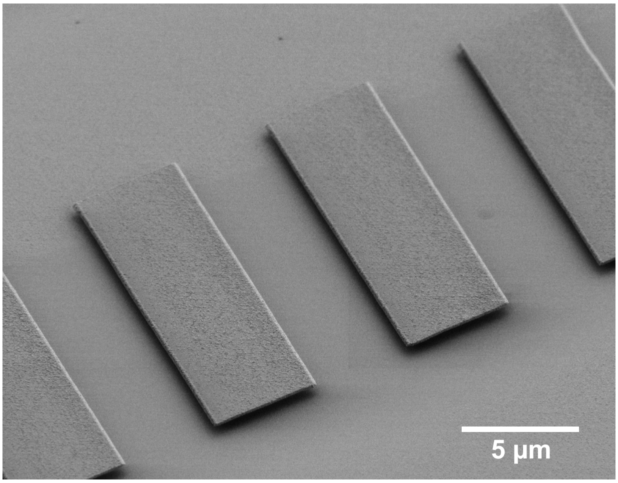

Figure 4.5: *Test structures with* 17×5 μ*m planes.*

4.1.3 Results

Free hanging planes

The SEM image of figure 4.5 shows the silicon nitride planes, with a thickness of 200 nm after etching of the silicon dioxide layer. The 17×5 μm planes are very nicely defined and have the desired square corners. The edges of the planes hang freely above the sample surface. The isotropic under–etching of the planes is depicted in more detail in figure 4.6. The samples were etched in HF for one minute. After that, the planes showed an under–etch of approximately one micron. The edges of the planes are completely free from the substrate as desired. The discontinuous film that covers the sample results from a cobalt deposition, that was already done on this sample.

The square corners of the planes are important for the magnetic properties of the tips that will be deposited on the sides of the planes. One corner of a plane is depicted in the SEM image of figure 4.7. The corner shown is not rounded but perfectly square. The definition of the islands in two steps has created the desired effect. The corners were not damaged in the HF etching step.

Magnetic tips

The magnetic material that forms the tips was deposited in an e–beam evaporation system. The material evaporates from a rather small melt (around 0.3 mm), 42 cm away from the sample. This distance is large enough to justify our approximations of a point source. The evaporation angle of 3° could be set using

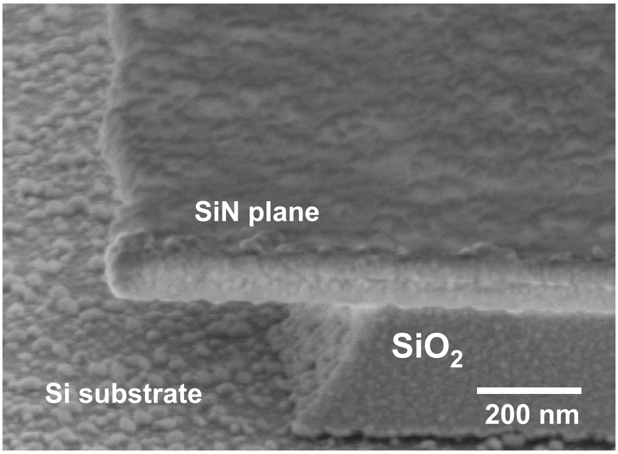

Figure 4.6: *Isotropic under–etching profile below a 57 nm thick plane.*

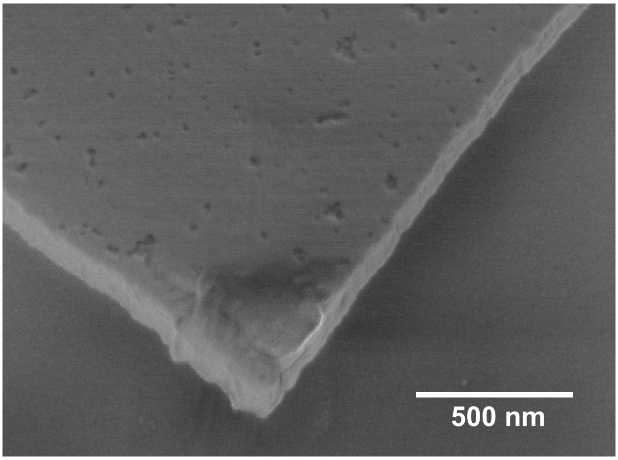

Figure 4.7: *Square corner of a 50 nm thick plane.*

a specially designed wafer holder. Two sets of samples were used, one set with 214 nm and one with the 50 nm thick silicon nitride planes. The thickness of the evaporated cobalt was verified with a 1×1 cm^2 test sample that was measured in the VSM. The magnetic moment of the sample at saturation was then used to calculate the thickness of the evaporated cobalt layer, using the bulk saturation magnetization of Co (1440 kA/m). In total, four different wafers with tips were produced:

- 214 nm thick planes with 163 nm of cobalt

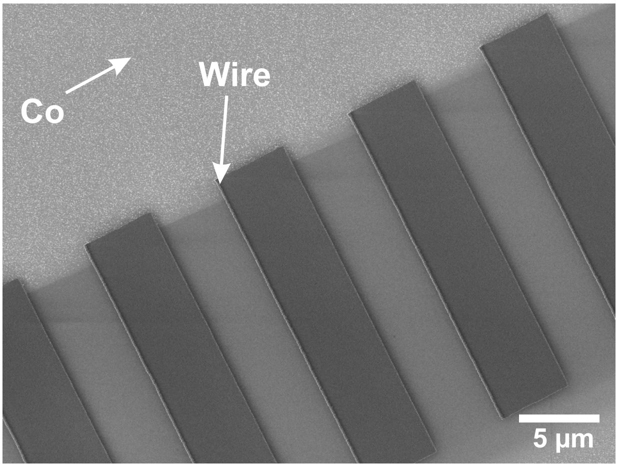

Figure 4.8: *Magnetic tips deposited on the side edge of 214 nm thick planes. The direction of evaporation is also shown.*

- 214 nm thick planes with 118 nm of cobalt
- 57 nm thick planes with 103 nm of cobalt
- 57 nm thick planes with 54 nm of cobalt

From these four samples, two of them were investigated using the SEM. The samples with the 214 nm thick planes and 163 nm of cobalt are depicted in figure 4.8 to figure 4.10. From the images can be concluded that the shadow evaporation on the side edges of the planes was successful. The cobalt, distinguishable by the brighter areas in figure 4.8, is present on the sides of the planes, but not in front and at the back of them.

As can be seen from figure 4.9, the cobalt doesn't cover the complete side of the silicon nitride plane. The angle of evaporation was below 3°, the angle for which the test structures were designed. The angle in this case, estimated from the SEM images, was 1.1°. However, one of the ends of the plane was completely covered with cobalt. This was caused by a slight misalignment of the wafer with respect to the evaporation source. The angle between the normal to the side edge and the source was less than 90°, so that the corner of the plane was not in the shadow region of its neighbor.

The tips that were made by evaporation of 103 nm of cobalt in the samples with 57 nm thick planes are shown in figure 4.11. In this case the alignment with respect to the evaporation source was better: the complete side edge of the planes was covered with cobalt and the width of tips was constant along the complete length of the plane.

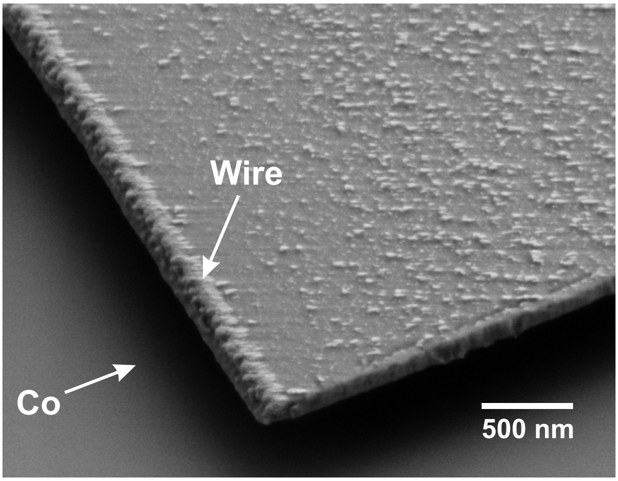

Figure 4.9: *Magnetic tip deposited on the side edge of a 214 nm thick plane.*

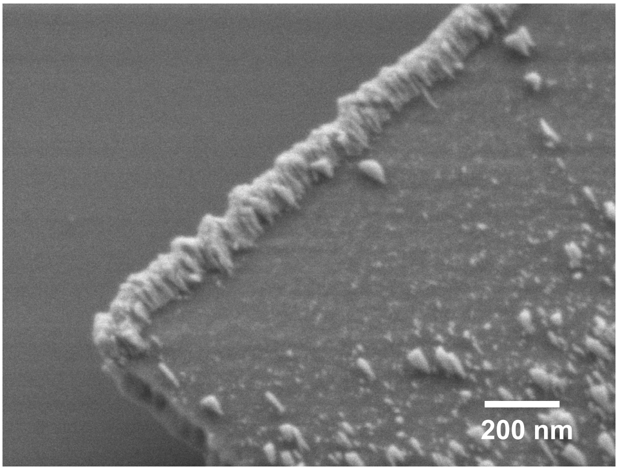

Figure 4.10: *Close–up SEM image of a magnetic tip deposited on a 214 nm thick plane, showing the columnar structure of the Co film.*

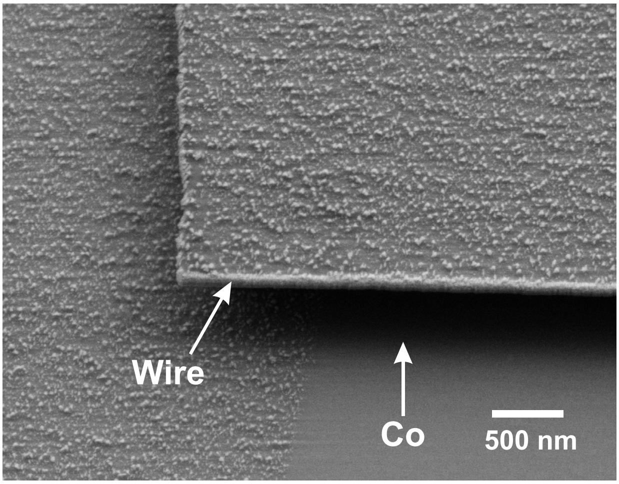

Figure 4.11: *Magnetic tip deposited on the side of a 57 nm thick plane. Note the shadow effect: no cobalt is deposited in front of the plane.*

A closer look at the tip, figures 4.9 and 4.10, reveals that the tip consists of densely packed, small cobalt columns. This structure is a result of the low mobility of the cobalt particles on the cold substrate and shadowing effects that occur during growth caused by the evaporation under an angle [135]. The column tilt angle depends amongst others on the angle at which the cobalt particles arrive at the surface [136, 137]. In this case, the angle is determined by the angle of evaporation and the tapering of the side edges of the planes. For the small angles of evaporation used here, this results in an easy axis of the anisotropy along the long axis of the deposited tips [138]. At the edges of the plane, the angle of evaporation will be much larger. The cobalt deposited here will have an easy axis oriented parallel with respect to the incidence plane of the atoms during deposition. This will counteract the anisotropy due to the shape of the tip and the contribution of the columns deposited at the low angles. Fortunately, the amount of material deposited in those areas is very small for the thicker planes. For very thin planes, such as the tip planes present on the CantiClever probe, columns at different angles, that could lower the anisotropy, will not be present at all. The experiments described in [138] were done with large area samples. Here, there will be simply not enough room for this effect to occur. Already on the thinnest test structures, the inclined columns are not present anymore.

Electrodes

The electrodes were made on one wafer that had 103 nm of cobalt deposited on 57 nm thick planes. The fabrication process consisted of evaporation of 100

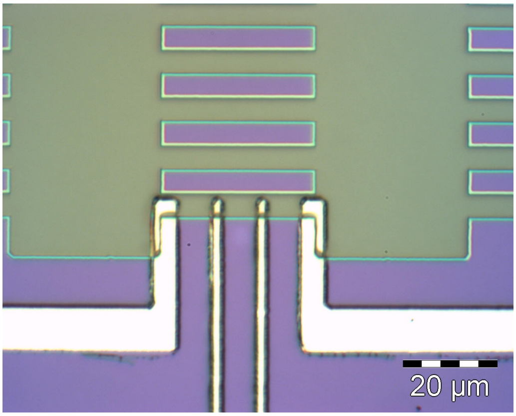

Figure 4.12: *Aluminium electrodes to the magnetic tip deposited using lift–off.*

nm of aluminum, using the same e-beam evaporation system that was used to deposit the cobalt. The excess of aluminum was then removed by a lift–off step in acetone. It proved hard to get rid of the excess aluminum, and as a result the lift-off process was only partly successful. Only 9 out of 48 samples had nicely separated wires, the other samples showed short circuits between them. One of the samples is shown in figure 4.12.

A closer look shown in figure 4.13 reveals the cause of the problems encountered in the lift–off step. Aluminium was also deposited on the sidewalls of the photoresist structures, greatly reducing the amount of photoresist that is exposed to the acetone. The aluminum sidewalls created another problem: the electrodes are shortened to the substrate.

To obtain some samples for MR–measurements, this problem was solved on some samples with the help of focussed ion beam (FIB) milling [139]. As shown in figure 4.14, parts of the vertical aluminum structures are sputter–etched away by the ion beam. This removed the shortcut between the electrodes while leaving the cobalt tip intact.

4.2 Properties of the magnetic tip

This section presents an investigation into the properties of the magnetic tip. Using the test structures described in section 4.1, the domain state and the switching behavior of the magnetic tip were investigated with MFM and VSM respectively. The switching behavior is also studied with micromagnetic simulations.

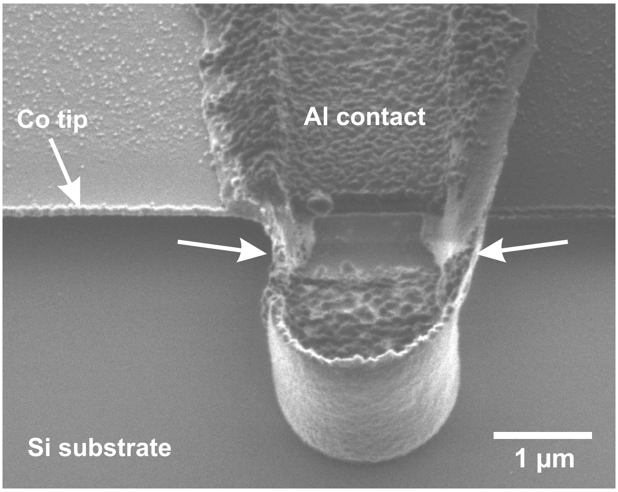

Figure 4.13: *One of the electrodes to the magnetic tip, that has a shortcircuit through the substrate, indicated by the arrows.*

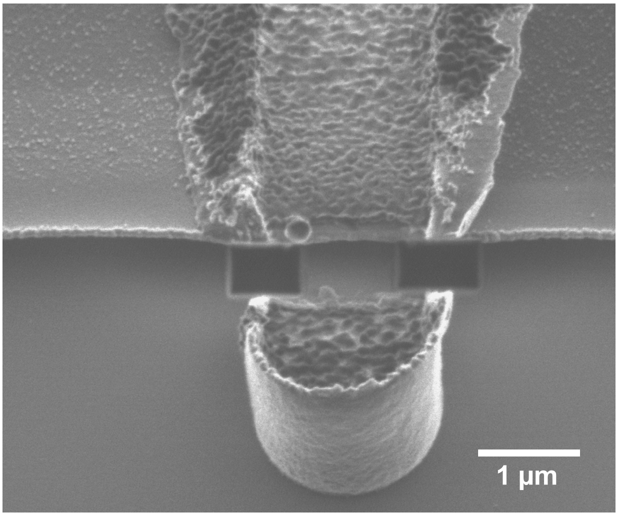

Figure 4.14: *The connections of the electrode to the substrate are removed by FIB milling.*

4.2.1 Domain state of the tip

The ideal tip for use in magnetic force microscopy is a single–domain magnetic particle with an elongated bar shape, as described in chapter 2. To verify if the magnetic tip of the CantiClever probe has a similar magnetic behavior, the magnetic domain state of the tip was studied on the test samples described in the previous section.

The measurements were carried out using a Dimension 3100 scanning probe microscope from Digital Instruments [140] in lift–mode. The tip that was used was a Force Modulation tip from Nanosensors with a tip radius less than 10 nm [106]. This tip was coated in–house on one side with a 10 nm chromium seed layer, a 50 nm cobalt layer and a 18 nm chromium capping layer. Without the chromium layers, the MFM tips were not very durable, the magnetic signal decayed severely within a couple of days, presumable due to oxidation of the cobalt. The chromium layers are deposited to protect the cobalt from oxidizing. These MFM tips showed an enhancement of the magnetic signal and a strong increase in durability. Several weeks after deposition, the tips showed no significant loss in magnetic signal. To avoid any confusion, the probe mounted in the microscope will be referred to as 'MFM tip' and the magnetic needles present on the test structures as 'tips' throughout this section.

The domain structure was studied on samples that had $17 \times 5\ \mu\mathrm{m}^2$ silicon nitride planes with a magnetic tip having a cross-section of $100 \times 163\ \mathrm{nm}^2$ deposited on the side–edge. An SEM image of such a tip is shown in figure 4.9. The sample was first imaged immediately after the deposition of cobalt (as–deposited). The resulting image is depicted in figure 4.15. Unfortunately, some topographic cross–talk shows up in the MFM image. The microscopy was still unable to accurately follow the surface of the sample in lift–mode, despite the slow scan rate. The domain state of the tip can still clearly be distinguished however. The black spots in the image represent attraction, the white spots repulsion between the MFM tip and the sample. A single magnetic domain can be distinguished in the image by a black and white spot caused by the magnetic stray fields at the boundaries of the magnetic domain. In the figure multiple black and white spots can be seen, corresponding to a multi–domain state of the sample, as indicated by the schematic drawing. The high shape anisotropy of the tip causes the domains to align parallel or anti–parallel to the wire axis. The multi–domain configuration results from the fact that during deposition, no magnetic field was applied parallel to the wire. As the tip is not continuous during its growth, multiple, anti–parallel domains are formed by chance. When the tip eventually becomes continuous, structural defects could pin the domain walls [141].

In figure 4.16 MFM images are shown after a magnetic field of 800 kA/m was applied parallel to the axis of the tips. The black and white spots are now only

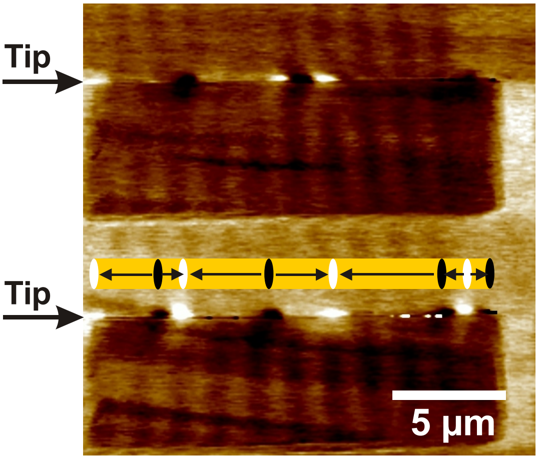

Figure 4.15: *MFM image showing the domain state of the as-deposited tip. The magnetic tip can be recognized by the black and white contrast on the top of the square patterns, as indicated by the arrows. A possible domain state is depicted in the schematic drawing.*

present at the edges of the cobalt tip, indicating that the tip now consists of only one magnetic domain. The domain walls could thus be removed by application of a magnetic field along the tip axis, as also found by [141] and [142].

Next to the black spots visible in the left image of figure 4.16 small white spots can be observed as well. This phenomenon occurred in all MFM measurements on the test samples. Dependent on the scan direction, small white spots were visible next to the black spots or small black spots next to the white spots. The small spots could only be seen when the MFM tip descended from the silicon nitride plane onto the silicon substrate below. An explanation for the appearance of the small spots could be the following. As the MFM tip scans the tip on the test structure and approaches the end of the tip, the MFM tip is e.g. attracted by the stray field at the end of the tip. This depends on the magnetization direction of both the MFM tip and tip on the sample. As long as the MFM tip is still above the end of the tip, a downward force will act on the tip and a black spot will appear on the image. When the MFM tip has descended from the silicon nitride plane to the region below the tip–end, the MFM tip is still attracted by the stray field of the tip–end. However, the force now acts on the tip in the upward direction and a white dot appears in the MFM image. The appearance of the small dots only when the tip is descending could occur because the MFM tip follows the surface of the sample differently when it rises then when it descends. This difference could be a result of the settings of the tip to sample distance control loop. From this it can be concluded that the presence of a small

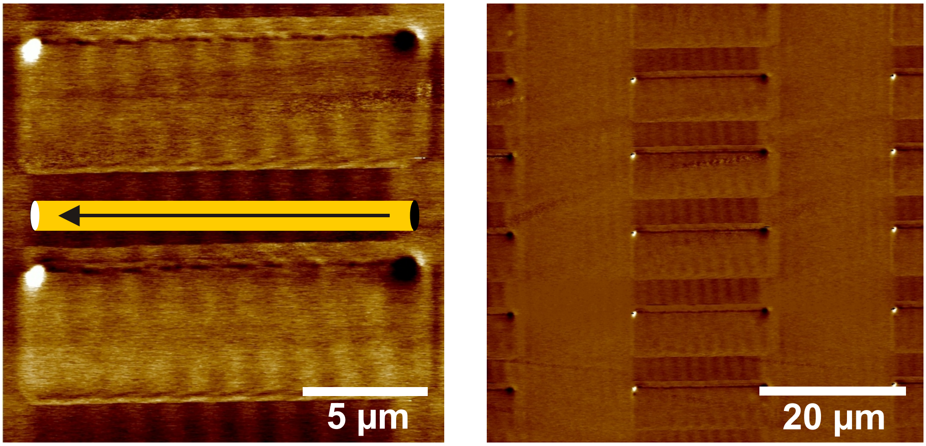

Figure 4.16: MFM images of the tips after saturation in a magnetic field parallel to the long axis of the tips. The domain configuration of a single tip can be seen in the left image. The complete array showed the same domain configuration (right image).

domain at the end of the sample is an artifact of the measurement rather a small domain at the end of the tip.

Figure 4.17 shows an MFM image of the tips after a magnetic field of 800 kA/m was applied perpendicular to the long axis of the tips. Now dark spots can be seen at the tip–ends and a white spot in the middle of the tip. This shows that the domain configuration has changed to a two–domain state, as depicted in the small inset sketch. This domain structure is formed after the magnetic field is reduced to zero. The magnetization rotates clockwise or counter–clockwise back to a direction parallel to the long axis of the tip. So by applying a magnetic field perpendicular to the long axis of the tip we can change the single–domain configuration of the tip into a multi–domain configuration. This is consistent with other experiments described in literature [141, 142].

4.2.2 Switching behavior

When the CantiClever probe is used in probe recording experiments, the magnetic field required to switch the tip is a very important parameter. This value needs to be lower than the coercive fields of typical media used for probe recording, as pointed out in chapter 1.2. An investigation into the switching behavior of the magnetic tip of the CantiClever probe is presented in this section.

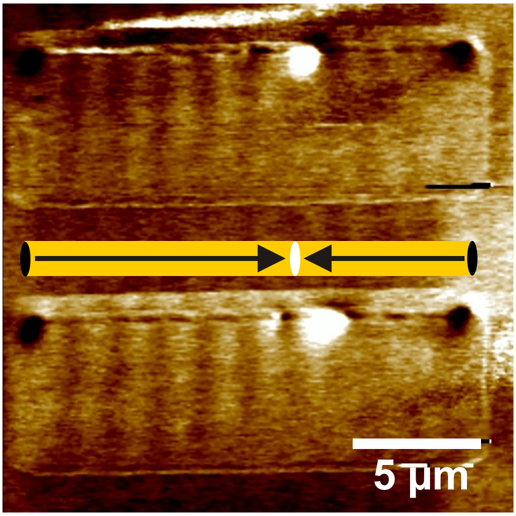

Figure 4.17: *MFM image showing the domain state of the tip after saturation in a magnetic field perpendicular to the long axis of the tip.*

Measurements

The switching behavior was studied with VSM measurements of the hysteresis loop of an array of tips. Because the amount of magnetic material on the test samples is very small compared to a sample with a continuous magnetic film, the measurements were complicated by unwanted contributions to the magnetic signal from the sample holder and the substrate of the test samples. To overcome this problem, a reference test sample without magnetic material was measured first. After the test sample with the cobalt tips was measured, the response of the reference sample was subtracted from the VSM measurements. This procedure was repeated for every measurement.

For all four different samples described in section 4.1.3, the hysteresis loop was measured. The magnetic field in all of the measurements was aligned parallel to the long axis of the tips. The hysteresis loops of the samples that contain 214 nm thick silicon nitride planes are shown in figure 4.18. The width of the cobalt tips is smaller than the thickness of the planes, as explained before. The thickness was determined from VSM measurement of a calibration sample. The thickness of the tips on the samples was 163 and 118 nm. The length of the tips was 35 and 29 μm respectively.

In figure 4.19, the hysteresis loops of the tips deposited on the 57 nm thick planes are depicted. The thickness of the cobalt layer was in these cases 103 and 54 nm. The length of the tips on these samples was 35 and 29 μm respectively.

The hysteresis loop of all the tips first show a small decrease when the field

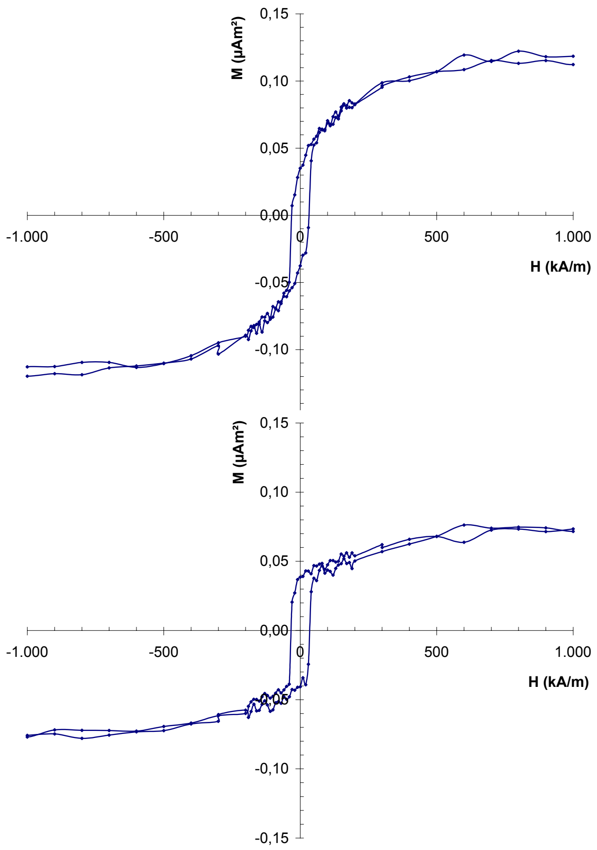

Figure 4.18: *VSM hysteresis loop of* $100 \times 163 \times 35000$ *nm*^{3} *(top) and* $100 \times 118 \times 29000$ *nm*^{3} *tips (bottom).*

is reduced from saturation followed by a sharp change into the reversed direction at the coercive field strength. Experiments done by others show a similar switching behavior [143, 144, 145, 131]. The macroscopic magnetic properties of the four samples have been determined from the hysteresis loops and summarized in table 4.1.

The value of the magnetic moment should drop as the volume of the tips decreases. The results from the VSM measurements do not show this trend. The remanent magnetization of the sample that has tips with a volume of $57 \times 54 \times 29 \cdot 10^3$ nm^3 is even higher than that of the samples with tips that measure $57 \times 103 \times 35 \cdot 10^3$ nm^3 and $100 \times 118 \times 29 \cdot 10^3$ nm^3. This could be a result of the deposition method that was used. The shadow effect during the deposition may cause the variations in magnetic moment that we measured. On the samples with 214 nm planes the side edge was not completely covered. When

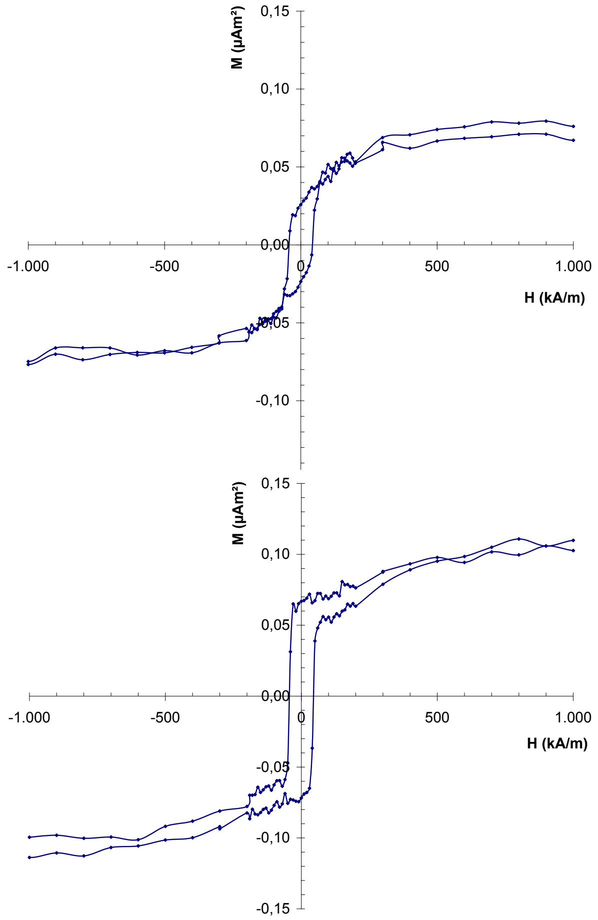

Figure 4.19: *VSM hysteresis loop of* $57 \times 103 \times 35000$ *nm*^{3} *(top) and* $57 \times 54 \times 29000$ *nm*^{3} *tips (bottom).*

Tip dimensions (nm^3)	Coercive field H_c (kA/m)	Saturation magnetization M_s (μAm^2)	Remanent magnetization M_r (μAm^2)	Squareness S
$100 \times 163 \times 35 \cdot 10^3$	38.5	0.12	0.04	0.33
$100 \times 118 \times 29 \cdot 10^3$	36.0	0.08	0.04	0.50
$57 \times 103 \times 35 \cdot 10^3$	47.5	0.08	0.03	0.38
$57 \times 54 \times 29 \cdot 10^3$	45.7	0.11	0.07	0.64

Table 4.1: *Magnetic properties of the cobalt tips obtained from VSM hysteresis loops.*

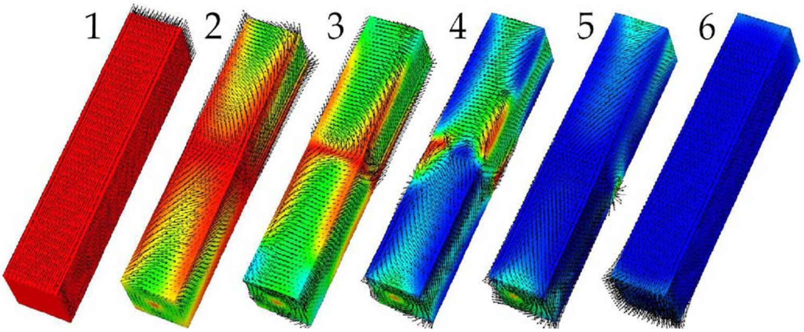

Figure 4.20: *Simulated switching behavior of a* $200 \times 200 \times 1000$ *nm*^{3} *tip.*

the same angle is used to evaporate the cobalt on the 57 nm thick planes, some material will be deposited on the side of the supporting silicon dioxide support structure. This extra amount of cobalt could contribute to the VSM signal. Another source of variations in the remanent magnetization are variations in the deposition angle. A 2° change of the deposition angle under the small angles used in our deposition system results in an approximately 0.6 μAm^2 change in magnetic signal. Finally, the thickness is dependent on the distance between the evaporation source and the substrate. This distance was not the same for all the samples, because they were not all taken from the same location on the wafer. This could also be an explanation for the differences in M_s that we measured.

Although the values of the switching field seem rather low, this doesn't mean that the magnetization of the tip switches easily when the tip is used for MFM measurements. The values presented in this section were measured in a uniform external field, whereas in MFM measurements, the stray field of the sample is only present very close to the sample. Then only a small part of the tip interacts with the stray field of the sample, and the magnetization of the tip will not switch easily.

Simulations

The magnetization reversal process of the tips was simulated by Hermann Forster from the Vienna University of Technology, during a three months stay in our lab. Using a finite element model [146], the switching behavior of a $200 \times 200 \times 1000$ nm^3 and a $20 \times 20 \times 14000$ nm^3 tip was simulated. The tip is assumed to be amorphous, so the crystalline anisotropy constant in the model is set to zero. Snapshots of the switching behavior of the $200 \times 200 \times 1000$ nm^3 tip are depicted in figure 4.20. Before the reversal process starts, the tip has a homogeneous magnetization parallel to the long axis of the tip. Then an external field

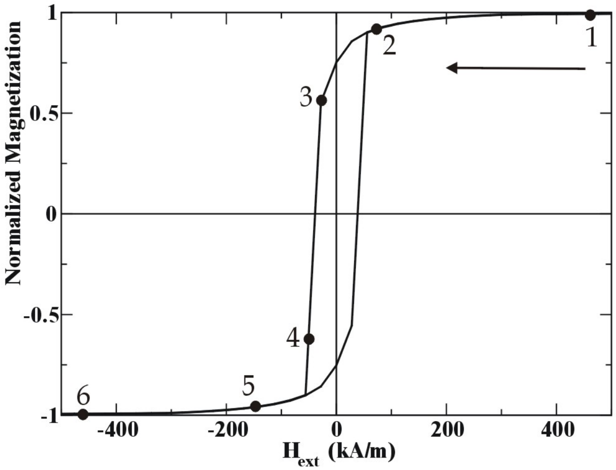

Figure 4.21: Simulated hysteresis loop for a $200 \times 200 \times 1000$ *nm*^{3} *tip. The numbered points in the loop correspond to the numbered domain states from figure 4.20.*

is applied parallel to the long axis of the tip but in the opposite direction. The reversal starts with the formation of small domains at the ends of the tip, where the magnetization rotates away from the magnetization direction of the rest of the tip. When the external field is high enough, the remainder of the tip switches rapidly in the opposite direction. The resulting hysteresis loop of the tip is depicted in figure 4.21. When returning from saturation, first the magnetization decreases slightly. In this regime, the domains at the ends of the tip are formed. At the switching field, the magnetization jumps over a very small field interval to the opposite direction. For the $200 \times 200 \times 1000$ nm^3 tip, a switching field of 32 kA/m is found. This switching behavior is in accordance with other micromagnetic models described in literature that simulate the switching behavior of similar structures (often called magnetic nanowires) [144, 147, 148]. These models agree with the simulations presented here on a type of non–uniform magnetization reversal where the reversal process starts with the nucleation of a small magnetic domain with an opposite direction of the magnetization, followed by the propagation of the domain walls. This reversal mechanism starts preferentially at the tip–ends or at defects within the tip and proceeds towards the center of the tip. The initial nucleation takes place in a range of the applied field whereas after the nucleation of a reverse domain the reversal can occur in a very narrow field region around the coercive field [149, 150].

Simulations of a much longer but thinner wire, with a cross–section of 20×20 nm^2 and a length of 14 μm, resulted in a hysteresis curve with a higher squareness compared to the loop depicted in figure 4.21. This is expected because the relative contribution of the ends of the tip to the total magnetization becomes smaller for longer tips. The switching field of this tip was also higher at 177 kA/m. From this we find that the switching field increases with decreasing cross–section of the wire. Similar behavior has been reported in literature [151, 150, 131].

In the simulations, a switching field of 32 kA/m was found for a tip with a 200×200 nm^2 cross section. The switching field, measured with the VSM, of the tips with a cross–section of 100×163 nm^2 and 100×118 nm^2 is 38.5 and 36 kA/m respectively. These values seem to be in good agreement with the simulations. The trend that the switching field increases with decreasing cross-section could also be seen in the VSM measurements of the tips with 57×103 nm^2 and a 57×54 nm^2 cross section. One has to note however, that the simulations use an idealized model of the real situation. The sample in the simulations had no anisotropy, perfectly smooth sides and the temperature was set at 0 K. As all imperfections cause a decrease of the nucleation field, it is very likely that the calculated values are too high. From the agreement between the simulations and the measurements, it can be concluded that the measured values of the switching field are rather high.

4.3 Integration of a magnetic tip

The deposition of the magnetic tip on the tip plane of the CantiClever probe is done with the same process that was used to fabricate the magnetic tips on the test structures. The only difference is the angle of evaporation. For the fabrication of the test structures an angle of 3° was necessary to obtain an array of tips. When depositing the magnetic tip on the tip plane, the direction of evaporation is chosen exactly perpendicular to the side edge of the tip plane. Again, cobalt was chosen as a material for the magnetic tip. The high saturation magnetization of cobalt will result in a high magnetic signal on the magnetic force microscope. Although iron and cobalt–iron have a higher saturation magnetization, we did not use them as a material for the magnetic tip because of their high sensitivity to corrosion. A SEM image of the tip plane after the cobalt is deposited is shown in figure 4.22. The tip plane of this probe has a thickness of 50 nm. The thickness of the cobalt layer is 30 nm. The side edge of the tip plane is covered by a continuous layer of cobalt without any discontinuities all the way down to the tip end. The close approximation to the ideal tip shape, a needle with a cross section in the nanometer range and several microns in length as discussed in chapter 2, could be realized. Due to the perpendicular direction of evaporation, only very little cobalt is deposited on top of the tip plane. The small isolated cobalt particles are separated from the magnetic needle on the side of the tip plane. It is expected that these particles do not have any influences on

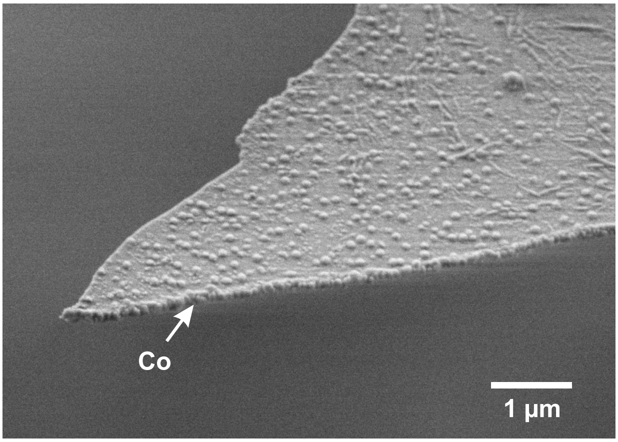

Figure 4.22: *Cobalt evaporated on the side edge of the tip plane. The arrow indicates the actual magnetic MFM tip.*

the behavior of the tip, as the end of the tip will be decisive for its performance in MFM measurements. We also expect these particles to be oxidized, or at most superparamagnetic, so that they will not contribute significantly to the magnetic signal.

One can distinguish that the tip consists of small, rounded grains that from a continuous layer along the complete side of the tip. It is very hard to see this in the figure, but this might very well result in a slightly rounded end of the magnetic tip. From the simulations, presented in section 2.3, it can be concluded that this is a desirable property, leading to a better resolution than originally estimated from the tip transfer curve of a tip with a flat tip–end.

4.4 Magnetic force microscopy using CantiClever MFM tips

To determine the maximum resolution that can be achieved with CantiClever MFM tip two types of samples were imaged. The first sample that we used is the CAMST-II reference sample [12]. The measurements on this sample are described in the first part of this section. The second sample is an experimental hard disk medium that contains written tracks with several bit lengths. The measurements on this sample are presented in the second part of this section. For all the measurements, the CantiClever probe was mounted in a Dimension 3100 MFM from Digital Instruments [140].

4.4.1 CAMST reference samples

The CAMST-II reference sample is a magnetic multilayer stack consisting of 20 bi–layers of 1.2 nm platinum and 1.2 nm cobalt–nickel on a 1.2 nm platinum seed layer. This multilayer stack has a strong perpendicular anisotropy. The sample that we imaged was AC-demagnetized.

The CantiClever probe that we used had a resonance frequency of 60 kHz and a 50 nm thick tip plane. The thickness of the cobalt tip was 50 nm. On the backside of the cantilever a 30 nm gold layer was deposited to improve the reflectivity.

The MFM was operated in lift–mode at a scan height of approximately 15 nm and a scan speed of 1 Hz. The resulting image is depicted in figure 4.23. The black and white regions represent areas with opposite perpendicular magnetization directions. This image was searched for the smallest magnetic details, carefully discriminating topography and measurement artifacts from magnetic features. The size of the magnetic details is measured by taking the distance between the two points where the signal is half of the maximum signal of the magnetic detail (full width at half maximum, FWHM). Using this procedure magnetic features as small as 30 nm could be distinguished, as can be seen in the line scan of figure 4.24. The sample was also imaged using a probe with a 37 nm tip plane. These measurements were comparable to the one shown here. The roughness of the sample prohibited a smaller tip to sample distance. Therefore, resolving magnetic features smaller than 30 nm became more a matter of speculation than measurement. Unfortunately, the extra resolution potential of probes with smaller magnetic tips can not be used anymore on this sample.

4.4.2 Perpendicular harddisk media

The second sample that we used to determine the performance of the CantiClever MFM probe is an experimental CoPtCr-SiO_2 perpendicular recording harddisk medium, developed by Fuji Electric Company and Tohoku University in Japan [152]. On the 3.5 inch disk, tracks with various recording densities are written using a single pole type head. The linear recording density ranges from 200 kFCI up to 1.1 MFCI. This corresponds to a bit length of 127 and 23 nm respectively.

For these measurements two different CantiClever probes, both with a resonance frequency of 65 kHz were used. The first probe featured a 50 nm thick tip plane, with a magnetic layer on the side that consists of 30 nm of cobalt, with a 20 nm thick layer of chromium on top. This layer has the same purpose as on the tips used to image the test samples in section 4.2.1: to protect the cobalt from oxidation, thereby enhancing the magnetic signal and the durability of the tip. The gold reflection layer at the back of the cantilever had the same thickness

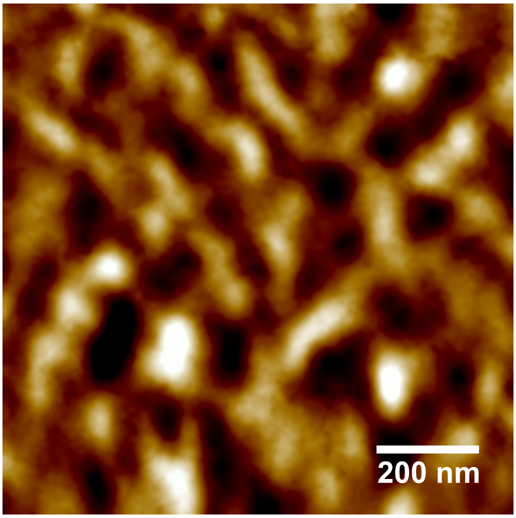

Figure 4.23: *MFM image of a demagnetized CAMST-II reference sample using the CantiClever MFM probe.*

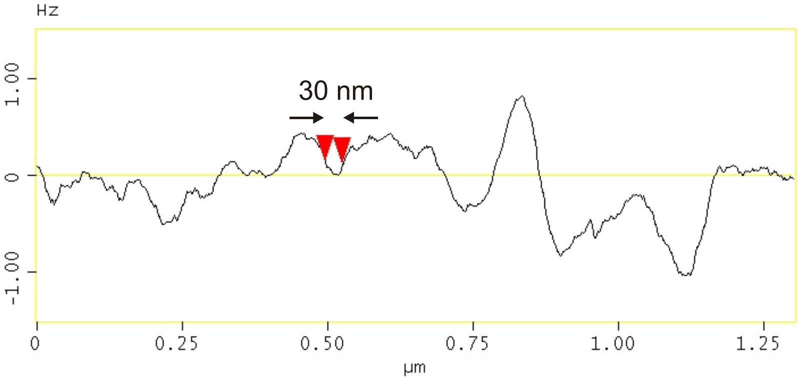

Figure 4.24: *Line scan taken from the MFM image of figure 4.23. A magnetic detail of 30 nm (FWHM) can clearly be distinguished.*

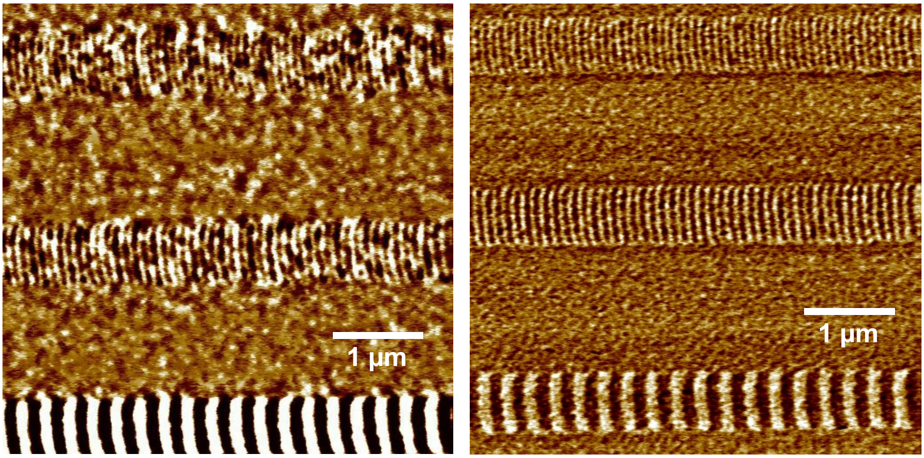

Figure 4.25: *MFM images of the hard disk medium showing the 200 (bottom), 500 (middle) and 600 kFCI (top) tracks, imaged using a probe with a 50 nm tip plane (left) and a 37 nm tip plane (right).*

as used before, 30 nm. The second probe had a 37 nm thick tip plane, with a 35 nm cobalt layer, covered by a 20 nm aluminum capping layer. Aluminium is preferable over chromium as a capping layer material, because it forms a closed layer at a smaller thickness. Moreover, when the aluminum oxidizes, a thin aluminumoxide layer is formed that prevents the layer stack from further oxidation [153]. For convenience, the reflection layer at the back of the cantilever consisted also of aluminum.

The MFM was again operated in lift–mode, with the scan height chosen such, that the tip just didn't touch the sample. The vibration amplitude was chosen lower in the MFM pass than in the AFM pass, to allow a smaller average tip to sample distance. Both parameters were adjusted such, that an image with an as high as possible resolution could be obtained while maintaining a decent signal to noise ratio and minimizing the topographical cross–talk in the image.

With the both probes, two regions of the sample were imaged that are depicted in figures 4.25 and 4.26. With the probe with a 50 nm tip plane, the bits in the written tracks can clearly be distinguished up to a recording density of 600 kFCI. The bit length at this recording density is 42 nm. Section analysis of the image from figure 4.25 showed a sharp peak in the spectrum at a wavelength of 89 nm, corresponding to a measured bit length of 45 nm. The bits in the 700 kFCI track of figure 4.26 are much harder to see, but can still be recognized. This track had the highest recording density at which we could still identify the bit transitions using the probe with a 50 nm tip plane. The spectrum of this track, shown in figure 4.27 shows a peak at a 77 nm wavelength, corresponding to a

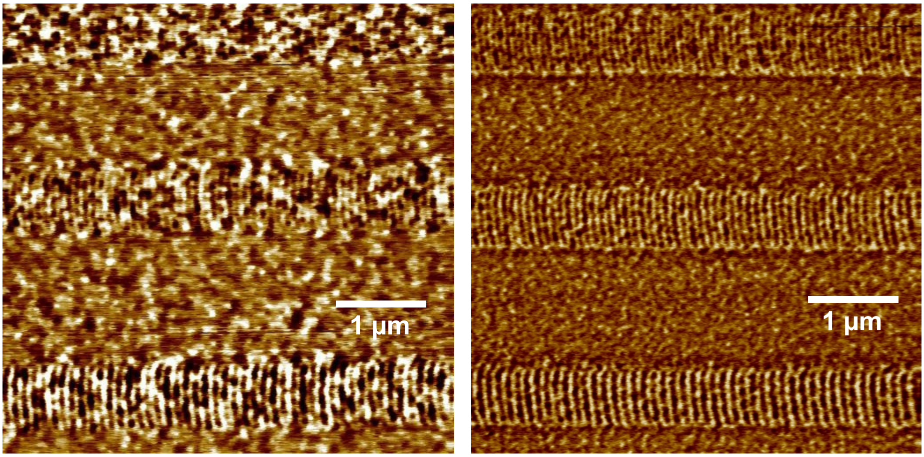

Figure 4.26: *MFM image of the hard disk medium showing the 500 (bottom), 600 (middle) and 700 kFCI (top) tracks, imaged using a probe with a 50 nm tip plane (left) and a 37 nm tip plane (right).*

measured bit length of 39 nm.

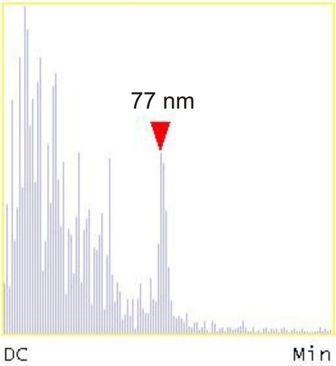

Figure 4.27: *Frequency spectrum taken from the 700 kFCI track of figure 4.26. The peak corresponding to the wavelength of the written track can be seen at 77 nm, corresponding to a measured bit length of 39 nm.*

As expected, the probe with a 37 nm tip plane enabled bits to be resolved in tracks with higher recording densities. With this probe, bit patterns could be imaged up to 1 MFCI, as shown in figure 4.28. The spectrum is shown in figure 4.29. A peak can be observed at 54 nm, resulting in a measured bit length of 27 nm. The slightly larger values for the measured bit lengths are probably due to a lower spinning speed of the medium during the writing of the tracks.

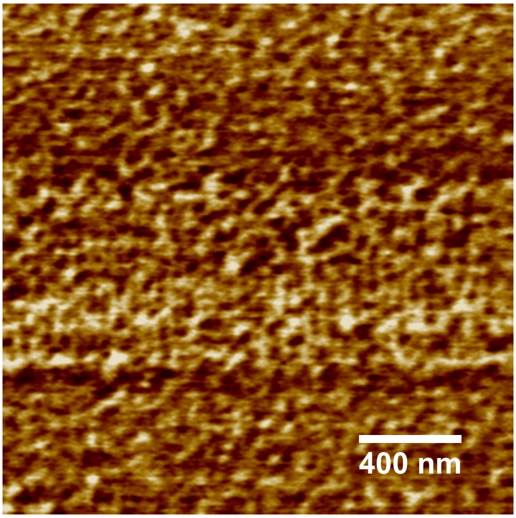

Figure 4.28: *MFM image of the 1 MFCI track on the hard disk medium.*

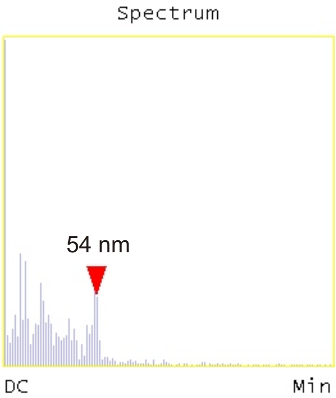

Figure 4.29: *Frequency spectrum taken from the 1 MFCI track of figure 4.28. The peak corresponding to the wavelength of the written track can be seen at 54 nm, corresponding to a measured bit length of 27 nm.*

MFM images like the ones presented in this section are used in the recording industry to study the recording process and determine the performance of the head and medium. A couple of observations can be made from the MFM images we obtained. First, for all but the largest bit patterns, the written bits are smaller than the intrinsic domain size. Second, the bits have a banana–like shape, caused by the geometry of the (single pole type) recording head. Third, one can see variations in the width of the tracks. This is probably a result of the DC erasure prior to the recording of the track. As this is a perpendicular medium, the thermal agitation is the most severe at large wavelengths. DC erasing almost corresponds to recording with very low recording density. However, it is unlikely that the magnetic clusters formed at track edge have a significant influence on the bits patterns, since the track width of the patterns is relatively large [154]. Finally, above 1 MFCI, no bit pattern could be observed anymore. This could be because our tip and/or microscope is not good enough to resolve the bits. Another possibility is that the bit patterns are not there anymore. If the 1 MFCI track was recorded very clearly with saturation recording, the bit patterns are probably very stable. However, the original patterns at the highest densities were not so clear, which indicates non–saturated recording due to a low field–gradient of recording head [154]. Although the medium should be very thermally stable at smaller wavelengths, badly written bit patterns could be erased by thermal agitation.

In conclusion, magnetic features that are smaller than the cross–section of the magnetic tip on the CantiClever probe could be distinguished on both the CAMST-II reference sample and the hard disk medium. Clearly, there seems to be no gap-zero effect. This is in agreement with the the simulations of the tip presented in section 2.3, that predict that smaller magnetic features than the tip cross–section can be resolved if the tip–end has an ellipsoidal rather than a flat shape.

4.5 Conclusion

The use of the CantiClever probe for MFM measurements has been discussed in this chapter, along with an analysis of the magnetic properties of the MFM tip.

Special test structures were designed to be able to measure the magnetic properties of the tip. On a 100 mm wafer, multiple arrays measuring 8×8 mm^2 containing approximately 160,000 silicon nitride islands were defined that closely resemble the tip plane on the CantiClever probe. Using a glancing angle evaporation method, magnetic tips with cross–sections down to 57×54 nm^2 were deposited on the sides of these planes. SEM images revealed that the tips consisted of small, densely packed columns of cobalt. The angle of evaporation proved to be a key factor that needs to be precisely controlled to successfully fabricate an array of tips.

Studies of the magnetic properties of the tips on the test structures using MFM showed that the tip consists of multiple magnetic domains in the as–deposited state. After an external magnetic field of 800 kA/m is applied parallel with the long axis of the tip, the domain configuration changes into a single domain state, as desired for MFM tips. When the same magnetic field is applied perpendicular to the long axis of the tip the single–domain configuration of the tip could be changed back into a two–domain configuration. This is consistent with other experiments described in literature.

When the magnetic tip is used for probe recording, the magnetic field required to switch the tip is a very important parameter. Therefore, the reversal behavior of the tips was studied by VSM measurements and micromagnetic simulations. The switching fields determined from VSM measurements ranged from 36 to 48 kA/m. This value is much lower than the coercive fields of typical media used in probe recording systems, so the CantiClever tip can be used for this application. Furthermore, the switching field increased with decreasing cross–section of the tip. The value of the switching field resulting from the simulations showed similar values as those determined from the measurements. Moreover, the simulations showed that the magnetization reversal of the tips takes place by nucleation of reversed magnetic domains at the edges of the tip, after which the magnetization reversal takes place by the displacement of the domain walls towards the center of the tip.

Integration of a magnetic tip on the CantiClever probe itself has been done using a similar evaporation process as used in the fabrication of the test structures. The only difference is the angle of evaporation; it was set to zero for evaporation on the probes. An SEM image of the tip plane after deposition showed a nicely defined tip, with only very little cobalt on top of the tip plane. The shape of the tip closely resembled the ideal tip shape.

To determine the maximum resolution that can be achieved with CantiClever MFM tip two types of samples were imaged: the CAMST-II reference sample and an experimental hard disk medium that contains written tracks with several bit lengths. The MFM we used is a Dimension 3100 MFM from Digital Instruments. On the CAMST-II samples, magnetic details as small as 30 nm could be observed, limited by the roughness of the sample. On the hard disk medium, which is much more flat, bit transitions could be identified up to 1 MFCI, corresponding to a bit length of 25 nm. The measured bit length on this track was slightly larger at 27 nm. In agreement with the the simulations of the tip shape, smaller magnetic features than the tip cross–section could be resolved due to the ellipsoidal shape of the tip–end.

Chapter 5

The integration of a magnetoresistive sensor

In this chapter, an investigation will be presented into integrating an active sensor element with electrical connections on the CantiClever probe. We have chosen for a magnetoresistive sensor as the active element for two reasons.

First, such a probe can be used in scanning magnetoresistance microscopy (SMRM) [155] [156]. Although the spatial resolution of this microscopy technique is less than that of MFM, it has several advantages. The signal is easier to quantify than that of MFM, the contact mode of operation makes it easier to implement and reduces the crosstalk of topography into the magnetic signal and finally the technique has relatively low costs. In the work of Yamamoto *et. al.* [155] and O'Barr *et. al.* [156], commercial MR heads were used as a probe. The resolution in this case is limited by the dimensions of the MR elements. To overcome this limitation, Phillips *et. al.* [157] used focussed ion beam (FIB) milling to reduce the size of the air–bearing surface of a yoke–type MR tape head. More recently, Nakamura *et. al.* developed a cantilever with an integrated MR sensor for SMRM that enables the simultaneous imaging of surface topography and magnetic stray field distribution [158, 159].

Second, the magnetoresistive CantiClever can be used as a probe in a prototype of a magnetic probe recording system. As described in chapter 1.2.2, one could either use a magnetic force probe or a magnetoresistive probe. In a recording mode based on MFM, the tip to medium distance must be controlled for each tip individually (varying when writing or constant when reading). This greatly increases the complexity of the total probe storage device. In a recording mode that uses MR–type probes, the tip is at a constant distance from the medium or even in contact with the medium. This would require only a very limited feedback control system to control the distance between the entire tip array and the medium, or none at all, thereby greatly simplifying the probe recording system.

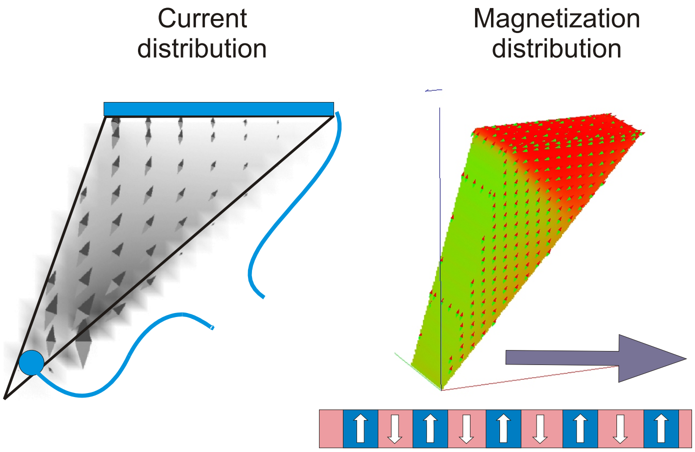

Figure 5.1: *Simulating the MR effect of a permalloy triangle. The left image shows the current distribution in the element and the contact leads (strip and dot). The right image shows the domain state of the element as it is scanned over the medium.*

Such an approach was chosen in the Millipede from IBM [21], where there is no individual tip to sample feedback for each probe.

The investigation starts with micromagnetic simulations of various shapes of the MR element and locations of the electrical contacts to determine the optimal shape and contact geometry. Then, the realization of such a sensor and the electrical contacts using a CantiClever probe is presented. Finally, the MR sensors were fabricated on a silicon wafer and characterized with MFM and Kerr microscopy.

5.1 Simulations of the MR effect

To study the MR response of a permalloy element integrated on the tip plane of the CantiClever probe, simulations were carried out by Klaus Ramstöck using his micromagnetic simulation package MagFEM3D [160]. To be able to simulate the MR effect of the permalloy elements, the package has been extended so that the current distribution inside the element could be calculated with a finite element method.

For all the simulations in this section, the following setup was used, depicted schematically in figure 5.1. All the elements consist of a 20 nm thick permalloy layer that has a specific resistance of 90 mΩcm. In the simulations, the element is scanned over a magnetic medium at a constant height of 5 nm. The magnetic

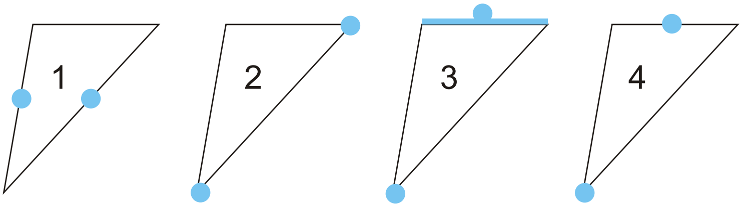

Figure 5.2: *The four different setups for contacts to the MR element that were simulated.*

medium is a 30 nm thick film having a saturation magnetization of 400 kA/m. In the medium, a bit pattern is written with a bit length of 480 nm in case of the triangle shaped elements and of 960 nm in case of the optimized shapes. The cell size of all the simulations presented throughout this section is smaller than $4 \times 2.5 \times 4\,\mathrm{nm}^3$.

5.1.1 MR response of a triangular tip

As a starting point, the shape of the permalloy element was chosen to be identical to the tip plane of the CantiClever probe as shown in figures 3.2 and 3.16. The outer dimensions of the simulated element were $600 \times 700\,\mathrm{nm}^2$. The magnetization pattern of the element was simulated as it scanned over the bit pattern. Subsequently, the current distribution in the element due to the contacts and the resulting MR response is calculated for four contact geometries, shown in figure 5.2. The results of the simulations for each setup when scanning over the medium is shown in figure 5.3.

From figure 5.3 it can be concluded that the highest signal could be obtained when one of the contacts is located at the ultimate tip end (geometry 2, 3 and 4). When the contacts are placed at both sides of the triangular element (geometry 1), the signal drops significantly, but this geometry has the advantage that it is much easier to realize. The maximum absolute MR response calculated for a triangular shaped element is only around $0.04\ \Omega$, with a resistance of the total element of $125\ \Omega$. From these simulations it can be concluded that a sharply pointed element is not a good choice. The triangular element consists of several large domains, which are pinned and therefore not influenced by the stray field of the sample. To improve the MR response, the shape of the element has to be optimized. These efforts are discussed in the next section.

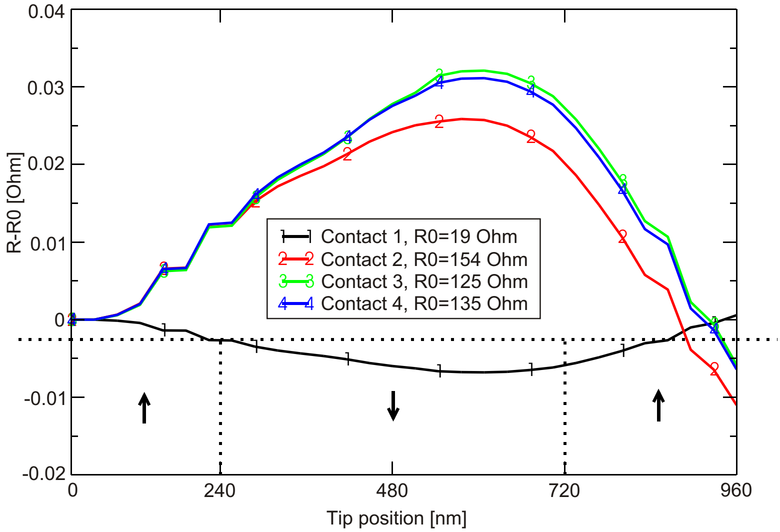

Figure 5.3: *MR response of the triangular shaped elements with the four contact geometries. The arrows and lines in the bottom part of the graph indicate the bit pattern and its magnetization direction.*

5.1.2 Optimization of the tip shape

Simulations of a triangular element indicated that only the part of the element closest to the medium is affected by the stray field from the medium. To get a higher MR signal from the element, the shape of the element has to be optimized in two ways. First, a larger part of the element must be close to the medium. As is the case with pole sizes in perpendicular recording heads, the tip radius must be adjusted to the desired resolution. In this case, the same size, or slightly larger than the bit length. Second, only the part of the current that flows through the region of the element affected by the medium stray field will contribute to the MR signal. Therefore, the current must be guided there.

The result of these optimizations is depicted in figure 5.4. The end of the element has been flattened to increase the “contact area”. A cut has been made in the middle part of the triangle to force the current to flow more closely to the bottom part of the element, as can be seen in figure 5.4. This 785×875 nm^2 shape results in a large increase in the MR signal, as depicted in figure 5.5. If the electrical connections to the element are positioned at the top of each “leg”, then the absolute MR signal increases to $0.18\ \Omega$ (labeled “optimized 3” in figure 5.5). Forcing the current to flow even more close to the tip end by making one of the connections close to the tip end further increases the absolute MR signal

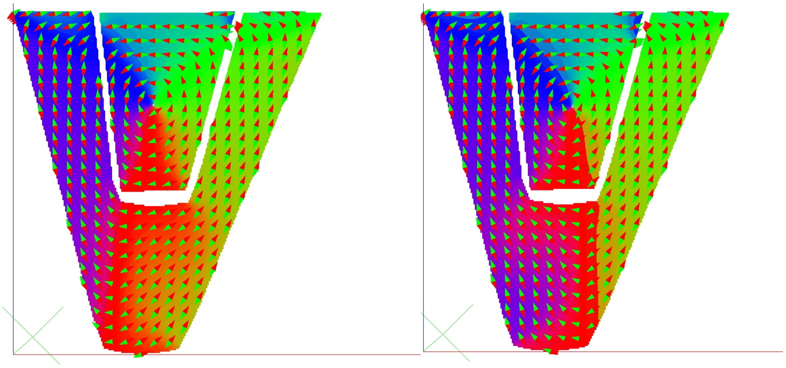

Figure 5.4: *MR element optimized to get a higher MR signal. The left image shows the magnetization distribution when going over a bit with magnetization pointing upwards, the right image when scanning over a bit magnetized downwards. The needles indicate direction of the magnetization.*

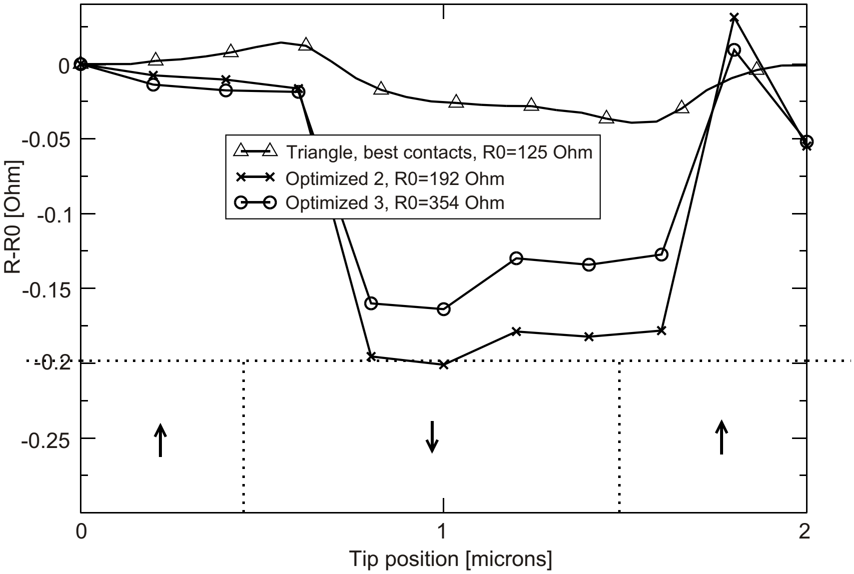

Figure 5.5: *MR response of the optimized elements and that of the best triangular element.*

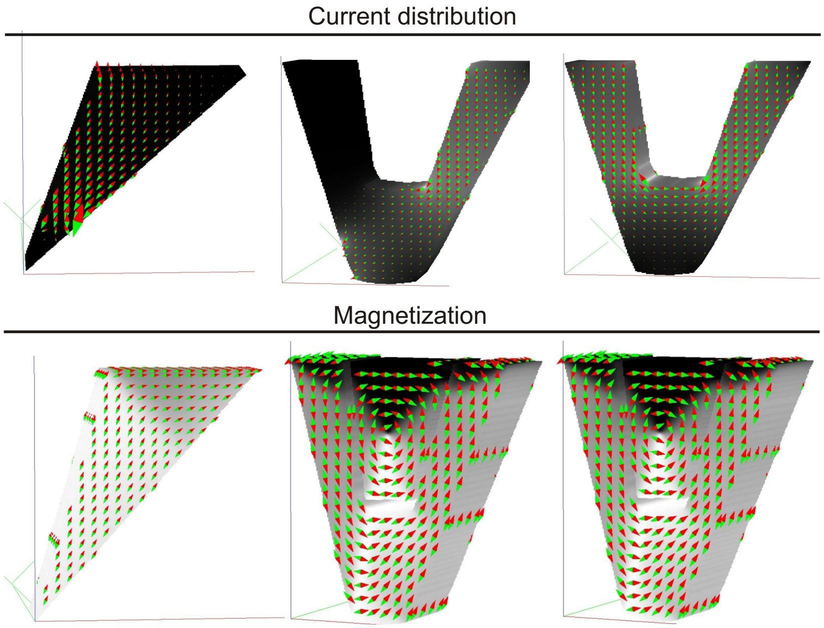

Figure 5.6: *Current distribution and magnetization of the three MR elements: triangle (left), optimized shape 2 connected at the top and at the tip (middle) and optimized shaped 3 with two connections at the top (right).*

to $0.24\ \Omega$ (curve labeled "optimized 2" in figure 5.5). It was found that the fields induced by the current flowing through the elements didn't influence the magnetization of the elements. The results of the simulations are summarized in table 5.1 and figure 5.6.

	AMR[1](%)	ΔR (Ω)	R0
Best triangle	˜0.01	0.04	125
Optimized 3	0.017	0.18	354
Optimized 2	0.041	0.24	192

Table 5.1: *Summary of the micromagnetic simulations.*

Two remarks must be made regarding figure 5.6. First, because there is no current flowing in this part of the element, the middle part of the optimized shapes was left out in the current distribution images. Second, because the only

---

[1] AMR is the percentage of the maximum MR response, taken to be 3% in the case of permalloy. The resistance of the elements is then calculated as: $R = R_0(1 + 0.03 \cdot \text{AMR})$.

difference between “optimized 2” and “optimized 3” is the position of the electrical contacts, the magnetization image of both optimized shapes is the same.

5.2 Realization of an MR sensor on the CantiClever

Due to time constraints, the development of an integrated fabrication process for making an MR sensor on a CantiClever probe was avoided by inventing a method to integrate an MR sensor on an already finished CantiClever probe. The method consists of two main parts: the deposition of the MR element on the tip plane and the fabrication of the electrical connections to the element. A schematic representation of how the finished probe should look like is shown in figure 5.7.

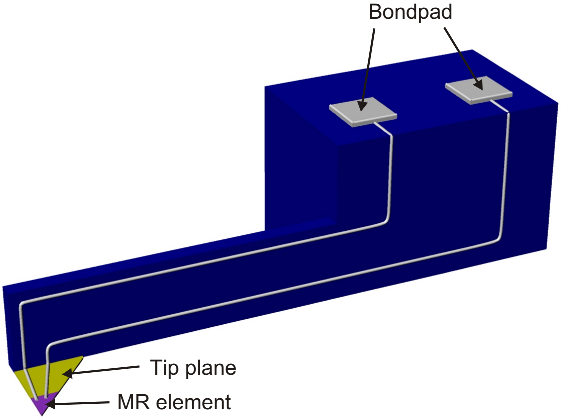

Figure 5.7: *Schematic picture of the CantiClever MR probe.*

5.2.1 Deposition of the MR element

The MR element had to be deposited on the tip plane of an already finished CantiClever probe. To be able to do so, one must be able to deposit the material that makes up the MR element only on the end of the tip plane. Shadow evaporation was chosen as the deposition method to accomplish this. The cantilever of the probe acts as the shadow mask, as shown in figure 5.8. Permalloy ($Ni_{82}Fe_{18}$) was chosen as the material for the MR element.

A special holder was built for this purpose, which is shown in the middle and right image of figure 5.8. The holder has a diameter equal to that of a 3 inch silicon wafer, to enable an easy fit in our MBE system. On the holder, 5 probe holders can be mounted, each offering space for six probes. Each of the

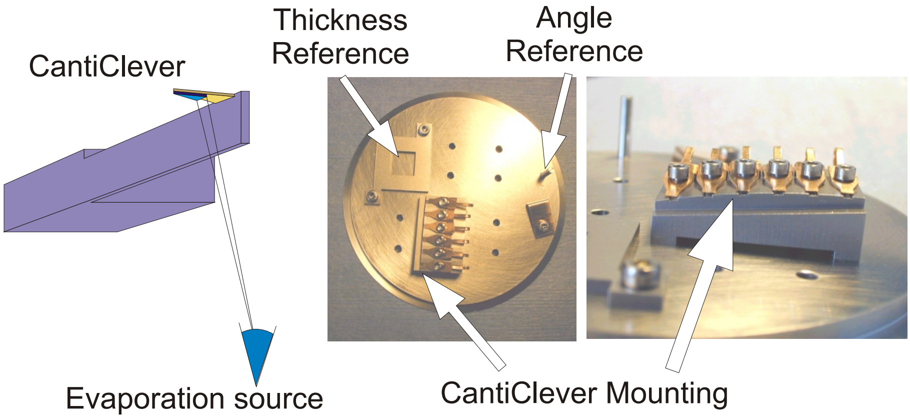

Figure 5.8: *Shadow evaporation of permalloy on the CantiClever probe. The left image shows the principle of using the cantilever of the probe as a shadow mask. The middle and right image show the holder designed for the evaporation. Only one of the possible five probe holders is mounted.*

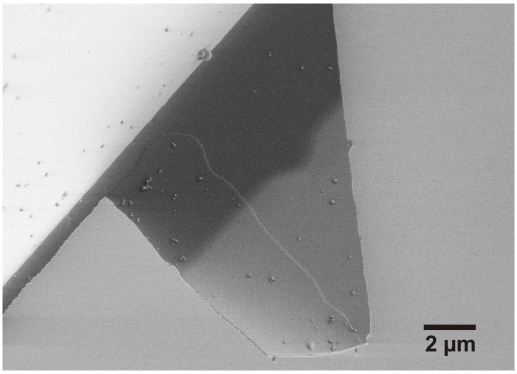

Figure 5.9: *SEM image showing the NiFe film (bright area) deposited by shadow evaporation on the backside of the tip plane.*

six probes is mounted under a different angle (ranging from 0° to 12.5°) to obtain different angles of evaporation. In this way, deviations in cantilever width can be compensated for and the shadow length can be varied. Besides for the probes, the holder also offers the space for two 1 cm^2 reference samples. With one sample the magnetic properties of the NiFe can be measured. With the other sample the deposition angle and direction can be checked by measuring the length and direction of the shadow from a small pillar.

A 20 nm thick NiFe film was evaporated onto the probes using the holder.

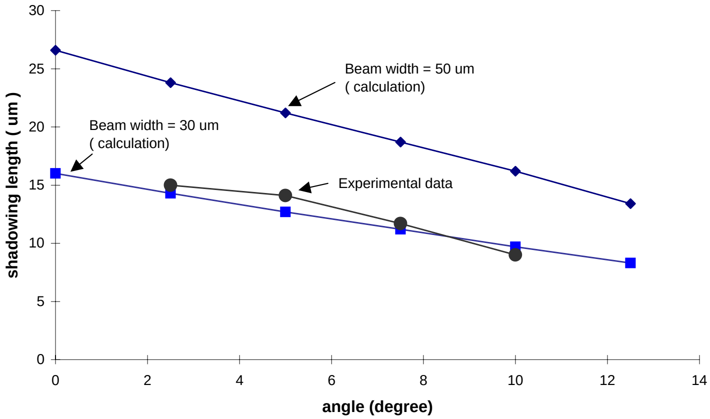

Figure 5.10: *Dependence of the shadow length on the evaporation angle during the shadow deposition of NiFe.*

An SEM image of the deposited film is shown in figure 5.9. The permalloy can be distinguished as the brighter area on the tip plane. The shadow evaporation technique succeeded in depositing a nicely defined, isolated NiFe element on the end of the tip plane. From SEM images, the length of the shadow for each evaporation angle was measured. These values were compared to the expected values from the geometry of the holder and measurement of the angle reference sample. The result is depicted in figure 5.10.

The measured shadow lengths are in good agreement with the calculated values for a 30 μm wide cantilever. The deviations from the calculated values are most certainly due to width variations of the cantilever. The probes used in this measurement were taken from a wafer where the width of the cantilever varied from 28 to 47 μm. The measurement shows that the holder for shadow evaporation works as desired.

5.2.2 Fabrication of the electrical contacts

The fabrication of wires to the NiFe element on the tip plane using standard thin film deposition methods and photolithography is not possible after the cantilever has been etched free from the substrate. To do this, another method had to be found. In this project, deposition of a metallic wire using an FIB system has been chosen as the method for fabricating the electrical connections to the MR sensor.

Ion beam induced deposition

Deposition of a metallic thin film in a FIB system is based on the principle of ion beam induced deposition (IBID), first demonstrated by Gamo *et. al.* in 1984 [161]. Material is deposited on the substrate surface when the ion beam (usually consisting of gallium ions) interacts with a layer of gas molecules, adsorbed on the surface. This so–called precursor gas consists of metal halide or organometallic molecules such as WF_6 to deposit tungsten [162] or $C_7H_7F_6O_2Au$ to deposit gold [163]. As a result, the molecules are disassociated into a volatile part that evaporates and a nonvolatile part that deposits on the surface [164]. This technique is used in a large number of applications such as repairing X-ray masks [165] and integrated circuits [166]. For the latter application, deposition of platinum from $(CH_3)_3CH_3C_5H_9Pt$ gas is used. The platinum does not contaminate the integrated circuit and is inert so it does not degrade when exposed to air or high current densities [167, 166]. Since this was the only material available at the time in our FIB system, we decided to use this as a material for fabricating the connections to the MR element.

Realization of the connections to the MR sensor

After the MR sensor has been deposited on the tip plane of the CantiClever probe, an insulating layer consisting of 70 nm of silicon oxide was applied using sputtering (to ensure good step coverage) before the contacts were made. This prevents not only damage to the NiFe element due to implantation of gallium ions during the FIB processes, but also shortcuts between the connections by leakage currents through the silicon cantilever.

The deposition of the electrical connections to the MR sensor was done in two separate FIB steps, because there is a 90° angle between the two parts of the probe on which the connections have to be made (i.e. the tip plane and the cantilever). The maximum tilt angle of our FIB system, a FEI FIB200, is only 45°. At these tilt angles, great care has to be be taken to avoid damage to the sample and the FIB system caused by contact between the gas nozzle for the precursor gas and the sample. In the first step, all the structures on the tip plane were made. After that, the sample was re–mounted, rotated 90° with respect to the first deposition step to deposit the structures on the cantilever.

First, the contacts to the MR sensor were made. To be able to make contact to the NiFe through the protection layer a staircase structure with small steps was milled trough the silicon oxide–NiFe–silicon nitride stack. One of the contacts to the MR sensor is shown in figure 5.11. The image was taken during the FIB process by using a low beam current. The NiFe can be clearly distinguished in the middle of the staircase by its different structure, and one can even observe a hole, where the FIB milled through the complete tip plane. The dimensions of

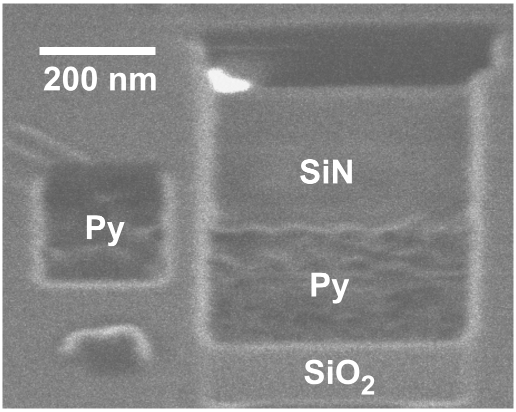

Figure 5.11: *One of the connections to the NiFe layer by FIB milling of a staircase.*

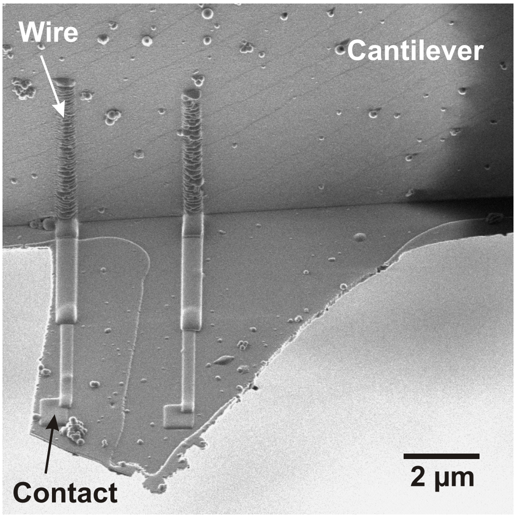

Figure 5.12: *The contacts to the MR sensor and the wires running over the tip plane to the cantilever.*

the staircase were $0.5 \times 1 \times 0.1\ \mu\mathrm{m}^3$ at a beam current of 11 pA. After this has been done, the whole staircase is filled with platinum, and the connecting wire to the cantilever is deposited on top. The first part of the wire has a cross–section of 300×200 nm^2, the second part 600×300 nm^2. The beam current in this case was also 11 pA. The contact holes filled with platinum and the wires on the tip plane are shown in figure 5.12. Note the part of the wire that runs from the tip plane onto the cantilever. To be able to deposit this wire, the stage of the FIB

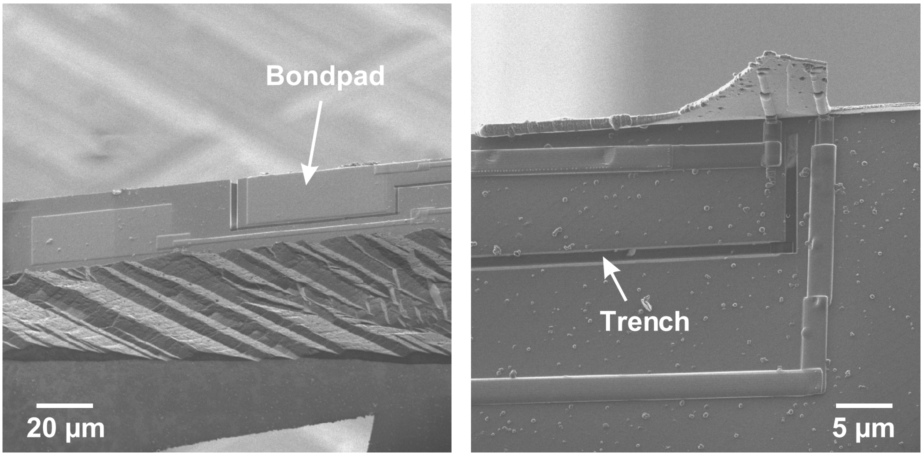

Figure 5.13: *The bondpads on the base of the probe (left image) and the wires on the tip plane and end of the cantilever (right image), deposited by FIB.*

system was tilted to 45°. The resulting wire consists of connected, ellipsoidal shaped islands. The same effect when depositing under an angle that departs from the normal to the surface is reported by Tao *et. al.* and may be due to a shadowing effect [167].

Subsequently, the wires on top of the cantilever and the bondpads were deposited. The wires have to run all the way from the tip to the base of the probe, in total around 250 microns. The cross–section was increased to $2 \times 1\ \mu\text{m}^2$ to improve the conductivity and larger beam currents up to 350 pA have been used to keep the deposition time within reasonable limits. The bondpads are $50 \times 20\ \mu\text{m}^2$ in size and were deposited at a beam current of 1 nA for 10 minutes. The results are depicted in figure 5.13. An FIB image of the complete MR probe is shown in figure 5.14. Note the trenches on both images of figure 5.13. These trenches were made using FIB milling to avoid a short circuit between the wires. If one looks at figures 5.12 and 5.13, there is a bright area around the deposited wires. This is also platinum, deposited during the FIB process. If the deposition time is short and the beam current is low (low ion dose), this layer is hardly conducting as the resistivity strongly increases at low ion doses [167]. With the thicker structures that were deposited, higher ion doses were used, so this layer might become a problem. To avoid this, a trench was milled along the complete cantilever to provide sufficient electrical isolation.

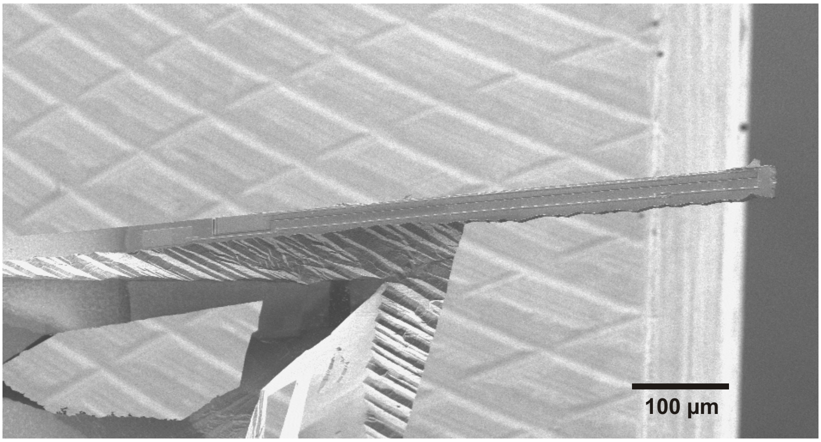

Figure 5.14: *The complete MR probe after the contacts and all the wires have been made using FIB techniques.*

5.2.3 Measuring the MR response

The resistance between the bondpads on the MR probe was measured using a probe station. The resistance of the structure was 12 kΩ. This value was consistent with estimations of the resistance of 13 kΩ using the specific resistance of the deposited platinum. The specific resistance was found by measurements on test samples to be 1930 $\mu\Omega$cm, or 19.3 Ω/square at a thickness of 1 μm. This value lies within the specifications of the FIB system we used that state a value between 10 and 20 Ω/square at a thickness of 1 μm [168]. This proved that electrical contacts to the MR sensor can be made using FIB deposition of platinum.

Unfortunately, no MR response could be measured when the sensor was placed in an external magnetic field. Measurements using the probe station equipment situated in the MESA$^+$ cleanroom failed because the equipment was not sensitive enough to detect the very small changes in resistance, with the high resistance of the FIB deposited connections. Attempts to use wire bonding to make contact to the bondpads were unsuccessful. This prevented measurements using a more sensitive measurement setup.

To find out whether the MR response can be measured if the wire bonding had been successful, one can calculate the signal to noise ratio (SNR) of the fabricated MR probe. If one assumes that the source of noise in the MR probe is dominated by thermal noise of the resistive contact leads then the expression for the rms noise voltage becomes [169, 170, 171]:

$$V_{noise,rms} = \sqrt{4kTR\Delta f} \tag{5.1}$$

Where k is the Boltzmann constant, T the absolute temperature, R the resistance and Δf the bandwidth of the measurement. Assuming a sinusoidal MR signal, the rms value of the MR response can be written as:

$$V_{signal,rms} = \frac{1}{2}\sqrt{2}(\frac{\Delta R}{R})IR \tag{5.2}$$

Where ΔR is the absolute change in resistance due to the MR effect, R the total resistance including the contacting platinum wires and I the current flowing through the sensor. The signal to noise ratio can then be obtained by combining both equations:

$$SNR_{dB} = 20\log\left[\frac{1}{2}\sqrt{2}\frac{(\frac{\Delta R}{R})IR}{\sqrt{4kTR\Delta f}}\right] = 20\log\left[\frac{I\Delta R}{\sqrt{8kTR\Delta f}}\right] \tag{5.3}$$

In the calculation of the SNR, we assume that the maximum current that can flow through the structure is limited by electromigration effects. For most metals, electromigration starts to occur at a current density of 10^9 to 10^{10} Am^{-2} [172]. For platinum a measured value of $3 \cdot 10^{11}$ Am^{-2} could be found in literature, but only during short current pulses [173]. Therefore, in the calculations below, the value of 10^9 Am^{-2} will be used. The smallest platinum wire present on the structure has a cross section of $60 \cdot 10^{-14}$ m^2, so the maximum current that can be put through the MR sensor is 60 μA. The absolute resistance change due to the MR signal in a triangular element determined from simulations is 50 mΩ (see section 5.1.1), while the resistance of the complete structure is 12 kΩ. Furthermore, we assume that the measurement will be done at room temperature (300 K) in a 1 Hz bandwidth. Filling all these values into equation 5.3 results in a signal to noise ratio of 44 dB.

Although this value indicates that measurement of the MR signal on the fabricated probe should be possible if contacts to the bondpads can be made properly using wire bonding and a sensitive measurement setup is used, there are a few practical problems that may very well prohibit a successful measurement. In the calculation given above, the high resistance of the wires and contact resistance of the wirebonds are assumed to be constant. It is very likely that this will not be the case in a real measurement. The resistance of the FIB deposited wires will vary due to heating because of the current and changes in ambient temperature. The contact resistance of the wirebonds will vary during the measurement because of the current and mechanical reasons. This could very easy be larger than the MR signal.

One could think of several solutions (or a combination thereof) to solve the problem. First of all, the use of a more advanced measurement setup that uses a four–point measurement instead of a two–point measurement to measure the resistance. This however implies that twice the amount of FIB processing has to be done, which is quite time consuming. The FIB deposition of the two connections is already stretching the capabilities of the FIB system. Second, one could shift the measurement band to a higher frequency by modulation of the signals. This could be realized with a lock–in amplifier. Third, one could try to lower the resistance of the wires to the MR sensor. For this, there are several possibilities. The first is to decrease the length of the wires by fabricating the MR sensor onto a CantiClever probe with a shorter cantilever. These are readily available, so this could be done with relative ease. The second possibility is to reduce the resistance by optimizing the FIB deposition process of platinum or to use gold for FIB deposition. For platinum deposited by FIB specific resistances down to 70 $\mu\Omega$cm are reported in literature [167], which is much lower compared to the 1930 $\mu\Omega$cm we measured. Even better results were obtained by deposition of gold, where a value of 7 $\mu\Omega$cm could be achieved, very near to that of pure gold (2.44 $\mu\Omega$cm) [174]. In conclusion, the use of a lock–in amplifier and two connections, with much lower resistance, to the MR sensor seems to be the most promising way to be able to measure any MR response from these kind of prototype MR probes.

5.3 Magnetoresistive sensors on a wafer scale

As described earlier in this chapter, no magnetic response could be measured from the MR sensor fabricated on the tip plane of the CantiClever probe. To verify the results of the simulations, to be able to measure the response of an MR sensor that can be integrated on the probe and to reduce the turn-around time in sensor optimization, the MR elements were fabricated on a silicon substrate with electrodes [175].

5.3.1 Design and fabrication

On a 100 mm wafer, 5×5 mm^2 square chips have been defined. Along the sides of these squares, the elements are situated for MR measurements. In this way, the required bondpads can be placed at the edges of each square for easy wirebonding. Most of these elements have 4 contacting wires to enable a four–point resistance measurement. On some of these squares, the area in the middle of the chip is filled with an array of elements to enable other measurements like MFM and Kerr microscopy. The principle layout is depicted in figure 5.15.

There are three different type of elements present on the wafer. The first type of element has the same shape as the MR element that was made on the probe, as described in section 5.2. The dimensions are chosen the same as those of the tip plane. The second type of element have the basic shape of the elements that were tuned for higher MR response using the micromagnetic simulations (see figure 5.4). The third group of elements are simple rectangles. As the smallest dimensions of the elements are restricted by the lithographic line of the MESA$^+$ cleanroom to 2 μm, these can be structured by FIB milling into any

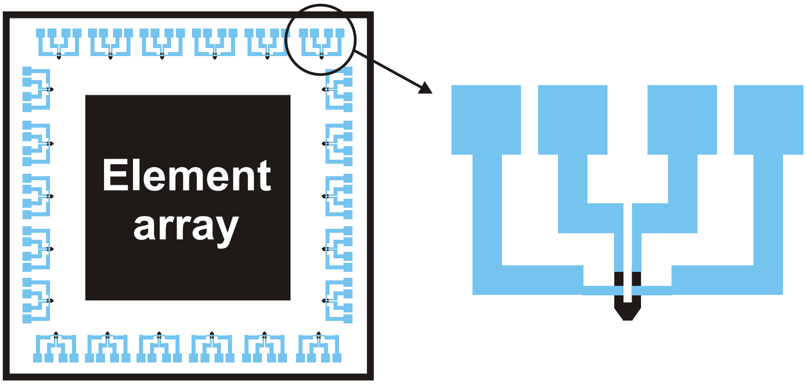

__Figure 5.15:__ Principle layout of the mask for the MR elements showing one of the 5×5 mm^2 square chips (left) and an individual element with its four contacts (right).

desired shape.

The fabrication process for the MR elements requires two masks: one to define the permalloy elements, and one to define the electrical connections. An overview of the fabrication process is as follows:

- The structures are made on a standard 100 mm $\langle 100 \rangle$ wafer. The wafer is first oxidized in a wet oxidation process to create a 500 nm thick silicon dioxide layer. This layer provides the insulating substrate needed for the structures on top.
- The permalloy elements are defined using a lift off process. The permalloy layer is deposited using sputtering on top of the photoresist patterns, made with the use of the first mask. After the deposition, the unwanted parts of the permalloy layer are then removed by dissolving of the photoresist, leaving the permalloy elements behind. The thickness of the permalloy was 70 nm.
- The electrodes and bondpads are defined in a similar lift– off process. The electrodes are made out of a 500 nm thick layer of aluminum, deposited using e–beam evaporation. The second mask is used in this step, aligned to alignment marks defined in the previous step.

5.3.2 Results

Two of the finished elements are depicted in figure 5.16. The left one shows a element that has the shape of the tip plane of the CantiClever. The two con-

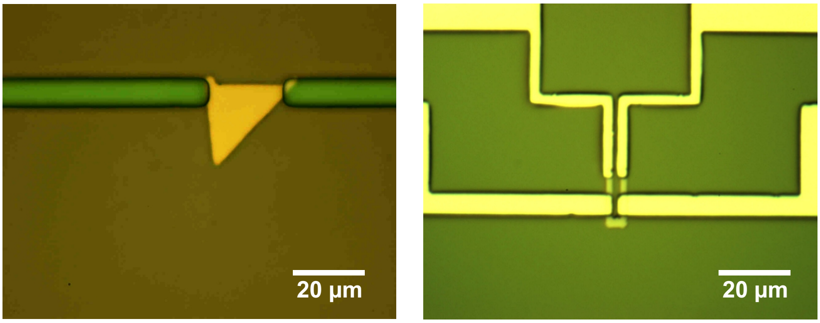

Figure 5.16: *Two types of lithographically defined permalloy elements. The triangle element shaped like the CantiClever tip plane (left image) and the U–shape as determined from simulations (right image).*

nections made here are corresponding to the configuration that gave the highest MR response in the micromagnetic simulations: one at the top of the triangle (left electrode) and one at the end of the 'tip' (right electrode). The right image shows one of the elements shaped similar to the optimized structures from the simulations, except for the part in the middle that is present on the simulated structures, but couldn't be fabricated using lithography. These elements have four electrodes to enable a four–point resistance measurement.

Rectangle elements were included on the wafer to be modified by FIB milling. One of the elements that has been shaped using FIB milling is depicted in figure 5.17. The dark recessed areas in the middle of the image are the parts of the structure that have been milled away. The remaining element itself is visible as the bright U–shape in the middle of the image, with the two aluminum electrodes on each side.

5.4 Magnetic characterization

The (not FIB etched) U–shaped permalloy elements described in the previous section were analyzed with three measurement methods. The remanent magnetization state was studied using MFM, and the switching behavior with in–plane Kerr microscopy and MR measurements.

5.4.1 Domain imaging using MFM

The domain state of the element in zero magnetic field was imaged with the MFM in two different conditions. The elements were saturated with a magnetic field oriented parallel to the "legs" of the element and perpendicular to the legs

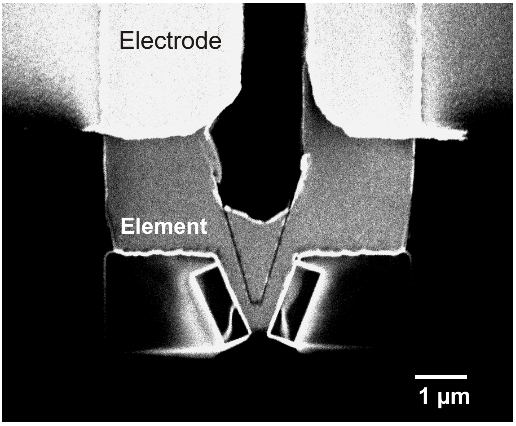

Figure 5.17: *Permalloy element modified with FIB milling to resemble the optimized shape determined from the simulations.*

of the element. The MFM and the tips that were used are the same as those described in section 4.2.1. The result is shown in figure 5.18.

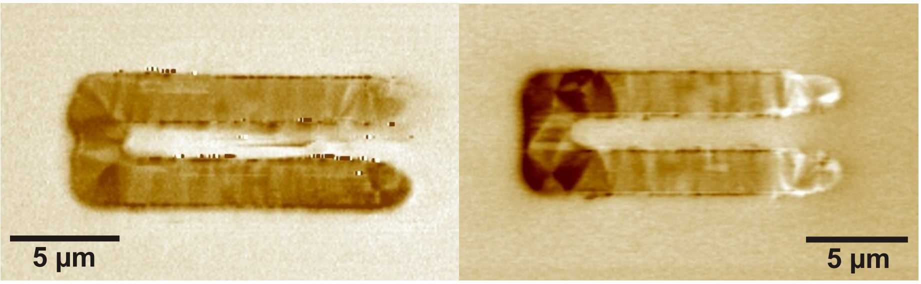

Figure 5.18: *MFM images of the permalloy images, showing the remanent domain structure after saturation in a magnetic field perpendicular to the legs (left) and parallel to the legs (right).*

Both elements show a complicated domain structure at the sensing part of the element (i.e. the connection between the legs), regardless of the orientation of the magnetic field that was used to saturate them before the measurement. This is not a desirable situation if the sensor is used for reading in a probe recording system, as it is a major source of noise. It can be concluded that biasing of the element will be necessary to be able to use the sensor for reading. However, the test sensors used here are relatively large. As the dimensions decrease, the number of domains will decrease as well. For small elements no domain walls fit inside the structure anymore, as can be seen in the micromagnetic simulations of figure 5.6.

5.4.2 Kerr microscopy measurements

The switching behavior of the elements in an external field could be imaged on our home–built Kerr microscope. This microscope is capable of measuring the longitudinal and polar Kerr effect and is equipped with an electromagnet to enable measurements of samples in an external field [176]. The following measurement procedure was used to measure the MR elements. First, the element was saturated with a magnetic field of 1000 Oe (80 kA/m) parallel with the legs of the element. Subsequently the field was reduced to zero, taking the background image (for substraction of the topographic information) at 100 Oe. After that, the field was increased in the opposite direction and a series of images was taken, that captured the switching of the element. The results are displayed in figure 5.19.

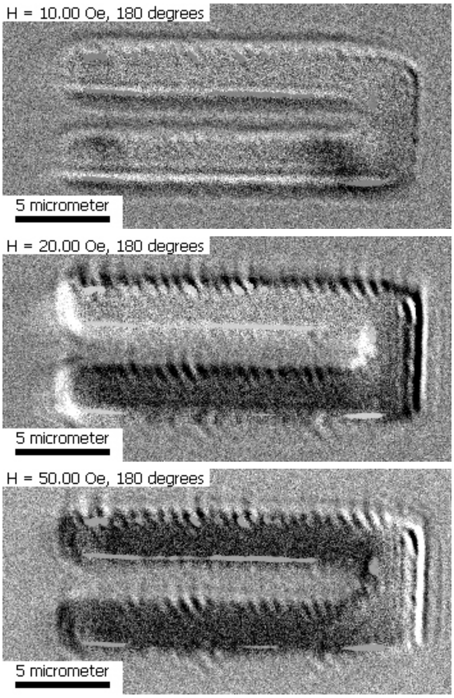

Figure 5.19: *Longitudinal Kerr microscopy images showing the switching of the element. The saturated state is displayed on top, followed by switching of the first leg (middle) and the second leg (bottom).*

From these images, the switching of the legs can clearly be seen. The lower leg switches at 20 Oe and the upper at 50 Oe. The magnitude of the magnetic field is however not very precise, as the field was not measured during the measurements and a relatively large electro-magnet was used, that exhibits a remanent magnetization that is in the same order of magnitude as the small field values at which the legs switch.

What happens at the sensing part of the element cannot be distinguished from the images. The fringes present at the edges of the element that prevent this are caused by the substraction of the topographic image. For application as a read sensor in a probe recording system, switching of the legs is probably not of great influence on the response of the sensor, as the stray field from the medium is only present very close to the medium surface. If the same sensor is used for writing however, it is important that the legs return in the anti-parallel position after the external field is removed, to avoid unwanted domain walls in the sensing part of the element.

5.4.3 MR measurements

The MR response curves of the elements to an external applied field were also measured. The magnetoresistance was measured using a Stanford Research SR830 DSP lock-in amplifier with a computer interface. The MR response proved to be 0.27% when the field was applied parallel to the legs of the element, as shown in figure 5.20. When the field was applied perpendicular to the legs, the MR response was 0.63%.

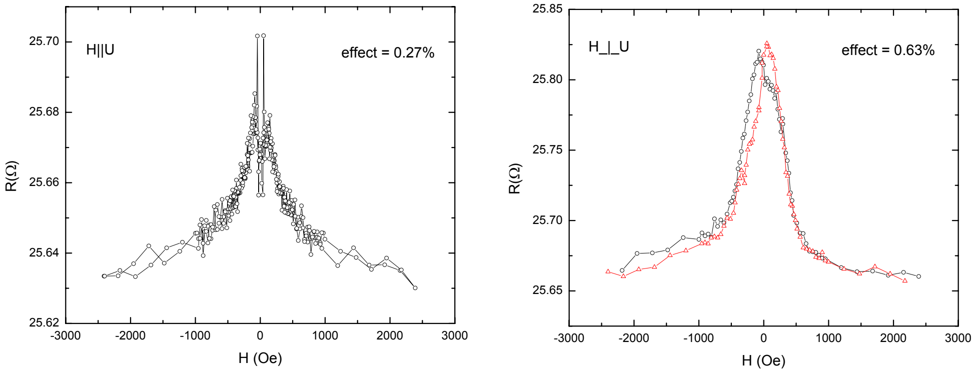

Figure 5.20: *MR response curve of the element with the field applied parallel to the legs (left) and perpendicular to the legs (right).*

The spikes that are visible in the left image of figure 5.20 might be due to the switching of the legs, as observed in the Kerr microscopy images. The spikes occur at small values of the magnetic field, centered around zero, which is different from the field values obtained from the Kerr images. This difference might be explained by the remanent field (and hysteresis) of the magnet in the Kerr microscope. Further investigations are necessary however to give a solid explanation for the spikes in the MR response.

5.5 Conclusion

An investigation of the possibilities of the CantiClever probe for the integration of another sensor besides an MFM tip has been presented in this chapter. A magnetoresistive element together with the electrical connections was chosen as the sensor because the resulting probe could be used for SMRM and serve as a prototype of a probe that can be used in future probe recording systems.

The absolute MR response of such a sensor was simulated using a micromagnetic simulation package expanded to also calculate current densities. A sensor with the same shape as the CantiClever tip plane was simulated first, determining the optimum location of the connections to the sensor. The MR response proved to be the highest if one of the wires was connected at the ultimate tip end. However, the absolute MR response calculated for this geometry proved only to be about $0.04\ \Omega$. From these simulations could be concluded that a very pointed tip is not a good choice because only the part of the element closest to the medium is affected by the stray field from the medium. The shape of the sensor was optimized by adjusting the tip radius to the desired resolution and focussing the current as close as possible to the tip end. These designs resulted into a higher absolute MR response, with the best geometry having an MR response of $0.24\ \Omega$.

To avoid the development of an integrated fabrication process for making an MR sensor on a CantiClever probe, a method was invented to integrate an MR sensor on an already finished CantiClever probe. The MR element was realized on the back of the tip plane by means of shadow evaporation of permalloy, using the cantilever of the probe as a mask. In this way, a 20 nm thick isolated magnetic element could be deposited at the end of the tip plane. The electrical connections to the element were made using the deposition of platinum in an FIB system. To avoid leakage currents through the silicon cantilever and to protect the permalloy elements from the ion radiation of the FIB, a layer of silicon oxide was sputtered on top of the permalloy element and the cantilever. On top of this layer, the wires and bondpads were successfully deposited and contact to the sensor could be established. The resistance of the total structure was measured using a probe station to be 12 kΩ. This value was consistent with estimations of the resistance using the specific resistance of the deposited platinum, measured to be 1930 $\mu\Omega$cm.

Unfortunately, no MR response could be measured when the sensor was placed in an external magnetic field. The probe station equipment used was not sensitive enough to detect the very small changes in resistance. Attempts to use wire bonding to make contact to the bondpads were unsuccessful, preventing measurements using a more sensitive measurement setup. Assuming that the resistance of the connections to the sensor is constant, a reasonable SNR of 44 dB was calculated. In practice however, the resistance of the connections will vary due to a number of effects, making it impossible to measure the small resistance changes. A solution to this problem could be to use a lock–in amplifier and two low resistance connections to the MR sensor to measure any MR response from these kind of prototype MR probes. Lower resistance connections can be achieved by using shorter wires, optimization of the FIB deposition process or the use of other materials like gold.

To be able to measure to response of the MR sensor, a large number of sensors were made on a silicon wafer and connected with aluminum wires and bondpads. Three different types of sensors were fabricated this way: triangular shaped sensors, sensors that resemble the optimized shape (U–shaped) obtained from the simulations and rectangular sensors to be shaped by FIB milling. The magnetic characterization using MFM, Kerr microscopy and MR measurements were done on the U–shaped sensors. The elements showed a complicated domain structure at the sensing part if there was no magnetic field applied. For use as a read sensor, the biasing of the element is required. The Kerr measurement showed very nicely the switching of the legs of the element. An MR response of 0.27% could be obtained if the field was oriented parallel with the legs and 0.63% if the field was oriented perpendicular to the legs.

Chapter 6

Conclusions and recommendations

6.1 Design of the CantiClever probe

In this work, a novel fabrication method for probes for scanning probe microscopy has been developed, called the CantiClever process. The novel probe made in this process deviates from existing probe designs for magnetic imaging in two ways.

First, the tip of the probe consists of a lithographically defined thin film instead of a silicon pyramid with fixed dimensions defined by the crystallographic orientation of the wafer used. This so called tip plane not only serves as a support for the magnetic needles needed in probes for magnetic force microscopy, but, because of the planar fabrication process, allows the integration of other (active) sensing elements.

Second, the silicon cantilever of the probe is fabricated tilted 90 degrees with respect to the wafer plane in comparison with conventional silicon cantilevers. This enables the two key parameters that control the resonance frequency of the cantilever, its length and thickness, to be precisely controlled by photolithography. This allows cantilevers with a wide range of resonance frequencies to be made out of a single silicon wafer or a large number of cantilevers having exactly the same mechanical properties.

The design of the probe was implemented with the use of a parameter based software package. Here, the structures are programmed instead of drawn. Key parameters can be specified and the structures are generated accordingly. In case of the CantiClever, the resonance frequency must be specified and a cantilever having the corresponding dimensions is generated. The resulting design can be easily re–used or modified and the resulting implementation has a very high accuracy.

The cantilever and base of the probe are fabricated from $\langle 110 \rangle$ silicon wafers using a two step KOH wet anisotropic etching process. In the first step windows are etched from the backside of the wafer to determine the final cantilever width. In the second step the cantilevers and tip planes are etched free. The KOH etching creates very flat surfaces, exactly perpendicular to the wafer surface, which are excellent for interferometric deflection detection.

The demands on the material for defining the tip planes are threefold: the material must be stiff in order to prevent bending during scanning with the tip, the material must have very low stress to obtain a free hanging structure over a large range that does not bend and finally the material must be able to withstand the KOH etching process. Silicon nitride deposited in a low stress LPCVD process proved to match all those criteria. As described in chapter 2, a very sharp cut-off corner of the tip plane is needed to obtain high resolution tips for MFM. By means of reactive ion etching using a Cr mask layer to remove the rounded end of the tip plane, a radius of curvature as small as 30 nm could be achieved using a 2 micron lithography process. With the procedure described above, tip planes as thin as 37 nm were successfully fabricated.

The probes were fabricated on 100 mm wafers, each wafer containing 220 probes. The probes were designed to have resonance frequencies, as calculated from the formula given in chapter 3, from 60 to 1000 kHz. The measured resonance frequency was always slightly lower. This is due to the fact the the thickness of the cantilevers was smaller than designed, despite the highly anisotropic etching process used for etching of the cantilevers. The quality factor of the cantilevers was also measured. At atmospheric pressures, the value of Q was around 600 for a 67 kHz cantilever. When the same probe was used in vacuum conditions, the Q–factor increased to around 50000.

The base of the probe was designed in such a way that the cantilever was situated at exactly the same location as that of a conventional probe. This ensures maximum compatibility with existing microscopes and avoids problems with the focussing of the laser of the beam deflection detection system of the microscope. With the CantiClever measurements were successfully carried out on various commercial microscopes, including those of Digital Instruments.

6.2 Using the CantiClever for magnetic force microscopy

As discussed in chapter 2, it appears that at the moment the resolution of MFM is limited by the geometry of the magnetic tip. The dimensions as well as the shape of the magnetic tip have a big influence on the resolution. Conventional AFM based probes have a pyramidal shape that strongly deviates from the ideal tip shape, being that of an elongated bar. The elongated shape induces a strong shape anisotropy, which increases the stability of the magnetic tip against remagnetization by the sample. Also, a long magnetic element behaves as a monopole when imaging small magnetic features, which increases the signal output.

The shape of the tip–end has a great influence on the achievable resolution. Therefore simulations were carried out to investigate this. Three different shapes of the tip–end were considered: a triangular, an ellipsoidal and a flat shape. The transfer functions of the three different tip shapes were calculated. The resolution that could be achieved was then estimated by comparison of the tip transfer function and the noise level due to thermal noise of the cantilever at room temperature. The triangular tip, resembling the shape of conventional sharp pointed MFM tips, proved to be less sensitive than the ellipsoidal and flat tips because a large proportion of their magnetic charges is located at a greater distance from the sample. The flat tip showed the highest sensitivity of the three tips, but suffers from the presence of gap zeros in its transfer function. This makes the ellipsoidal shaped tip the best candidate for high resolution MFM. Only at very high wavelengths, around 5 nm, the flat tip has an advantage over the ellipsoidal tip.

With the CantiClever process, such an MFM tip having a nearly perfect shape could be realized by deposition of magnetic material on the side of the tip plane. This defined both lateral dimensions of the tip by thin film deposition techniques, allowing for control in the nanometer regime, while the length of the tip is defined using photolithography allowing for lengths of several microns.

Studies of the magnetic properties of the tips using MFM show that the tip consists of multiple magnetic domains in the non magnetized state. After an external magnetic field of 800 kA/m is applied parallel with the long axis of the tip, the domain configuration changes into the desired single domain state. Applying the same external field perpendicular to the long axis of the tip causes a two-domain configuration with a domain wall in the center of the tip. This behavior is consistent with measurements described in literature.

The resolution that could be achieved with the CantiClever MFM tip was determined by measurements on two types of samples, using a commercial DI3100 microscope in air at room temperature. The first sample was a demagnetized CAMST-II reference sample, that has been used in the past for testing the resolution of various magnetic force microscopes. Magnetic features as small as 30 nm could be distinguished when a CantiClever having a 50 nm tip plane, coated with 50 nm of cobalt. The cantilever of the probe had a 60 kHz resonance frequency. Unfortunately, the extra resolution potential of probes with smaller magnetic tips could not be used on this sample, due to the roughness of the sample, that prohibited a smaller tip to sample distance. The second sample was an experimental CoPtCr-SiO_2 perpendicular recording harddisk medium, containing written tracks with linear densities up to 1.1 MFCI. The bit patterns could be imaged up to a density of 1 MFCI, using a CantiClever probe with a 37 nm tip plane coated with 35 nm of cobalt and a 20 nm aluminum capping layer. The measured bit length was slightly larger at 27 nm. On both samples, magnetic features that are smaller than the cross–section of the magnetic tip on the CantiClever probe could be distinguished. Clearly, there seems to be no gap-zero effect. As the tip consists of small, rounded grains that form a continuous layer along the complete side of the tip, the end of the tip might very well be slightly rounded, resembling the ellipsoidal tip shape of the simulations. The simulations predicted that smaller magnetic features than the tip cross–section can be resolved if the tip–end has an ellipsoidal rather than a flat shape.

Besides the work going on within the SMI research group in the field of probe microscopy, research is also carried out in another field where magnetic probes can be applied, that of magnetic probe recording. In cooperation with other groups, a system called μSPAM, short for micro Scanning Probe Array Memory, is under development that uses an array of magnetic probes to read and write data in parallel on a patterned magnetic medium, consisting of single domain magnetic dots. To read and write bits in such a system, there are two modes for reading and writing: MFM and MRM, as described in section 1.2.2. When a magnetic tip is used for (MFM mode) probe recording, the magnetic field required to switch the tip is a very important parameter. On special fabricated samples containing around 10^5 tips the reversal behavior was studied for tips with various cross-sections ranging from 100×163 nm^2 down to 57×54 nm^2 using VSM measurements. From these results and micromagnetic simulations could be concluded that the magnetization reversal of the tips takes place by nucleation of reversed magnetic domains at the edges of the tip, after which the magnetization reversal takes place by the displacement of the domain walls towards the center of the tip. Switching fields have been measured between 36 and 48 kA/m. This value proved to be lower than the coercive fields of typical media used for probe recording. This leads to the conclusion that the CantiClever tip can be used for this application. The results further showed that the switching field increased with decreasing tip cross–section, as expected from the simulations.

6.3 The integration of a magnetoresistive sensor

The use of a lithographically defined tip plane enables the realization of MFM tips that are suitable for high resolution MFM. Apart from that, the tip plane has another advantage over the pyramid–shaped tips of conventional probes, that are defined by crystal planes. Because the tip plane is oriented parallel to the substrate surface, similar planar fabrication processes can be used to define other structures on the tip plane and the rest of the probe. This could enable the integration of other sensors besides an MFM tip on the CantiClever probe.

In this work, a prototype of a single probe that could be used for SMRM and in preliminary probe recording experiments was developed by integrating a magnetoresistive sensor and wiring onto a CantiClever probe.

To avoid the development of an integrated fabrication process for making an MR sensor on a CantiClever probe, a method was invented to integrate an MR sensor on an already finished CantiClever probe. The MR element was realized on the back of the tip plane by means of evaporation of permalloy. The magnetic material must only be deposited at the end of the tip plane and not on the whole probe. This could be achieved by shadow evaporation, using the cantilever of the probe as a shadow mask. To realize such a structure with great accuracy, a special holder was designed that can hold up to 6 probes at various angles, to control the length of the deposited element and compensate for variations in the width of the cantilever. The holder also offers space for test samples to check the angle of deposition and measure the magnetic properties of the deposited permalloy. Using this holder, 20 nm thick isolated magnetic elements could be deposited at the end of the tip plane.

To measure any change in resistance of the element, electrical connections to the element must be made. For this prototype, these connections were made using the deposition of platinum in a focussed ion beam system (FIB). Such a system, mostly used for modifying and repairing integrated circuits, can locally deposit a conducting layer by decomposition of a metallic gas using ion beam radiation. To protect the permalloy elements from the ion radiation of the FIB and avoid leakage current through the silicon substrate, a layer of silicon oxide was sputtered on top of the permalloy element and the cantilever. On top of this layer, the wires and bondpads were successfully deposited and contact through the protection layer to the permalloy was established. The resistance of the total structure was measured using a probe station to be 12 kΩ. This value was consistent with estimations of the resistance using the specific resistance of the deposited platinum, measured to be 1930 $\mu\Omega$cm. This proved that the silicon oxide layer worked as an insulator. Unfortunately, no MR response could be measured when the sensor was placed in an external magnetic field. Bonding wires to the bondpads proved to be difficult and the high resistance of the connecting wires made detecting the very small changes in resistance impossible. The most promising way to be able to measure any MR response from these kind of prototype MR probes would be to use a lock–in amplifier and two connections to the MR sensor, with much lower resistance. The FIB process used can be optimized to lower the resistivity of the deposited wires, as the present resistivity of the wires is high compared to the values described in literature.

The MR response of the triangular element was simulated using a micromagnetic simulation package expanded to also calculate current densities. From the simulations the optimum location of the connections to the element was determined. The MR response proved to be the highest if one of the wires was connected at the ultimate tip end. The absolute MR response calculated for this geometry proved only to be about $0.04\ \Omega$. From these simulations it was concluded that a very pointed tip is not a good choice. The radius of the tip should be adjusted to the desired resolution to improve the MR response. Therefore new designs were developed. These had a higher MR response: the best geometry showed around $0.24\ \Omega$.

Before implementing the optimized shape of the element onto the tip plane of the CantiClever probe, different shapes of the elements, obtained from the simulations, were realized on a wafer scale and the magnetic properties were measured using MFM, Kerr microscopy and MR response measurements. At zero applied field, the elements showed a complicated domain structure at the sensing part of the element (i.e. the connection between the legs of the U–shape). This is not a desirable situation if the sensor is used for reading in a probe recording system, as it is a major source of noise. Therefore, biasing of the element will be necessary to be able to use the sensor for reading. The Kerr microscopy measurements showed very nicely the switching of the legs, when the sensor was placed in an external field. One leg switched at 20 Oe and the other at 50 Oe. The switching of the legs is probably not of great influence on the response of the sensor when used in a probe recording system, as the stray field from the medium is only present very close to the medium surface. The MR response proved to be 0.27% when the field was applied parallel to the legs of the element. For use as a reading sensor in a probe recording system, the response in this direction of the applied field would be the most important, as probe recording system would probably have a perpendicular medium. When the field was applied perpendicular to the legs, the MR response was 0.63%.

6.4 Recommendations

With the current CantiClever probes, bits with a length down to 27 nm could be resolved in MFM measurements on a commercial instrument in air. To be able to resolve even smaller magnetic features, the following improvements to the probe could be made. First of all, the tip planes of the probes could be made thinner. The fabrication process should allow probes to be made with tip planes as thin as 10 nm or even less. Second, the magnetic tip itself could be improved. So far, cobalt was chosen as a material for the magnetic tip, but other materials such as iron or metal alloys might provide a higher magnetic moment and therefore more signal. The use of an aluminum capping layer can protect the tip materials from corrosion. In the current process, this layer is around 10 nm thick. For smaller tips, it will be necessary to reduce this thickness. Experiments have to be done to find out what the lower limit on the thickness will be. For these advanced tips, the commercial instrument we used might not be good enough to get the best results from the tips. More sensitive electronics and performing the measurements in vacuum will be unavoidable at some point.

In this thesis, only a preliminary investigation into the possibilities for integration of other sensor on the CantiClever probe has been done. A proper manufacturing process has to be developed that integrates the sensor on the tip plane before the cantilevers are etched free from the substrate. The same holds true for the electrical connections. The challenge will be to find a process and materials that are compatible with the high temperatures and apparatus used to deposit the silicon nitride as well as the KOH wet etching process.

Although it might look as if the designed probe and fabrication process can be readily used for commercialization, there are still some things that might need to be improved. The wafer surface could be used more efficiently, so that more probes can be fabricated from a single wafer. Furthermore, the design could be adapted to improve the handling of the probes once the processing has finished.

Bibliography

[1] R. Young, J. Ward and F. Scire. "The Topografiner: An Instrument for Measuring Surface Microtopography". *Rev. Sci. Instrum.* **43**, 999–1011 (1972). 9, 10

[2] G. Binnig, H. Rohrer, Ch. Gerber and E. Weibel. "Surface Studies by Scanning Tunneling Microscopy". *Phys. Rev. Lett.* **49**, 57–61 (1982). 10

[3] G. Binnig, H. Rohrer, Ch. Gerber and E. Weibel. "7 x 7 Reconstruction on Si(111) Resolved in Real Space". *Phys. Rev. Lett.* **50**, 120–123 (1983). 10

[4] G. Binnig, C.F. Quate and Ch. Gerber. "Atomic Force Microscope". *Phys. Rev. Lett.* **56**, 930–933 (1986). 10

[5] Y. Martin, C.C. Williams and H.K. Wickramasinghe. "Atomic force microscope–force mapping and profiling on a sub 100–Å scale". *J. Appl. Phys.* **61**, 4723–4729 (1987). 10

[6] F.J. Giessibl and G. Binnig. "Investigation of the (001) cleavage plane of potassium bromide with an atomic force microscope at 4.2 K in ultra–high vacuum". *Ultramicroscopy* **42-44**, 281–289 (1992). 10

[7] Y. Martin and H.K. Wickramasinghe. "High-resolution magnetic imaging of domains in TbFe by force microscopy". *Appl. Phys. Lett.* **50**, 1455–1457 (1987). 10, 18, 19, 28

[8] J.J. Sàenz, N. Garcìa, P. Grütter, E. Meyer, H. Heinzelmann, R. Wiesendanger, L. Rosenthaler, H.R. Hidber and H.J. Güntherodt. "Observation of magnetic forces by the atomic force microscope". *J. Appl. Phys.* **62**, 4293–4295 (1987). 10, 19, 29

[9] J.C. Suits, R.H. Geiss, C.J. Lin, D. Rugar and A.E. Bell. "Lorentz microscopy of micron–sized laser–written magnetic domains in TbFe". *Appl. Phys. Lett.* **49**, 419–421 (1986). 11

[10] R. Wiesendanger, D. Bürgler, G. Tarrach, A. Wadas, D. Brodbeck, H.J. Güntherodt, G. Güntherodt, R.J. Gambino and R. Ruf. "Vacuum tunneling of spin-polarized electrons detected by scanning tunneling microscopy". *J. Vac. Sci. Technol. B* **9**, 519–524 (1991). 11

[11] P. Rice, S.E. Russek, J. Hoinville and M.H. Kelley. “Optimizing the NIST magnetic imaging reference sample”. *IEEE Trans. Magn.* **33**, 4065–4067 (1997). 12

[12] L. Abelmann, S. Porthun, M. Haast, C. Lodder, A. Moser, M. E. Best, P. J. A. Vanschendel, B. Stiefel, H. J. Hug, G. P. Heydon, A. Farley, S. R. Hoon, T. Pfaffelhuber, R. Proksch and K. Babcock. “Comparing the resolution of magnetic force microscopes using the CAMST reference samples”. *J. Magn. Magn. Mater.* **190**, 135–147 (1998). 12, 18, 85

[13] Y. Chen, X. Dang, Y. Liu, H. Jiang, K. Stoev, F. Liu, P. Luo, J. Wang, J. Chen, S. Gu, M. Lederman, M. Krounbi and M. Re. “Inductive Write Heads Using High–Moment Pole Materials for Ultrahigh–Density Demonstrations”. *IEEE Trans. Magn.* **39**, 2368–2370 (2003). 12

[14] E. Grochowksi. http://www.research.ibm.com (2002). 12, 13

[15] E.E. Fullerton, D.T. Margulies, M.E. Schabes, M. Carey, B. Gurney, A. Moser, M. Best, G. Zeltzer, K. Rubin and M. Doerner. “Antiferromagnetically coupled magnetic media layers for thermally stable high–density recording”. *Appl. Phys. Lett.* **77**, 3806–3808 (2000). 12

[16] S. Iwasaki and Y. Nakamura. “An analysis for the magnetization mode for high density magnetic recording”. *IEEE Trans. Magn.* **MAG-13**, 1272–1277 (1977). 12

[17] H. Takano, Y. Nishida, A. Kuroda, H. Sawaguchi, Y. Hosoe, T. Kawabe, H. Aoi, H. Muraoka, Y. Nakamura and K. Ouchi. “Realization of 52.5 Gb/in^2 perpendicular recording”. *J. Magn. Magn. Mater.* **235**, 241–244 (2001). 12

[18] J.J.M. Ruigrok, R. Coehoorn, S.R. Cumpson and H.W. Kesteren. “Disk recording beyond 100 Gb/inch^2: Hybrid recording?”. *J. Appl. Phys.* **87**, 5398–5403 (2000). 12

[19] S.Y. Chou, P.R. Krauss and L. Kong. “Nanolithographically defined magnetic structures and quantum magnetic disk”. *J. Appl. Phys.* **79**, 6101–6106 (1996). 12

[20] M.A.M. Haast, J.R. Schuurhuis, L. Abelmann, J.C. Lodder and Th.J. Popma. “Reversal mechanism of submicron patterned CoNi/Pt multilayers”. *IEEE Trans. Magn.* **34**, 1006–1008 (1998). 12

[21] P. Vettiger, M. Despont, U. Drechsler, U. Dürig, W. Häberle, M.I. Lutwyche, H.E. Rothuizen, R. Stutz, R. Widmer and G.K. Binnig. “The Millipede - More than one thousand tips for future AFM data storage”. *IBM J. Res. Develop.* **44**, 323–340 (2000). 14, 94

[22] M.I. Lutwyche, M. Despont, U. Drechsler, U. Dürig, W. Häberle, H. Rothuizen, R. Stutz, R. Widmer, G.K. Binnig and P. Vettiger. “Highly parallel data storage system based on scanning probe arrays”. *Appl. Phys. Lett.* **77**, 3299–3301 (2000). 14

[23] P. Vettiger, G. Cross, M. Despont, U. Drechsler, U. Dürig, B. Gotsmann, W. Häberle, M.A. Lantz, H.E. Rothuizen, R. Stutz and G.K. Binnig. "The 'Millipede'–Nanotechnology Entering Data Storage". *IEEE Trans. Nanotechnol.* **1**, 39–55 (2002). 14, 15

[24] H.J. Mamin and D. Rugar. "Thermomechanical writing with an atomic force microscope tip". *Appl. Phys. Lett.* **61**, 1003–1005 (1992). 14

[25] U. Drechsler, N. Bürer, M. Despont, U. Dürig, B. Gotsmann, F. Robin and P. Vettiger. "Cantilevers with nano-heaters for thermomechanical storage application". *Microelectron. Eng.* **67-68**, 397–404 (2003). 15

[26] E. Eleftheriou, T. Antonakopoulos, G.K. Binnig, G. Cherubini, M. Despont, A. Dholakia, U. Dürig, M.A. Lantz, H. Pozidis, H.E. Rothuizen and P. Vettiger. "Millipede-A MEMS–Based Scanning–Probe Data–Storage System". *IEEE Trans. Magn.* **39**, 938–945 (2003). 15

[27] L.R. Carley, J.A. Bain, G.K. Fedder, D.W. Greve, D.F. Guillou, M.S.C. Lu, T. Mukherjee, S. Santhanam, L. Abelmann and S. Min. "Single-chip computers with microelectromechanical systems–based magnetic memory". *J. Appl. Phys.* **87**, 6680–6685 (2000). 15, 16

[28] L.R. Carley, G.R. Ganger and D.F. Nagle. "MEMS–based integrated–circuit mass–storage systems". *Communications of the ACM* **43**, 72–80 (2000). 15

[29] L.R. Carley, G.R. Ganger, D.F. Guillou and D.F. Nagle. "Sytem design considerations for MEMS–Actuated Magnetic–Probe–Based Mass Storage". *IEEE Trans. Magn.* **37**, 657–662 (2001). 15

[30] R.T. El-Sayed and L.R. Carley. "Performance Analysis of Beyond 100 Gb/in^2 MFM–Based MEMS–Actuated Mass Storage Devices". *IEEE Trans. Magn.* **38**, 1892–1894 (2002). 15

[31] L. Kong, L. Zhuang and S.Y. Chou. "Writing and reading 7.5 Gbits/in^2 longitudinal quantized magnetic disk using magnetic force microscope tips". *IEEE Trans. Magn.* **33**, 3019–3021 (1997). 15

[32] L. Abelmann. "Opvolgers gezocht voor de harde schijf". *Natuur & Techniek* pages 23–29 (2001). 16

[33] P. Grütter, D. Rugar, H.J. Mamin, G. Castillo, C.J. Lin, I.R. McFadyen, R.M. Valletta, O. Wolter, T. Bayer and J. Greschner. "Magnetic force microscopy with batch–fabricated force sensors". *J. Appl. Phys.* **69**, 5883–5885 (1991). 18, 29

[34] M. Rührig, S. Porthun and J. C. Lodder. "Magnetic force microscopy using electron-beam fabricated tips". *Rev. Sci. Instrum.* **65**, 3224–3228 (1994). 18, 30

[35] L. Folks, M. E. Best, P. M. Rice, B. D. Terris, D. Weller and J. N. Chapman. "Perforated tips for high-resolution in-plane magnetic force microscopy". *Appl. Phys. Lett.* **76**, 909–911 (2000). 18, 30

[36] G.N. Phillips, L. Abelmann, M.H. Siekman and J.C. Lodder. "High resolution magnetic force microscopy using focussed ion beam modified tips". *Appl. Phys. Lett.* **81**, 865–867 (2002). 18, 31

[37] H.J. Hug, P. Kappenberger, S. Martin, P. Reimann, R. Hoffman, J. Rychen, W. Lu and H.J. Güntherodt. "High Resolution Quantitative Magnetic Force Microscopy". Unpublished result, presentation EB05, presented at Intermag 2002 (2002). 18

[38] P. Grütter, H.J. Mamin and D. Rugar. "Scanning Tunneling Microscopy" volume II chapter Magnetic Force Microscopy, pages 151–207. Springer, Berlin, Heidelberg, New York (1992). 17

[39] D. Rugar, H.J. Mamin, P. Guethner, S.E. Lambert, J.E. Stern, I. McFadyen and T. Yogi. "Magnetic force microscopy: General principles and application to longitudinal recording media". *J. Appl. Phys.* **68**, 1169–1183 (1990). 17, 20, 24, 29

[40] A. Wadas and H.J. Hug. "Models for the stray field from magnetic tips used in magnetic force microscopy". *J. Appl. Phys.* **72**, 203–206 (1992). 17, 22

[41] M.R. Koblischka, B. Hewener, U. Hartmann, A. Wienss, B. Christoffer and G. Persch-Schuy. "Magnetic force microscopy applied in magnetic data storage technology". *Appl. Phys. A–Mater.* **76**, 879–884 (2003). 17, 30

[42] H.J. Hug, B. Stiefel, P.J.A. van Schendel, A. Moser, R. Hofer, S. Martin and H.J. Güntherodt. "Quantitative magnetic force microscopy on perpendicular magnetized sampes". *J. Appl. Phys.* **83**, 5609–5620 (1998). 19, 20, 22, 26

[43] J.J. Sàenz, N. Garcìa and J. C. Slonczewski. "Theory of magnetic imaging by force microscopy". *Appl. Phys. Lett.* **53**, 1449–1451 (1988). 20

[44] A. Wadas and P. Grütter. "Theoretical approach to magnetic force microscopy". *Phys. Rev. B.* **39**, 12013–12017 (1989). 20, 22

[45] A. Wadas, P. Grütter and H.J. Güntherodt. "Analysis of magnetic bit pattern by magnetic force microscopy". *J. Vac. Sci. Technol. A* **8**, 416–420 (1990). 20

[46] A. Wadas, P. Grütter and H.J. Güntherodt. "Analysis of in-plane bit structure by magnetic force microscopy". *J. Appl. Phys.* **67**, 3462–3467 (1990). 20

[47] A. Wadas and H.J. Güntherodt. "The topography effect on magnetic images in magnetic force microscopy". *J. Appl. Phys.* **68**, 4767–4771 (1990). 20

[48] U. Hartmann. "Theory of magnetic force microscopy". *J. Vac. Sci. Technol. A* **8**, 411–415 (1990). 20

[49] J.O. Oti and P. Rice. "Micromagnetic simulations of tunneling stabilized magnetic force microscopy". *J. Appl. Phys.* **73**, 5802–5804 (1993). 20

[50] A. Aharoni and J.P. Jakubovics. "Effect of the MFM tip on the measured magnetic structure". *J. Appl. Phys.* **73**, 6498–6500 (1993). 20

[51] S. Müller-Pfeiffer, M. Schneider and W. Zinn. "Imaging of magnetic domain walls in iron with a magnetic force microscope: A numerical study". *Phys. Rev. B.* **49**, 15745–15752 (1994). 20

[52] S.L. Tomlinson and A.N. Farley. "Micromagnetic model for magnetic force microscopy tips". *J. Appl. Phys.* **81**, 5029–5031 (1997). 20

[53] B. Vellekoop, L. Abelmann, S. Porthun and J.C. Lodder. "On the determination of the internal magnetic structure by magnetic force microscopy". *J. Mag. Magn. Mater.* **190**, 148–151 (1998). 20

[54] S. Porthun, L. Abelmann, S. J. L. Vellekoop, J. C. Lodder and H. J. Hug. "Optimization of lateral resolution in magnetic force microscopy". *Appl. Phys. A–Mater.* **66**, S1185–S1189 (1998). 20, 22, 23, 24

[55] A. Wadas and H.J. Güntherodt. "Lateral resolution in magnetic force microscopy. Application to periodic structures". *Phys. Lett. A* **146**, 277–280 (1990). 22

[56] L. Abelmann, A.G. van den Bos and J.C. Lodder. "Magnetic Microscopy of Nanostructures" chapter Magnetic Force Microscopy–Towards higher resolution. Springer Verlag, Heidelberg (to be published). 22, 28

[57] T. R. Albrecht, P. Grütter, D. Horne and D. Rugar. "Frequency modulation detection using high–Q cantilevers for enhanced force mircoscope sensitivy". *J. Appl. Phys.* **69**, 668–673 (1991). 23, 58

[58] H. Saito, A.G. van den Bos, L. Abelmann and J.C. Lodder. "High–resolution MFM: Simulation of tip sharpening". *IEEE Trans. Magn.* **39**, 3447–3449 (2003). 25, 26, 27, 28

[59] Y. Martin, D. Rugar and H.K. Wickramasinghe. "High-resolution magnetic imaging of domains in TbFe by force microscopy". *Appl. Phys. Lett.* **52**, 244–246 (1988). 28, 29

[60] H.J. Mamin, D. Rugar, J.E. Stern, B.D. Terris and S.E. Lambert. "Force microscopy of magnetization patterns in longitudinal recording media". *Appl. Phys. Lett.* **53**, 1563–1565 (1988). 29

[61] P. Grütter, A. Wadas, E. Meyer, H.R. Hidber and H.J. Güntherodt. "High resolution magnetic force microscopy". *J. Vac. Sci. Technol. A* **8**, 406–410 (1990). 29

[62] A.J. den Boef. "Preparation of magnetic tips for a scanning force microscope". *Appl. Phys. Lett.* **56**, 2045–2047 (1990). 29

[63] O. Wolter, Th. Bayer and J. Greschner. "Micromachined silicon sensors for scanning force microscopy". *J. Vac. Sci. Technol. B* **9**, 1353–1357 (1991). 29

[64] M. Nonnenmacher, J. Greschner, O. Wolter and R. Kassing. "Scanning force microscopy with micromachined silicon sensors". *J. Vac. Sci. Technol. B* **9**, 1358–1362 (1991). 29

[65] P. Grütter, D. Rugar, H.J. Mamin, G. Castillo, S.E. Lambert, C.J. Lin, R.M. Valletta, O. Wolter, T. Bayer and J. Greschner. "Batch fabricated sensors for magnetic force microscopy". *Appl. Phys. Lett.* **57**, 1820–1822 (1990). 29

[66] S.H. Liou and Y.D. Yao. "Development of high coercivity magnetic force microscopy tips". *J. Magn. Magn. Mater.* **190**, 130–134 (1998). 29

[67] S.M. Casey, D.G. Lord, P.J. Grundy, M. Slade and D. Lambrick. "Single layer and multilayer tip coatings in magnetic force microscopy". *J. Appl. Phys.* **85**, 5166–5168 (1999). 29

[68] K. Sueoka, K. Okuda, N. Matsubara and F. Sai. "Study of tip magnetization behavior in magnetic force microscope". *J. Vac. Sci. Technol. B* **9**, 1313–1317 (1991). 29

[69] P.F. Hopkins, J. Moreland, S.S. Malhotra and S.H. Liou. "Superparamagnetic magnetic force microscopy tips". *J. Appl. Phys.* **79**, 6448–6450 (1996). 29

[70] O. Teschke. "Micromagnetic structure images taken using platinum coated tips". *Appl. Phys. Lett.* **79**, 2773–2775 (2001). 30

[71] Y. Akama, E. Nishimura, A. Sakai and H. Murakami. "New scanning tunneling microscopy tip for measuring surface topography". *J. Vac. Sci. Technol. A* **8**, 429–433 (1990). 30

[72] P. B. Fischer, M. S. Wei and S. Y. Chou. "Ultrahigh Resolution Magnetic Force Microscope Tip Fabricated Using Electron Beam Lithography". *J. Vac. Sci. Technol. B* **11**, 2570–2573 (1993). 30

[73] S.Y. Chou, M.S. Wei and P.B. Fischer. "An ultra-high resolution single-domain magnetic force microscope tip fabricated using nanolithography". *IEEE Trans. Magn.* **30**, 4485–4487 (1994). 30

[74] M. Rührig, S. Porthun, J. C. Lodder, S. McVitie, L. J. Heyderman, A. B. Johnston and J. N. Chapman. "Electron beam fabrication and characterization of high-resolution magnetic force microscopy tips". *J. Appl. Phys.* **79**, 2913–2919 (1996). 30

[75] M.R. Koblischka, U. Hartmann and T. Sulzbach. "Improvements of the lateral resolution of the MFM technique". *Thin Solid Films* **428**, 93–97 (2003). 30

[76] G. D. Skidmore and E. D. Dahlberg. "Improved spatial resolution in magnetic force microscopy". *Appl. Phys. Lett.* **71**, 3293–3295 (1997). 30

[77] P. Leinenbach, U. Memmert, J. Schelten and U. Hartmann. "Fabrication and characterization of advanced probes for magnetic force microscopy". *Appl. Surf. Sci.* **144-145**, 492–496 (1999). 30

[78] U. Memmert, A.N. Müller and U. Hartmann. "Probes for magnetic force microscopy imaging of soft magnetic samples". *Meas. Sci. Technol.* **11**, 1342–1347 (2000). 30

[79] I. Utke, P. Hoffmann, R. Berger and L. Scandella. "High-resolution magnetic Co supertips grown by a focused electron beam". *Appl. Phys. Lett.* **80**, 4792–4794 (2002). 30

[80] M.J. Vasile, D. Grigg, J.E. Griffith, E. Fitzgerald and P.E. Russell. "Scanning probe tip geometry optimized for metrology by focused ion beam ion milling". *J. Vac. Sci. Technol. B* **9**, 3569–3572 (1991). 30

[81] Z. Liu, Y. Dan, Q. Jinjun and Y. Wu. "Magnetic force microscopy using focused ion beam sharpened tip with deposited antiferroferromagnetic multiple layers". *J. Appl. Phys.* **91**, 8843–8845 (2002). 30

[82] S.H. Liou. "Comparison of magnetic images using point and thin-film magnetic force microscopy tips". *IEEE Trans. Mag.* **35**, 3989–3991 (1999). 31

[83] D. Litvinov and S. Khizroev. "Orientation–sensitive magnetic force microscopy for future probe storage applications". *Appl. Phys. Lett.* **81**, 1878–1880 (2002). 31

[84] S. Iijima. "Helical microtubules of graphitic carbon". *Nature* **354**, 56–58 (1991). 31

[85] H. Dai, J.H. Hafner, A.G. Rinzler, D.T. Colbert and R.E. Smalley. "Nanotubes as nanoprobes in scanning probe microscopy". *Nature* **384**, 147–150 (1996). 31

[86] T. Arie, H. Nishijima, S. Akita and Y. Nakayama. "Carbon-nanotube probe equipped magnetic force microscope". *J. Vac. Sci. Technol. B* **18**, 104–106 (2000). 31

[87] N. Yoshida, M. Yasutake, T. Arie, S. Akita and Y. Nakayama. "Quantitative Analysis of the Magnetic Properties of Metal-Capped Carbon Nanotube Probe". *Jpn. J. Appl. Phys.* **41**, 5013–5016 (2002). 31

[88] E. Yenilmez, Q. Wang, R.J. Chen, D. Wang and H. Dai. "Wafer scale production of carbon nanotube scanning probe tips for atomic force microscopy". *Appl. Phys. Lett.* **80**, 2225–2227 (2002). 31

[89] A. Hall, W.G. Matthews, R. Superfine, M.R. Falvo and S. Washburn. "Simple and efficient method for carbon nanotube attachment to scanning probes and other substrates". *Appl. Phys. Lett.* **82**, 2506–2508 (2003). 31

[90] R.C. Barret and C.F. Quate. "Charge storage in a nitride–oxide–silicon medium by scanning capacitance microscopy". *J. Appl. Phys.* **70**, 2725–2733 (1991). 34

[91] C.C. Williams and H.K. Wickramasinghe. "Scanning thermal profiler". *Appl. Phys. Lett.* **49**, 1587–1589 (1986). 34

[92] M. Nonnenmacher and H.K. Wickramasinghe. "Scanning probe microscopy of thermal conductivity and subsurface properties". *Appl. Phys. Lett.* **61**, 168–170 (1992). 34

[93] K. Luo, Z. Shi, J. Varesi and A. Majumdar. "Sensor nanofabrication, performance, and conduction mechanisms in scanning thermal microscopy". *J. Vac. Sci. Technol. B* **15**, 349–360 (1997). 34

[94] E. Oesterschulze. "Novel probes for scanning probe microscopy". *Appl. Phys. A–Mater.* **66**, S3–S9 (1998). 34

[95] A. Hammiche, L. Bozec, M. Conroy, H.M. Pollock, G. Mills, J.M.R. Weaver, D.M. Price, M. Reading, D.J. Hourston and M. Song. "Highly localized thermal, mechanical, and spectroscopic characterization of polymers using miniaturized thermal probes". *J. Vac. Sci. Technol. B* **18**, 1322–1332 (2000). 34

[96] S.R. Manalis, E.B. Cooper, P.F. Indermuhle, P. Kernen, P. Wagner, D.G. Hafeman, S.C. Minne and C.F. Quate. "Microvolume field–effect pH sensor for the scanning probe microscope". *Appl. Phys. Lett.* **76**, 1072–1074 (2000). 34

[97] E.B. Cooper, J. Fritz, G. Wiegand, P. Wagner and S. R. Manalis. "Robust microfabricated field-effect sensor for monitoring molecular adsorption in liquids". *Appl. Phys. Lett.* **79**, 3875–3877 (2001). 34

[98] W. Noell, M. Abraham, W. Ehrfeld, M. Lacher and K. Mayr. "Microfabrication of new sensors for scanning probe microscopy". *J. Micromech. Microeng.* **8**, 111–113 (1998). 34

[99] A.M. Chang, H.D. Hallen, L. Harriott, H.F. Hess, H.L. Kao, J. Kwo, R.E. Miller, R. Wolfe, J. van der Ziel and T.Y. Chang. "Scanning Hall probe microscopy". *Appl. Phys. Lett.* **61**, 1974–1976 (1992). 34

[100] A. Oral, S.J. Bending and M. Henini. "Real–time scanning Hall probe microscopy". *Appl. Phys. Lett.* **69**, 1324–1326 (1996). 34

[101] B.K. Chong, H. Zhou, G. Mills, L. Donaldson and J.M.R. Weaver. "Scanning Hall probe microscopy on an atomic force microscope tip". *J. Vac. Sci. Technol. A* **19**, 1769–1772 (2001). 34

[102] A.J. Brook, S.J. Bending, J. Pinto, A. Oral, D. Ritchie, H. Beere, M. Henini and A. Springthorpe. "Integrated piezoresistive sensors for atomic force–guided scanning Hall probe microscopy". *Appl. Phys. Lett.* **82**, 3538–3540 (2003). 34

[103] C2V. http://www.c2v.nl (2003). 36

[104] L. Meirovitch. "Fundamentals of vibrations". Mechanical Engineering Series. McGraw-Hill international edition 2001 edition (2001). 37

[105] Digital Instruments Inc. "Dimension 3100 Series Scanning Probe Microscope Instruction Manual" (1997). 38

[106] Nanosensors. http://www.nanosensors.com (2000). 39, 76

[107] T.D. Stowe K. Yasumura, T.W. Kenny, D. Botkin, K. Wago and D. Rugar. "Attonewton force detection using ultrathin silicon cantilevers". *Appl. Phys. Lett.* **71**, 288–290 (1997). 40

[108] K.Y. Yasumura, T.D. Stowe, E.M. Chow, T. Pfafman, T.W. Kenny, B.C. Stipe and D. Rugar. “Quality Factors in Micron- and Submicron–Thick Cantilevers”. *J. Microelectromech. S.* **9**, 117–125 (2000). 40, 53, 58, 60

[109] H.V. Jansen. “Plasma etching in microtechnology”. PhD thesis University of Twente (1996). 41

[110] P.G. Glöersen. “Ion–beam etching”. *J. Vac. Sci. Technol.* **12**, 28–35 (1975). 41

[111] J.M.E. Harper, J.J. Cuomo and H.R. Kaufman. “Technology and applications of broad–beam ion sources used in sputtering. Part II. Applications”. *J. Vac. Sci. Technol.* **21**, 737–756 (1982). 41

[112] M. Elwenspoek and H. Jansen. “Silicon micromachining”. Cambridge studies in semiconductor physics and microelectronic engineering. Cambridge University Press (1998). 41, 45

[113] R. Legtenberg, H. Jansen, M. de Boer and M. Elwenspoek. “Anisotropic reactive ion etching of silicon using $SF_6/O_2/$ CHF_3 gas mixtures”. *J. Electrochem. Soc.* **142**, 2020–2028 (1995). 41

[114] H. Jansen, M. de Boer, R. Legtenberg and M. Elwenspoek. “The black silicon method: a universal method for determining the parameter setting of a fluorine–based reactive ion etcher in deep silicon trench etching with profile control”. *J. Micromech. Microeng.* **5**, 115–120 (1995). 42

[115] H. Seidel, L. Csepregi, A. Heuberger and H. Baumgärtel. “Anisotropic etching of crystalline silicon in alkaline solutions”. *J. Electrochem. Soc.* **137**, 3612–3626 (1990). 42, 43, 45, 48, 52

[116] D.L. Kendall and G.R. Guel. “Micromachining and micropackaging of transducers” chapter Orientations of the third kind: the coming age of (110) silicon, pages 107–124. Elsevier Science Publishers (1985). 42, 52

[117] P. Krause and E. Obermeier. “Etch rate and surface roughness of deep narrow U–grooves in (110)–oriented silicon”. *J. Micromech. Microeng.* **5**, 112–114 (1995). 42, 45, 52

[118] L. Tenerz, Y. Bäcklund, J. Tiren and J. O’Connel. “Perpendicular walls fabricated in $\langle 100 \rangle$-oriented silicon by anisotropic wet etching”. *Sensor. Mater.* **1**, 313–320 (1989). 42

[119] H. Jansen, M. de Boer, J. Burger, R. Legtenberg and M. Elwenspoek. “The black silicon method II: the effect of mask material and loading on the reactive ion etching of deep silicon trenches”. *Microelectron. Eng.* **27**, 475–480 (1995). 43, 49

[120] M. Vangbo and Ylva Bäcklund. “Precise mask alignment to the crystallographic orientation of silicon wafers using wet anisotropic etching”. *J. Micromech. Microeng.* **6**, 279–284 (1996). 46, 47

[121] J.W. Gardner. “Microsensors principles and applications”. John Wiley & sons (1994). 48

[122] A. Merlos, M. Acero, M.H. Bao, J. Baussells and J. Esteve. “TMAH/IPA anisotropic etching characteristics”. *Sensor. Actuat. A–Phys.* **37-38**, 737–743 (1993). 48

[123] O. Tabata, R. Asahi, H. Funabashi, K. Shimaoka and S. Sugiyama. “Anisotropic etching of silicon in TMAH solutions”. *Sensor. Actuat. A–Phys.* **34**, 51–57 (1992). 48

[124] J.G.E. Gardeniers, H.A.C. Tilmans and C.C.G. Visser. “LPCVS silicon-rich nitride films for applications in mechanics, studied with statistical experimental design”. *J. Vac. Sci. Technol. A* **14**, 2879–2892 (1996). 48

[125] F.R. Blom, S. Bouwstra, M. Elwenspoek and J.H.J. Fluitman. “Dependence of the quality factor of micromachined beams on pressure and geometry”. *J. Vac. Sci. Technol. B* **10**, 19–26 (1992). 53, 58

[126] H. Hosaka, K. Itao and S. Kuroda. “Damping characteristics of beam–shaped micro-oscillators”. *Sensor. Actuat. A–Phys.* **49**, 87–95 (1995). 58, 60

[127] A.J. le Fèbre. “Fabrication and Characterization of Magnetic Nanowires”. Master’s thesis University of Twente (2003). 63

[128] Personal communication with M.H. Siekman (2002). 64

[129] K. Hong and N. Giordano. “New effects in ferromagnetic nanostructures”. *J. Magn. Magn. Mater.* **151**, 396–402 (1995). 64

[130] K. Matsuyama, S. Komatsu and Y.Nozaki. “Magnetic properties of nanostructured wires deposited on the side edge of patterned thin film”. *J. Appl. Phys.* **87**, 4724–4726 (2000). 64

[131] G. Dumpich, T.P. Krome and B. Hausmanns. “Magnetoresistance of single Co nanowires”. *J. Magn. Magn. Mater.* **248**, 241–247 (2002). 64, 80, 84

[132] L. Holland. “Vacuum deposition of thin films”. Chapman & Hall, London (1963). 65

[133] A.O. Adeyeye, J.A.C. Bland, C. Daboo and D.G. Hasko. “Magnetostatic interactions and magnetization reversal in ferromagnetic wires”. *Phys. Rev. B.* **56**, 3265–3270 (1997). 66

[134] A. Ercole, A.O. Adeyeye, C. Daboo, J.A.C. Bland and D. G. Hasko. “Finite size effects in the static and dynamic magnetic properties of FeNi wire array structures”. *J. Appl. Phys.* **81**, 5452–5454 (1997). 66

[135] L. Abelmann and J.C. Lodder. “Oblique evaporation and surface diffusion”. *Thin Solid Films* **305**, 1–21 (1997). 73

[136] D.X. Ye, Y.P. Zhao, G.R. Yang, Y.G. Zhao, G.C. Wang and T.M. Lu. "Manipulating the column tilt angles of nanocolumnar films by glancing–angle deposition". *Nanotechnology* **13**, 615–618 (2002). 73

[137] F. Tang, D.L. Liu, D.X. Ye, Y.P. Zhao, T.M. Lu and G.C. Wangg. "Magnetic properties of Co nanocolumns fabricated by oblique–angle deposition". *J. Appl. Phys.* **93**, 4194–4200 (2003). 73

[138] J.M. Alameda, F. Carmona, F.H. Salas, L.M. Alverez-Prado, R. Morales and G.T. Pérez. "Effects of the initial stages of film growth on the magnetic anisotropy of obliquely–deposited cobalt thin films". *J. Magn. Magn. Mater.* **154**, 249–253 (1996). 73

[139] R.L. Seliger, J.W. Ward, V. Wang and R.L. Kubena. "A high-intensity scanning ion probe with submicrometer spot size". *Appl. Phys. Lett.* **34**, 310–312 (1979). 74

[140] Digital Instruments Inc. http://www.veeco.com (2003). 76, 85

[141] U. Ebels, A. Radulescu, Y. Henry, L. Piraux and K. Ounadjela. "Spin Accumulation and Domain Wall Magnetoresistance in 35 nm Co Wires". *Phys. Rev. Lett.* **84**, 983–986 (2000). 76, 77, 78

[142] A. Radulescu, U. Ebels, Y. Henry, K. Ounadjela, J.L. Duvail and L. Piraux. "Magnetoresistance of a single domain wall in Co and Ni nanowires". *IEEE Trans. Magn.* **36**, 3062–3064 (2000). 77, 78

[143] W. Wernsdorfer, K. Hasselbach, A. Benoit, B. Barbara, B. Doudin, J. Meier, J.Ph. Ansermet and D. Mailly. "Measurements of magnetization switching in individual nickel nanowires". *Phys. Rev. B.* **55**, 11552–11559 (1997). 80

[144] R. Ferre, K. Ounadjela, J.M. George, L. Piraux and S. Dubois. "Magnetization processes in nickel and cobalt electrodeposited nanowires". *Phys. Rev. B.* **59**, 14066–14075 (1997). 80, 83

[145] P.M. Paulus, F. Luis, M. Kroöll, G. Schmid and L.J. de Jongh. "Low-temperature study of the magnetization reversal and magnetic anisotropy of Fe,Ni,and Co nanowires". *J. Magn. Magn. Mater.* **224**, 180–196 (2001). 80

[146] More information can be found on: http://magnet.atp.tuwien.ac.at. 82

[147] R. Hertel. "Computational micromagnetism of magnetization processes in nickel nanowires". *J. Magn. Magn. Mater.* **249**, 251256 (2002). 83

[148] B. Hausmanns, T.P. Krome, G. Dumpich, E.F. Wassermann, D. Hinzke, U. Nowak and K.D. Usadel. "Magnetization reversal process in thin Co nanowires". *J. Magn. Magn. Mater.* **240**, 297–300 (2002). 83

[149] F.G. Monzon, D.S. Patterson and M.L. Roukes. "Characterization of individual nanomagnets by the local Hall effect". *J. Magn. Magn. Mater.* **195**, 19–25 (1999). 83

[150] D.J. Sellmyer, M. Zheng and R. Skomski. “Magnetism of Fe, Co and Ni nanowires in self-assembled arrays”. *J. Phys.–Condens. Mat.* **13**, R433–R460 (2001). 83, 84

[151] A.O. Adeyeye, J.A.C. Bland, C. Daboo, Jaeyong Lee, U. Ebels and H. Ahmed. “Size dependence of the magnetoresistance in submicron FeNi wires”. *J. Appl. Phys.* **79**, 6120–6122 (1996). 84

[152] T. Oikawa, M. Nakamura, H. Uwazumi, T. Shimatsu, H. Muraoka and Y. Nakamura. “Microstructure and Magnetic Properties of CoPtCr-SiO_2 Perpendicular Recording Media”. *IEEE Trans. Magn.* **38**, 1976–1978 (2002). 86

[153] Personal communication with R. Jansen (2003). 88

[154] Personal communication with T. Shimatsu (2003). 91

[155] S.Y. Yamamoto and S. Schultz. “Scanning magnetoresistance microscopy”. *Appl. Phys. Lett.* **69**, 3263–3265 (1996). 93

[156] R. O’Barr, M. Lederman and S. Schultz. “A scanning microscope using a magnetoresistive head as the sensing element”. *J. Appl. Phys.* **79**, 6067–6069 (1996). 93

[157] G.N. Phillips, M. Eisenberg, E.A. Draaisma, L. Abelmann and J.C. Lodder. “Performance of focused ion beam trimmed yoke-type magnetoresistive heads for magnetic microscopy”. *IEEE Trans. Magn.* **38**, 3528–3535 (2002). 93

[158] M. Nakamura, M. Kimura, K. Sueoka and K. Mukasa. “Scanning magnetoresistance microscopy with a magnetoresistive sensor cantilever”. *Appl. Phys. Lett.* **80**, 2713–2715 (2002). 93

[159] M. Nakamura, K. Sueoka and K. Mukasa. “Improvement of the MR Cantilever for Scanning Magnetoresistance Microscope”. *Trans. Magn. Soc. Japan* **2**, 7–10 (2002). 93

[160] K. Ramstöck. http://www.ramstock.de (2003). 94

[161] K. Gamo, N. Takakura, N. Samoto, R. Shimizu and S. Namba. “Ion beam assisted deposition of metal organic films using focused ion beams”. *Jpn. J. Appl. Phys.* **23**, L293 (1984). 102

[162] Z. Xu, T. Kosugi, K. Gamo and S. Namba. “An x-ray photoelectron spectroscopy study on ion beam induced deposition of tungsten using WF_6”. *J. Vac. Sci. Technol. B* **7**, 1959–1962 (1989). 102

[163] G.M. Shedd, H. Lezec, A.D. Dubner and J. Melngailis. “Focused ion beam induced deposition of gold”. *Appl. Phys. Lett.* **49**, 1584–1586 (1986). 102

[164] A.D. Dubner and A. Wagner. “The role of gas adsorpsion in ion–beam–induced deposition of gold”. *J. Appl. Phys.* **66**, 870–874 (1989). 102

[165] A. Wagner, J.P. Levin, J.L. Mauer, P.G. Blauner, S.J. Kirch and P. Longo. "X-ray mask repair with focused ion beams". *J. Vac. Sci. Technol. B* **8**, 1557–1564 (1990). 102

[166] T. Tao, W. Wilkonson and J. Melngailis. "Focused ion beam induced deposition of platinum for repair processes". *J. Vac. Sci. Technol. B* **9**, 162–164 (1991). 102

[167] T. Tao, J. Ro, J. Melngailis, Z. Xue and H.D. Kaesz. "Focused ion beam induced deposition of platinum". *J. Vac. Sci. Technol. B* **8**, 1826–1829 (1990). 102, 104, 107

[168] Personal communication with FEI Company (2002). 105

[169] A. van der Ziel. "Noise in solid state devices and circuits". John Wiley & Sons (1986). 105

[170] P.R. Gray, P.J. Hurst, S.H. Lewis and R.G. Meyer. "Analysis and design of analog integrated circuits". John Wiley & Sons (2001). 105

[171] M. Vargas and R. Pallàs-Areny. "Thermal noise in a finite bandwidth". *IEEE Instrum. Meas. Mag.* **4**, 23–25 (2001). 105

[172] B.H. Jo and R.W. Vook. "In-situ ultra-high vacuum studies of electromigration in copper films". *Thin Solid Films* **262**, 129–134 (1995). 106

[173] W. Moritz, U. Roth amd M. Heyde, K. Rademann, M. Reichling and J. Hartmann. "Submicrosecond range surface heating and temperature measurement for efficient sensor reactivation". *Thin Solid Films* **391**, 143–148 (2001). 106

[174] P.G. Blauner, Y. Butt, J.S. Ro, C.V. Thompson and J. Melngailis. "Focused ion beam induced deposition of low-resistivity gold films". *J. Vac. Sci. Technol. B* **7**, 1816–1818 (1989). 107

[175] This work was carried out in co–operation with Bogdan Craus, and will be published in the near future. 107

[176] C.S. Doppen. "The design and building of a Kerr microscope". Master's thesis University of Twente (2003). 111

Appendix

CantiClever processing scheme

wafers:
orientation: $\langle 110 \rangle$
size: 100 mm type: P/Boron
polished: DSP
thickness: 380 μm
resistivity: 5–10 Ωcm

A. Finding the $\langle 111 \rangle$ orientation of $\langle 110 \rangle$ wafers

- **Wafer thickness measurement**
- **Cleaning introduction**
  fuming nitric acid (II) 5 min
  quick dump rinse, DI, < 0.1 μS
  boiling 70% nitric acid (95°C), 15 min
  quick dump rinse, DI, < 0.1 μS
  spin drying
- **Native oxide strip**
  60 s HF (1 %) dip
  quick dump rinse, DI, < 0.1 μS
  spin drying
  store wafers in a cleaned wafer box
- **LPCVD SiRN–S+A 50 nm**
  Tempress LPCVD Furnace Tube 6 S+A
  program N3 (SiRN)
  SiH_2Cl_2 flow: 70 sccm
  NH_3 flow: 18 sccm
  temperature: 850°C
  pressure: 200 mTorr
  measure deposition rate on dummy wafer
  Nf: 2.14, stress: $10.6 \cdot 10^{-10}$ dyne/cm^2
- **Lithography Olin907-17**
  hotplate 120°C, 10 min

HMDS: 4000 rpm, 20 s
resist: Olin 907-17, 4000 rpm, 20 s
prebake: hotplate 95°C, 90 s
vangbo mask, frontside, hard contact
after exposure bake: 120°C, 60 s
development: OPD 4262, 30+30 s
quick dump rinse, DI, $< 0.1\ \mu$S
spin drying
visual microscopic inspection

- **Plasma etching of SiN**
  Elektrotech PF 310/340 (Etske)
  dirty chamber, styros electrode
  electrode temp.: 10°C
  CHF_3 flow 25 sccm, O_2 flow 5 sccm
  pressure: 10 mTorr
  power: 75 W
  etchrate SiRN 60–90 nm/min, etchrate Olin resist 95 nm/min
- **Photoresist stripping by oxygen plasma**
  O_2 flow 55 sccm
  power: 120 W
  electrode temperature: 150°C
  pressure: 2.00 mbar
  time: 15 min
- **Etching native oxide**
  etchant HF (1 %)
  time $>$ 60 sec
  quick dump rinse, DI, $< 0.1\ \mu$S
  spin drying
- **Etching Si KOH**
  prepare 25 weight % KOH p.a. (500 gr KOH – 1500 ml DI)
  etch temp.: 75°C
  stirrer
  mask etch rates: SiO_2 (thermisch): 180 nm/hr, SiRN: $<$ 1 nm/min
  etchrate $\langle 100 \rangle$: 1 μm/min
  etchrate $\langle 110 \rangle$: 1.8 μm/min
  etchrate $\langle 111 \rangle$: 12.5 μm/min
  quick dump rinse, DI, $< 0.1\ \mu$S
  spin drying
- **Inspection**
  locate correct underetched structure for future alignment
- **Cleaning RCA-2**
  chemicals:
  HCL (37 weight % as HCL)
  H_2O_2 (30 %, "not stabilized") mixture HCL:H_2O: H_2O_2 (1:5:1) volume %

add HCL to H_20
add H_2O_2 when mixture is 70°C
temperature 75-80°C
time 10-15 min
quick dump rinse, DI, $< 0.1\ \mu$S
spin drying

- **Cleaning online**
  fuming nitric acid (I), 5 min
  fuming nitric acid (II), 5 min
  quick dump rinse, DI, $< 0.1\ \mu$S
  boiling nitric acid (95C), 15 min
  quick dump rinse, DI, $< 0.1\ \mu$S
  spin drying

B. Alignment & CantiClever marks

- **Lithography Olin907-17**
  hotplate 120°C, 10 min
  HMDS: 4000 rpm, 20 s
  resist: Olin 907-17, 4000 rpm, 20 s
  prebake: hotplate 95°C, 90 s
  alignment mark mask, frontside, hard contact
  align to correct vangbo–marks
  after exposure bake: 120°C, 60 s
  development: OPD 4262, 30+30 s
  quick dump rinse, DI, $< 0.1\ \mu$S
  spin drying
  visual microscopic inspection

- **Plasma etching of SiN**
  Elektrotech PF 310/340 (Etske)
  dirty chamber-styros electrode
  electrode temp.: 10°C
  CHF_3 flow 25 sccm, O_2 flow 5 sccm
  pressure: 10 mTorr
  power: 75 W
  etchrate SiRN 60-90 nm/min, etchrate Olin resist 95 nm/min

- **Plasma etching of Si**
  Elektrotech PF 310/340 (Etske)
  clean chamber, styros electrode
  electrode temp.: 10°C
  SF_6 flow 50 sccm
  pressure: 75 mTorr
  power: 75 W
  etchrate Si 0.75–0.8 μm/min, etchrate Olin resist 95 nm/min
  profile: isotropic

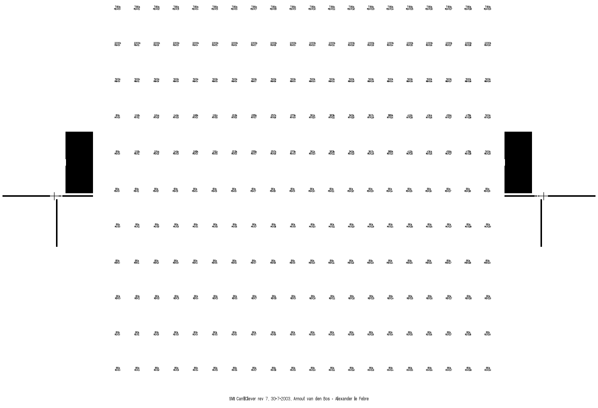

Figure A-1: *Mask for defining the alignment marks on the wafer required for aligning the next masks.*

- **Photoresist stripping by oxygen plasma**
  O_2 flow 55 sccm
  power: 120 W
  electrode temperature: 150°C
  pressure: 2.00 mbar
  time: 15 min

- **Cleaning online**
  fuming nitric acid (I), 5 min
  fuming nitric acid (II), 5 min
  quick dump rinse, DI, $< 0.1\ \mu$S
  boiling nitric acid (95C), 15 min
  quick dump rinse, DI, $< 0.1\ \mu$S
  spin drying

- **Etching native oxide**
  etchant HF (1 %)
  time $>$ 60 sec
  quick dump rinse, DI, $< 0.1\ \mu$S
  spin drying

- **LPCVD SiRN–S+A 150 nm**
  Tempress LPCVD Furnace Tube 6 S+A
  program N3 (SiRN)
  SiH_2Cl_2 flow: 70 sccm
  NH_3 flow: 18 sccm
  temperature: 850°C
  pressure: 200 mTorr

measure deposition rate on dummy wafer
Nf: 2.14, stress: $10.6 \cdot 10^{-10}$ dyne/cm^2

C. Windows etching

- **Lithography Olin907-17**
  hotplate 120°C, 10 min

  frontside:
  HMDS: 4000 rpm, 20 s
  resist: Olin 907-17, 4000 rpm, 20 s
  prebake: hotplate 95°C, 90 s
  postbake: 120°C, 10 min

  backside
  HMDS: 4000 rpm, 20 s
  resist: Olin 907-17, 4000 rpm, 20 s
  prebake: hotplate 95°C, 90 s
  backside window mask, backside, hard contact
  align to to alignment mask mark # 3 (front to back alignment!)
  after exposure bake: 120°C, 60 s
  development: OPD 4262, 30+30 s
  quick dump rinse, DI, $< 0.1\ \mu$S
  spin drying
  visual microscopic inspection

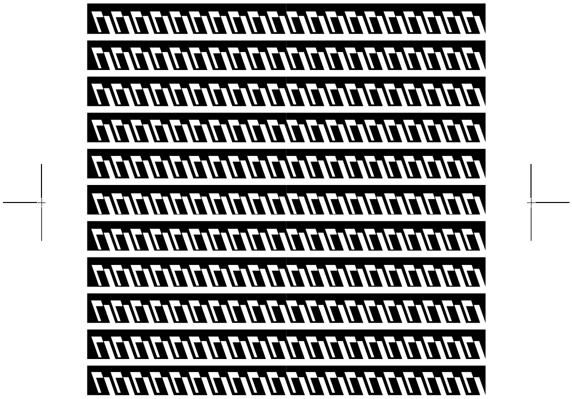

Figure A-2: *Mask for defining windows at the backside of the wafer.*

- **Plasma etching of SiN**
  Elektrotech PF 310/340 (Etske)

etch the backside, 200 nm of SiN
dirty chamber-styros electrode
electrode temp.: 10°C
CHF_3 flow 25 sccm, O_2 flow 5 sccm
pressure: 10 mTorr
power: 75 W
etchrate SiRN 60-90 nm/min, etchrate Olin resist 95 nm/min

- **Photoresist stripping by oxygen plasma**
  etch the backside O_2 flow 55 sccm
  power: 120 W
  electrode temperature: 150°C
  pressure: 2.00 mbar
  time: 15 min

- **Etching Si KOH**
  etching of the backside windows
  prepare 25 weight % KOH p.a. (500 gr KOH – 1500 ml DI)
  etch temp.: 75°C
  stirrer
  mask etch rates: SiO_2 (thermisch): 180 nm/hr, SiRN: < 1 nm/min
  etchrate $\langle 100 \rangle$: 1 μm/min
  etchrate $\langle 110 \rangle$: 1.8 μm/min
  etchrate $\langle 111 \rangle$: 12.5 μm/min
  etch until 50 μm left
  measured etch rate 1.76 μm/min
  check on the Dektak after 2 hours of etching
  quick dump rinse, DI, < 0.1 μS
  spin drying

- **Cleaning RCA-2**
  chemicals:
  HCL (37 weight % as HCL)
  H_2O_2 (30 %, "not stabilized") mixture HCL:H_2O: H_2O_2 (1:5:1) volume %
  add HCL to H_20
  add H_2O_2 when mixture is 70°C
  temperature 75-80°C
  time 10-15 min
  quick dump rinse, DI, < 0.1 μS
  spin drying

- **Cleaning online**
  fuming nitric acid (I), 5 min
  fuming nitric acid (II), 5 min
  quick dump rinse, DI, < 0.1 μS
  boiling nitric acid (95C), 15 min
  quick dump rinse, DI, < 0.1 μS
  spin drying

D. Support planes and cantilever patterns

- **Lithography Olin907-17**
  hotplate 120°C, 10 min
  HMDS: 4000 rpm, 20 s
  resist: Olin 907-17, 4000 rpm, 20 s
  prebake: hotplate 95°C, 90 s
  cantilever + support plane mask, frontside, hard contact
  alignment to alignment mask mark #4
  after exposure bake: 120°C, 60 s
  development: OPD 4262, 30+30 s
  quick dump rinse, DI, $< 0.1\ \mu$S
  spin drying
  visual microscopic inspection

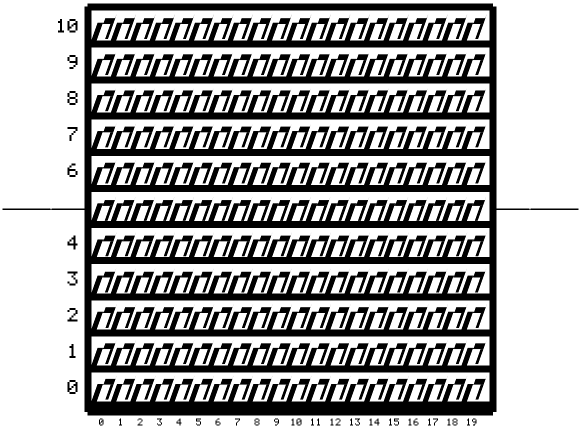

Figure A-3: *Mask for defining the cantilevers and support planes.*

- **Plasma etching of SiN**
  Elektrotech PF 310/340 (Etske)
  dirty chamber-styros electrode
  electrode temp.: 10°C
  CHF_3 flow 25 sccm, O_2 flow 5 sccm
  pressure: 10 mTorr
  power: 75 W
  etchrate SiRN 60-90 nm/min, etchrate Olin resist 95 nm/min

- **Photoresist stripping by oxygen plasma**
  O_2 flow 55 sccm
  power: 120 W
  electrode temperature: 150°C
  pressure: 2.00 mbar

time: 15 min

- **Cleaning online**
  fuming nitric acid (I), 5 min
  fuming nitric acid (II), 5 min
  quick dump rinse, DI, $< 0.1\ \mu$S
  boiling nitric acid (95C), 15 min
  quick dump rinse, DI, $< 0.1\ \mu$S
  spin drying
- **Etching native oxide**
  etchant HF (1 %)
  time > 60 sec
  quick dump rinse, DI, $< 0.1\ \mu$S
  spin drying
- **LPCVD SiRN–S+A**
  deposit desired tip plane thickness
  Tempress LPCVD Furnace Tube 6 S+A
  program N3 (SiRN)
  SiH_2Cl_2 flow: 70 sccm
  NH_3 flow: 18 sccm
  temperature: 850°C
  pressure: 200 mTorr
  for small thicknesses, first do a test run on a dummy wafer!
  Nf: 2.14, stress: $10.6 \cdot 10^{-10}$ dyne/cm^2

E. Tip planes

- **Lithography Olin907-17**
  hotplate 120°C, 10 min
  HMDS: 4000 rpm, 20 s
  resist: Olin 907-17, 4000 rpm, 20 s
  prebake: hotplate 95°C, 90 s
  tip plane mask, frontside, hard contact
  alignment to alignment mask mark #5
  after exposure bake: 120°C, 60 s
  development: OPD 4262, 30+30 s
  quick dump rinse, DI, $< 0.1\ \mu$S
  spin drying
  visual microscopic inspection
- **Plasma etching of SiN**
  Elektrotech PF 310/340 (Etske)
  etch only the tip planes, time etch stop!
  dirty chamber-styros electrode
  electrode temp.: 10°C
  CHF_3 flow 25 sccm, O_2 flow 5 sccm
  pressure: 10 mTorr

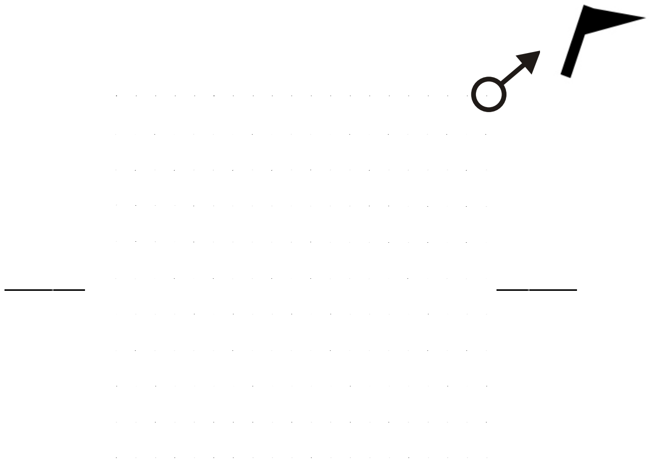

Figure A-4: *Mask for defining the tip planes.*

power: 75 W
etchrate SiRN 60-90 nm/min, etchrate Olin resist 95 nm/min

- **Photoresist stripping by oxygen plasma**
  O_2 flow 55 sccm
  power: 120 W
  electrode temperature: 150°C
  pressure: 2.00 mbar
  time: 15 min

F. Tip sharpening planes

- **Lithography Olin907-17**
  hotplate 120°C, 10 min
  HMDS: 4000 rpm, 20 s
  resist: Olin 907-17, 4000 rpm, 20 s
  prebake: hotplate 95°C, 90 s
  sharpening plane mask, frontside, hard contact
  alignment to alignment mask mark #6
  after exposure bake: 120°C, 60 s
  development: OPD 4262, 30+30 s
  quick dump rinse, DI, $< 0.1\ \mu$S
  spin drying
  Check resist pattern to tip plane alignment in microscope!
- **Evaporation of chromium**
  evaporate 90 nm of chromium in Balzers BAK600

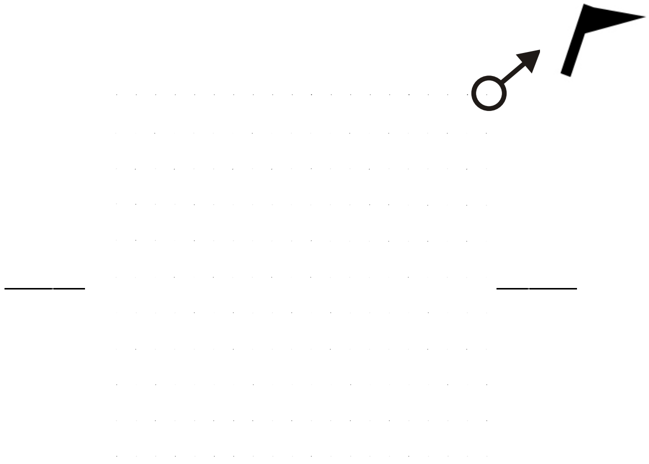

Figure A-5: *Mask for defining the chromium sharpening planes.*

- **Lift–off**
  acetone, room temperature
  don't use ultrasonic agitation!

G. KOH etch of cantilevers

- **Etching Si KOH**
  etching of the backside windows
  prepare 25 weight % KOH p.a. (500 gr KOH – 1500 ml DI)
  etch temp.: 75°C
  NO STIRRER!
  mask etch rates: SiO_2 (thermisch): 180 nm/hr, SiRN: < 1 nm/min
  etchrate $\langle 100 \rangle$: 1 μm/min
  etchrate $\langle 110 \rangle$: 1.8 μm/min
  etchrate $\langle 111 \rangle$: 12.5 μm/min
  monitor front underetching of cantilevers after 1.5 hours
  stop when etched through the wafer
  etch rate of cantilever frontside: approx. 4 μm/min
  vertical etch rate: approx. 1.4 μm/min
  spin drying no longer possible
  dry using ethanol

H. Tip plane sharpening

- **Plasma etching of SiN**
  Elektrotech PF 310/340 (Etske)
  etch until wafer is free of SiN ”left–overs”
  dirty chamber-styros electrode
  electrode temp.: 10°C
  CHF_3 flow 25 sccm, O_2 flow 5 sccm
  pressure: 10 mTorr
  power: 75 W
  etchrate SiRN 60-90 nm/min, etchrate Olin resist 95 nm/min

I. chromium removal

- **Wet etching chromium**
  Standard Cr–etchant
  recipe:
  perchloric acid ($HClO_4$) 60%: 10 ml
  cerium ammonium nitrate: 33 gr
  demiwater: 100 ml
  etch rate approx. : 100 nm/min

- **Cleaning**
  HF dip 2 min (removal of KOH residu)
  dip in demiwater beaker
  immerse in beaker with ethanol
  dry wafers

Test structure processing scheme

wafers:
orientation: $\langle 100 \rangle$
size: 100 mm type: P/Boron
polished: SSP
thickness: 550 μm
resistivity: 10 Ωcm

A. Fabrication starting substrate

- **Cleaning introduction**
  fuming nitric acid (II) 5 min
  quick dump rinse, DI, < 0.1 μS
  boiling 70% nitric acid (95°C), 15 min
  quick dump rinse, DI, < 0.1 μS
  spin drying

- **Wet Oxidation 1150°C**
  S+A Tempress Omega Junior III
  check water level
  gasses: H_2O+N_2
  temperature: 1150°C
  determine oxidation time by oxidation chart
  Nf: 1.46, thickness: 0.4 μm, 5 min (2 hours total time)

- **Cleaning online**
  fuming nitric acid (I), 5 min
  fuming nitric acid (II), 5 min
  quick dump rinse, DI, < 0.1 μS
  boiling nitric acid (95C), 15 min
  quick dump rinse, DI, < 0.1 μS
  spin drying

- **LPCVD SiRN–S+A**
  deposit desired tip thickness
  Tempress LPCVD Furnace Tube 6 S+A
  program N3 (SiRN)
  SiH_2Cl_2 flow: 70 sccm
  NH_3 flow: 18 sccm
  temperature: 850°C
  pressure: 200 mTorr
  for small thicknesses, first do a test run on a dummy wafer!
  Nf: 2.14, stress: $10.6 \cdot 10^{-10}$ dyne/cm^2

B. Forming alignment marks

- **Lithography Olin907-17**
  hotplate 120°C, 10 min
  HMDS: 4000 rpm, 20 s
  resist: Olin 907-17, 4000 rpm, 20 s
  prebake: hotplate 95°C, 90 s
  AML mask, frontside, hard contact
  after exposure bake: 120°C, 60 s
  development: OPD 4262, 30+30 s
  quick dump rinse, DI, < 0.1 μS
  spin drying

- **Plasma etching of SiN and SiO_2**
  Elektrotech PF 310/340 (Etske)
  dirty chamber-styros electrode
  electrode temp.: 10°C
  CHF_3 flow 25 sccm, O_2 flow 5 sccm
  pressure: 10 mTorr
  power: 75 W
  etchrate SiRN 60-90 nm/min, etchrate SiO_2 60-90 nm/min
  etchrate Olin resist 95 nm/min

- **Resist stripping HNO_3**
  HNO_3 (100%) Selectipur: MERCK 100453
  use beaker of resist stripping
  time: 20 min
  quick dump rinse, DI, $< 0.1\ \mu$S
  spin drying
- **Cleaning online**
  fuming nitric acid (I), 5 min
  fuming nitric acid (II), 5 min
  quick dump rinse, DI, $< 0.1\ \mu$S
  boiling nitric acid (95C), 15 min
  quick dump rinse, DI, $< 0.1\ \mu$S
  spin drying

C. Forming SiN strips

- **Lithography Olin907-12**
  hotplate 120°C, 10 min
  HMDS: 4000 rpm, 20 s
  resist: Olin 907-17, 4000 rpm, 20 s
  prebake: hotplate 95°C, 60 s
  PSV mask, frontside, hard contact
  after exposure bake: 120°C, 60 s
  development: OPD 4262, 30+30 s
  quick dump rinse, DI, $< 0.1\ \mu$S
  spin drying
- **Plasma etching of SiN**
  Elektrotech PF 310/340 (Etske)
  dirty chamber-styros electrode
  electrode temp.: 10°C
  CHF_3 flow 25 sccm, O_2 flow 5 sccm
  pressure: 10 mTorr
  power: 75 W
  etchrate SiRN 60-90 nm/min, etchrate Olin resist 95 nm/min
- **Resist stripping HNO_3**
  HNO_3 (100%) Selectipur: MERCK 100453
  use beaker of resist stripping
  time: 20 min
  quick dump rinse, DI, $< 0.1\ \mu$S
  spin drying
- **SiN thickness measurement**
  Dektak
- **Cleaning online**
  fuming nitric acid (I), 5 min
  fuming nitric acid (II), 5 min

quick dump rinse, DI, < 0.1 μS
boiling nitric acid (95C), 15 min
quick dump rinse, DI, < 0.1 μS
spin drying

D. Forming free hanging SiN planes

- **Lithography Olin907-12**
  hotplate 120°C, 10 min
  HMDS: 4000 rpm, 20 s
  resist: Olin 907-17, 4000 rpm, 20 s
  prebake: hotplate 95°C, 60 s
  PSH mask, frontside, hard contact
  after exposure bake: 120°C, 60 s
  development: OPD 4262, 30+30 s
  quick dump rinse, DI, < 0.1 μS
  spin drying
- **Evaporation of chromium**
  evaporate 50 nm of chromium in Balzers BAK600
- **Lift–off**
  acetone, room temperature
  use ultrasonic agitation
- **Plasma etching of SiN**
  Elektrotech PF 310/340 (Etske)
  dirty chamber-styros electrode
  electrode temp.: 10°C
  CHF_3 flow 25 sccm, O_2 flow 5 sccm
  pressure: 10 mTorr
  power: 75 W
  etchrate SiRN 60-90 nm/min, etchrate Olin resist 95 nm/min
- **Wet etching of chromium**
  etchant: LSI Selectipur, MERCK 111547
  etch rate approx.: 5 nm/min!
  quick dump rinse, DI, < 0.1 μS
  spin drying
- **SiN thickness measurement**
  Dektak
  in two directions!
- **Etching HF 50% SiO_2**
  HF 50%
  quick dump rinse, DI, < 0.1 μS
  etchrate thermal oxide: 60-80 nm/min
  etchrate SiN: 5 nm/min
  etch rate SiO_2: 500 nm/min

0:25 min for underetching
spin drying

- **Inspection SiN structure**
  optical microscope/SEM
  look for underetch

- **Cleaning online**
  fuming nitric acid (I), 5 min
  fuming nitric acid (II), 5 min
  quick dump rinse, DI, $< 0.1\ \mu$S
  boiling nitric acid (95C), 15 min
  quick dump rinse, DI, $< 0.1\ \mu$S
  spin drying

E. Side-edge evaporation of cobalt

- **Evaporation of cobalt**
  evaporate desired cobalt thickness in Balzers BAK600
  use dedicated holder
  alignment to source with correct angle:
  tip plane thickness 200 nm: 2.3°
  tip plane thickness 50 nm: 0.6°

- **Inspection cobalt tip**
  SEM

F. Deposition aluminum electrodes

- **Lithography Olin907-12**
  hotplate 120°C, 10 min
  HMDS: 4000 rpm, 20 s
  resist: Olin 907-17, 4000 rpm, 20 s
  prebake: hotplate 95°C, 60 s
  PWE mask, frontside, hard contact
  after exposure bake: 120°C, 60 s
  development: OPD 4262, 30+30 s
  quick dump rinse, DI, $< 0.1\ \mu$S
  spin drying

- **Evaporation of aluminum**
  evaporate 100 nm in Balzers BAK600
  use dedicated holder
  alignment to source with angle of 60°

- **Lift–off**
  acetone, room temperature
  don’t use ultrasonic agitation!

G. Dicing wafer

- **Spin resist, apply dicing foil**
  HMDS: 4000 rpm, 20 s
  resist: Olin 907-17, 4000 rpm, 20 s
  prebake: hotplate 95C, 60 s
  dicing foil backside
- **Dicing**
  Micro Automation 1006, blade type TC100
  speed: 1 mm/s
  cut width: 50 μm
  index1: 8 mm, index2: 8 mm
  height: 0.135 mm, thickness: 1.3 mm
  wafer diameter: 100 mm
  stopcount 1: 9, stopcount 2: 9
- **Remove foil, resist**
  remove Olin 907 in aceton (technical)
  spin drying or isopropanol
  visual microscopic inspection

H. Wirebonding

- **Bonding of aluminum wires**
  WeldEquip Westbond
  wire thickness 25 μm

Summary

Magnetic force microscopy (MFM) is a scanning probe technique that is used to generate a high–resolution image of stray fields above a magnetic thin film, with very little sample preparation. This makes the MFM the instrument of choice for the analysis of bit patterns in hard disks. The tremendous increase in data density of magnetic storage systems has pushed the bit size down into the nanometer range, close to the maximum resolution of current MFM's. This resolution, which is currently limited by the geometry of the magnetic tip, has to be improved, or the hard disk research community will loose a very powerful imaging technique. In this thesis a new probe for magnetic microscopy and recording, called the CantiClever, is presented. This probe is designed to address the issue of the tip geometry of conventional MFM tips. The new probe also allows for integration of other sensors besides an MFM tip with relative ease due to its planar fabrication process.

The first chapter provides a background to the research presented in this thesis. The principles and applications of different scanning probe microscopy techniques are described, with special attention to the field of MFM. Furthermore, the application of scanning probe techniques in future data storage systems is discussed.

The topic of chapter 2 is one of the key components of an MFM: the probe with the magnetic tip. The image formation process of an MFM is described and a definition of the resolution of an MFM is given. Using this theory, it is shown that the tip that gives the highest resolution is a bar shaped tip with a flat front end. In calculations, the influence of deviations from the optimal tip shape on the resolution that can be achieved are determined. It is shown that a tip with an ellipsoidal tip end is a good candidate for a high resolution MFM tip because of the absence of gap–zeros in its transfer function and a much smaller dependence of the resolution on the thickness of the tip. Next, an overview is given of the development of the magnetic tip towards the ultimate MFM tip since the invention of the MFM in 1987. Despite the efforts in micromachined tips, most of the tips suited for very high resolution MFM are still made by hand. In this chapter, a novel design of a cantilever and tip for MFM, called the CantiClever, is presented. This novel design enables the fabrication of a nearly

ideally shaped tip for MFM in a batch fabrication process, while at the same time enables the integration of other sensors at the end of a cantilever.

In chapter 3, the fabrication process of the CantiClever probe is described. This process deviates from that of existing probe designs for magnetic imaging in two ways. First, the tip of the probe consists of a lithographically defined silicon nitride film instead of a silicon pyramid that is defined by the crystallographic orientation of the wafer used. Second, the silicon cantilever of the probe is fabricated tilted 90 degrees with respect the wafer plane in comparison to conventional silicon cantilevers. The cantilever and base of the probe are fabricated from $\langle 110 \rangle$ silicon wafers using a two step KOH wet anisotropic etching process. In the first step windows are etched from the backside of the wafer to determine the final cantilever width. In the second step the cantilevers and tip planes are etched free from the front side. With this fabrication process 220 probes could be made on a 100 mm wafer, with tip planes as thin as 37 nm. A radius of curvature of the tip end of around 30 nm could be achieved. The quality factor of the cantilevers has been measured to be around 600 for a 67 kHz cantilever in air and around 50000 in vacuum conditions.

Chapter 4 focusses on the use of the CantiClever probe in MFM. A layer of magnetic material is deposited on the side of the tip plane. Investigations using SEM showed that the tip is nicely defined, with only very little cobalt on top of the tip plane. The shape of the tip closely resembles the ideal tip shape. MFM studies of the magnetic properties of the tips on dedicated test structures showed that the tip consists of multiple magnetic domains in the as–deposited state. After an external magnetic field of 800 kA/m is applied parallel with the long axis of the tip, the domain configuration changes into a single domain state, as desired for MFM tips. The reversal behavior of the tips is studied by VSM measurements and micromagnetic simulations. The switching fields determined from VSM measurements ranged from 36 to 48 kA/m. These values show that the CantiClever tip is suitable for probe recording applications, as these values are much lower than the coercive fields of typical media used. To determine the performance of the CantiClever probe in MFM, two types of samples have been imaged using a Dimension 3100 MFM from Digital Instruments in air. The first sample was a CAMST-II reference sample. Here, magnetic details as small as 30 nm could be observed, limited by the roughness of the sample. The second sample was an experimental perpendicular hard disk sample, with written tracks of several bit lengths. On the hard disk medium, which is much more flat, bit transitions could be identified up to 1 MFCI, corresponding to a bit length of 25 nm. The measured bit length on this track was slightly larger at 27 nm.

An investigation of the possibilities of the CantiClever probe for the integration of another sensor besides an MFM tip is presented in chapter 5. A magnetoresistive element together with the electrical connections was chosen as the sensor. The absolute MR response of such a sensor has been simulated using a micromagnetic simulation package. First, a sensor with the same shape as the CantiClever tip plane has been simulated. The MR response proved to be the highest if one of the wires was connected at the ultimate tip end. It turned out that this shape was not a good choice, as the absolute MR signal, calculated for this geometry, was only $0.04\ \Omega$. To improve the MR response, the shape of the sensor has been modified by adjusting the tip radius to the desired resolution and focussing the current as close as possible to the end of the tip. These designs resulted into a higher absolute MR response of $0.24\ \Omega$. A 20 nm thick MR element has been realized on the back of the tip plane of the CantiClever probe by means of shadow evaporation of permalloy. The electrical connections to the element have been made using the deposition of platinum in an FIB system. The resistance of the total structure has been measured to be 12 kΩ. Unfortunately, no MR response could be measured when the sensor was placed in an external magnetic field. To be able to measure to response of the MR sensor, similar sensors have been made on a silicon wafer and connected with aluminum wires and bondpads. Triangular shaped sensors and sensors that resemble the optimized shape (U–shaped) obtained from the simulations have been made this way. The U–shaped sensors have been characterized using MFM, Kerr microscopy and MR measurements. The elements show a complicated domain structure at the sensing part if there is no magnetic field applied. For use as a read sensor, biasing of the element is thus required. The Kerr measurements showed very nicely the switching of the legs of the element. In MR measurements, a response of 0.27% could be obtained if the field was oriented parallel with the legs and 0.63% if the field was oriented perpendicular to the legs.

In chapter 6, the conclusions of this thesis are given and possibilities for improvements and further research are discussed.

Samenvatting

Magnetische kracht microscopie, in het Engels afgekort tot MFM, is een scanning probe techniek die gebruikt kan worden om de strooivelden boven een magnetisch sample met hoge resolutie in beeld te brengen, zonder dat het sample daar grondig voor geprepareerd hoeft te worden. Deze eigenschappen maken dat de MFM een zeer geschikt instrument is om geschreven bitpatronen in harde schijven mee te bestuderen. De datadichtheid in magnetische opslag systemen is in de afgelopen decennia enorm toegenomen. Dit heeft ervoor gezorgd, dat de grootte van de geschreven bits in moderne hard disks tegenwoordig nog maar enkele tientallen nanometers bedraagt, niet veel groter dan de resolutie die met een MFM gehaald kan worden. Als deze resolutie, die op dit moment door de geometrie van de magnetische tip wordt beperkt, niet wordt verbeterd, zal de harde schijf industrie een belangrijk instrument verliezen. In dit proefschrift wordt een nieuwe probe, geschikt voor magnetische kracht microscopie, gepresenteerd die ontworpen is om het probleem van de geometrie van de bestaande magnetische tips op te lossen. Het fabricageproces van de nieuwe probe maakt tevens de integratie van andere sensoren, anders dan een MFM tip, mogelijk.

Het eerste hoofdstuk geeft de achtergronden van het onderzoek dat in dit proefschrift is beschreven. Het gaat in op de principes en de toepassingen van verschillende scanning probe technieken, met speciale aandacht voor de magnetische kracht microscopie. Ook wordt het gebruik van scanning probe technieken voor het opslaan van data besproken.

Het onderwerp van hoofdstuk 2 is een van de belangrijkste onderdelen van de MFM: de magnetische tip. Het beeldvormingsproces in een MFM wordt beschreven en er wordt een definitie gegeven van de resolutie. Het behulp van deze theorie wordt bewezen dat met een magnetische tip, die de vorm heeft van een staafmagneetje met een plat uiteinde, de hoogst mogelijke resolutie kan worden behaald. Met behulp van berekeningen is de invloed bepaald van afwijkingen van deze ideale vorm op de te behalen resolutie. Uit deze berekeningen kan geconcludeerd worden dat een tip met een ellipsoïde vormig uiteinde een goede tip is voor MFM met een hoge resolutie. Deze tip heeft geen nulpunten in zijn overdrachtsfunctie en de resolutie die met deze tip kan worden gehaald hangt veel minder sterk af van de dikte van de tip. Hierna wordt een overzicht gegeven van de ontwikkeling van MFM tips sinds de uitvinding in 1987. Ondanks de inspanningen om goede MFM tip in massaproductie te maken, zijn de tips die per stuk, "met de hand", zijn gemaakt nog steeds beter. Aan het einde van het hoofdstuk wordt het nieuwe ontwerp voor een cantilever met een tip voor MFM, de CantiClever genaamd, gepresenteerd. Dit nieuwe ontwerp maakt massaproductie van tips met een vrijwel ideale geometrie voor MFM mogelijk. Daarnaast maakt het ontwerp ook de integratie van andere sensoren op het einde van een cantilever mogelijk.

In hoofdstuk 3 is het fabricageproces van de CantiClever probe beschreven. Dit proces wijkt op twee punten af van het proces van bestaande probes voor magnetische microscopie. Ten eerste bestaat de tip van de probe uit een silicium nitride film die met lithografische technieken is gemaakt. Bestaande probes hebben een tip die gevormd wordt door een silicium piramide, met dimensies die zijn vastgelegd door de kristalorientatie van de silicium wafer waaruit deze zijn gemaakt. Ten tweede is de silicium cantilever van de probe tijdens het fabricageproces 90° gedraaid, vergeleken met de cantilevers van bestaande probes. De cantilever en de basis (het "handvat") van de probe zijn gemaakt uit $\langle 110 \rangle$ silicium wafers door middel van een KOH nat ets proces, dat uit twee stappen bestaat. In de eerste stap worden er vensters geëtst aan de achterkant van de wafers. Hierdoor wordt de breedte van de cantilever bepaald. In de tweede ets stap, vanaf de voorkant van de wafer, worden de cantilevers uit het substraat geëtst. Met dit fabricageproces kunnen 220 probes gemaakt worden uit een 100 mm wafer, met een tipvlak dat minimaal 37 nm dik is. Het einde van de tip had een radius van ongeveer 30 nm. De kwaliteitsfactor van de cantilevers is ook gemeten, deze bedraagt ongeveer 600 in lucht en ongeveer 50000 in vacuum.

Hoofdstuk 4 gaat in op het gebruik van de CantiClever probe voor MFM. Hiertoe wordt een dunne laag magnetisch materiaal aangebracht op de zijkant van het tipvlak. Deze laag vormt de magnetische tip van de probe. Uit onderzoek met raster electronenmicroscopie blijkt dat deze magnetische tip mooi continue langs de gehele zijkant van het tipvlak loopt, en dat er slechts weinig magnetisch materiaal op de bovenkant van het tipvlak terecht komt. De vorm van de magnetische tip komt erg dicht bij de ideale vorm van een MFM tip. Bestudering van de magnetische tip met de MFM, gebruik makend van speciale teststructuren, laat zien dat de tip in de toestand direct na depositie uit meerdere magnetische domeinen bestaat. Wanneer er een magnetisch veld van 800 kA/m aangelegd wordt parallel aan de lange zijde van de tip, verandert de domeinstruktuur in een één–domein toestand. Dit is de domeinstruktuur, die voor een MFM tip gewenst is. Het magnetisatie omkeergedrag van de tips is bestudeerd aan de hand van VSM metingen en micromagnetische simulaties. De waarden van het omkeerveld varieert van 36 tot 48 kA/m. Deze waarden zijn lager dan die van media die gebruikt worden in probe recording systemen, zodat de CantiClever probe wellicht in prototypen van dergelijke systemen toegepast zal kunnen worden. Om te kijken hoe goed de nieuwe probe presteert in een MFM zijn beelden gemaakt van twee typen samples met een Dimension 3100 MFM van Digital Instruments. Het eerste sample is het zogenaamde CAMST–II referentie sample. De kleinste magnetische strukturen die op dit sample zichtbaar gemaakt konden worden, waren 30 nm groot. De relatief grote ruwheid van het sample bleek hier de beperkende faktor. Het tweede sample is een experimenteel hard disk medium met een vertikale magnetische anisotropie, waarin bitpatronen staan geschreven met verschillende bitlengtes. Dit sample is veel gladder dan het CAMST–II sample. Hierop konden dan ook bits worden onderscheiden tot een lineaire dichtheid van 1 miljoen flux overgangen per inch (1 MFCI). Dit komt overeen met een bitlengte van 25 nm. De gemeten lengte was iets groter: 27 nm.

Een onderzoek naar de mogelijkheden tot het integreren van andere sensoren naast een MFM tip op de CantiClever probe wordt gepresenteerd in hoofdstuk 5. Als sensor is gekozen voor een magnetoweerstandssensor en de bijbehorende elektrische verbindingen omdat een probe met een dergelijke sensor voor zowel microscopie als recording gebruikt kan worden. Het gedrag van een dergelijke sensor is gesimuleerd met een micromagnetisch simulatiepakket. Het uitgangspunt was een sensor met dezelfde vorm als het tipvlak van de probe. Het bleek dat een puntige sensor geen goede keuze is, omdat het signaal van deze sensor erg klein is, slechts $0.04\ \Omega$. Om het signaal te verbeteren is de vorm van de sensor zodanig veranderd dat de grootte van het einde van de tip overeenkomt met de gewenste resolutie en de stroom dichter langs het uiteinde van de tip loopt (U-vormige sensoren). Dit resulteerde in een groter uitgangssignaal van $0.24\ \Omega$. Met behulp van schadow opdampen is vervolgens een MR sensor gerealiseerd op het tipvlak van de CantiClever probe. De elektrische verbindingen zijn met focusseerde ionenbundel depositie (FIB) gemaakt. De weerstand van de sensor en de verbindingen samen was 12 kΩ. Van deze sensor kon helaas geen magnetisch uitgangssignaal worden gemeten. Om dit toch te kunnen doen, zijn soortgelijke sensoren op een silicium wafer gemaakt, aangesloten met aluminium draden. Driehoekige sensoren en U-vormige sensoren, bepaald aan de hand van de simulaties, zijn zo gemaakt. De U-vormige sensoren zijn onderzocht met MFM, Kerr microscopie en MR metingen. De sensoren hebben een ingewikkelde domeinstruktuur wanneer er geen extern magnetisch veld wordt aangelegd. Om ze als lees–sensor te gebruiken moeten er een magnetisch bias veld worden aangelegd. De Kerr metingen laten prachtig het omkeren van de "benen" van de sensor zien. Een uitgangssignaal van 0.27% kon worden gemeten als het veld parallel aan de benen werd aangelegd en 0.63% wanneer dit loodrecht op de benen werd aangelegd.

In hoofdstuk 6 worden tenslotte de conclusies van dit proefschrift gegeven en worden enkele aanbevelingen gedaan voor verder onderzoek.

Acknowledgements

Throughout my Ph.D. project I had the pleasure of working with numerous people who contributed in one way or another to my research. The cooperation with all those people has had a positive influence on my work, and I think this thesis is a better one because of it. Here, I would like to express my gratitude to all those people.

First of all, I would like to thank Cock Lodder for being my promotor. His enthusiastic lecture on "Microtechnologie ten behoeve van transducenten" was one of the main reasons for doing my graduation project in the SMI group. Later on, he encouraged me to become a Ph.D. researcher. The monthly discussions during my project helped me to put the daily issues aside and maintain the necessary overview to stay on track.

I especially would like to thank Leon Abelmann for his daily supervision. He was always willing to generate new ideas and helping me to find solutions to my problems, despite his very busy, electronically maintained, schedule. The Abelmann helpdesk was always online, which proved very helpful to get last minute issues solved in time. Being his first Ph.D. student, I hope that many more will follow and have the same pleasant learning experience I had.

I gladly acknowledge the financial support of the Dutch Technology Foundation (STW), and I would like to thank the members of the STW user committee for the annual discussions.

The work of Andre van Dijk provided me with a good starting point for my Ph.D. project. Since then, many more people contributed to my work who I would like to thank: Tomohiro Okada for his work on deposition of the MR sensor on the tip plane. Takehito Shimatsu for providing the experimental hard disk samples that allowed us to explore the limits of our MFM tips. Klaus Ramstöck for his micromagnetic simulations of the MR sensors and valuable comments on my thesis. Hitoshi Saito for his calculations of the tip shapes and support with Mathematica. Bogdan Craus for his work on the waferscale MR elements. Siebe

Berveling for the measurements of the mechanical properties of the cantilevers. I especially would like to thank Alexander le Fèbre for all his efforts into the test structures during his graduation project and his help with the processing of the final CantiClevers. Alexander, I hope that you can enjoy your work at the SMI group as a Ph.D. researcher as much as I did, now that the tedious CantiClever processing is nearly finished.

This research contains a lot of practical work, most of it carried out in the MESA$^+$ cleanroom. I therefore would like to thank the members of the cleanroom staff for their support and advice. Furthermore, I would like to thank all the people who contributed to the practical work: First of all Iwan Heskamp, the cleanroom magician, for sharing his cleanroom skills and secrets and making waiting for processes to finish less boring. Meint de Boer and Erwin Berenschot for their help with the development of the fabrication process. Ferdi Meijer for his help with the FIB etching. Wim Geerts for the Kerr microscopy images of the MR sensors. And finally Mark Smithers for the beautiful SEM images.

As this thesis is about sensors for magnetic imaging, there should be at least one person brave enough to try to use them. This person is Martin Siekman. In the beginning, he was willing to spend long friday afternoons and sometimes nights behind the MFM to try to get some sort of signal from them. Later on, he pushed hard to try to show that our tips were the best. Martin, thanks for everything!

Since I started working in the group of Cock Lodder, many things changed, even its name. The one thing that hasn't changed is the pleasant and informal atmosphere. I would like to thank all the present and past SMI group members for making working in the SMI group a very enjoyable experience for me. Part of the pleasant experience is certainly due to my roommates Ferry Postma and Mathieu Bolks, who also provided me with last minute comments on this thesis. I would like to thank Thijs Bolhuis for all his help around the lab and keeping my PC in shape. Finally I would like to thank Casper Doppen for his very nice photograph of the CantiClevers and helping me design the cover of this thesis.

In het tot stand komen van dit proefschrift hebben niet alleen collega's en vrienden een belangrijke rol gespeeld. Ik wil dan ook Ellen hartelijk danken voor alle steun tijdens mijn promotieonderzoek en met name in de laatste fase. Mijn ouders hebben het mogelijk gemaakt dat ik mijn studie kon volgen en deze heb kunnen afsluiten met dit promotieonderzoek. Ik wil hen daarvoor hartelijk bedanken. Ten slotte wil ik de rest van mijn familie bedanken die mij tijdens mijn studie en promotieonderzoek hebben gesteund.

About the author

Arnout van den Bos was born on december 10, 1974 in Oosterhout (NB) and grew up in Apeldoorn. He graduated in 1993 from the ″Gymnasium″ of the ″Christelijk Lyceum Apeldoorn″. At the University of Twente, he studied Electrical Engineering. During his study, he spent four months at Robert Bosch GmbH in Reutlingen, Germany, as a practical training, where he got his first hands–on experience with cleanroom work. Back in the Netherlands, he did his graduation project in the group of Cock Lodder. After summarizing this work in the thesis: ″Development of a patterning process for magnetic thin films″ he received his Master of Science (ir.) degree in 1999. He continued to work in the SMI group of Prof. Lodder as a Ph.D. researcher in the project ″Magnetic field probe microscope for research, development and production of magnetic recording media and heads″ funded by STW. His work involved the development of a new type of probe for magnetic imaging, and is concluded with this thesis.

List of publications

Articles

- A.G. van den Bos, A.C.J. van Dijk, I.R. Heskamp, L. Abelmann and J.C. Lodder, "A New Concept in Magnetic Force Microscope Cantilevers", *Magnetic Storage Systems Beyond 2000*, volume 41 of the NATO Science Series II: Mathematics, Physics and Chemistry, pages 307–312 (Kluwer 2001).
- A.G. van den Bos, I.R. Heskamp, M.H. Siekman, L. Abelmann and J.C. Lodder, "The CantiClever: A Dedicated Probe for Magnetic Force Microscopy", *IEEE Trans. Magn.* **38** (5), pages 2441–2443 (2002).
- H. Saito, A.G. van den Bos, L. Abelmann and J.C. Lodder, "High–resolution MFM: Simulation of tip sharpening", *IEEE Trans. Magn.* **39** (5), pages 3447–3449 (2003).

Accepted articles

- L. Abelmann, A.G. van den Bos and J.C. Lodder, "Magnetic Force Microscopy - Towards higher resolution", *Magnetic Microscopy of Nanostructures*, H.P. Oepen ed.
- A.G. van den Bos, A.J. le Fèbre, H. Saito, K. Ramstöck, M.H. Siekman, L. Abelmann and J.C. Lodder, "High resolution magnetic tips and integrated multi–wire probes for scanning probe microscopy", *Proceedings of the 12th International Conference on Scanning Tunneling Microscopy / Spectroscopy and Related Techniques (STM'03).*

Patents

- A.G. van den Bos, L. Abelmann and J.C. Lodder, "Probe en werkwijze voor de vervaardiging van een dergelijke probe", patent number: PCT NL02/00842, filed on December 21, 2001.

Presentations

- A.G. van den Bos, A.C.J. van Dijk, I.R. Heskamp, L. Abelmann and J.C. Lodder, ”A New Concept in Magnetic Force Microscope Cantilevers”, NATO/ASI Magnetic Storage Systems Beyond 2000 (2000), poster presentation.

- A.G. van den Bos, I.R. Heskamp, L. Abelmann and J.C. Lodder, ”A New Concept in Magnetic Force Microscope Cantilevers”, Dutch Scanning Probe Day (2000), poster presentation.

- A.G. van den Bos, I.R. Heskamp, M.H. Siekman, L. Abelmann and J.C. Lodder, ”The CantiClever: a dedicated probe for magnetic force microscopy”, Intermag 2002, oral presentation.

- A.G. van den Bos, M.H. Siekman, L. Abelmann and J.C. Lodder, ”The CantiClever: a dedicated probe for magnetic force microscopy”, IMST2002 (2002), poster presentation.

- A.G. van den Bos, T. Okada, M.H. Siekman, L. Abelmann and J.C. Lodder, ”Integrated multi–wire probes based on the CantiClever concept”, Dutch Scanning Probe Day (2002), oral presentation.

- A.G. van den Bos, A.J. le Fèbre, H. Saito, K. Ramstöck, M.H. Siekman, L. Abelmann and J.C. Lodder, ”High resolution magnetic tips and integrated multi–wire probes for scanning probe microscopy”, STM’03 (2003), poster presentation.

- A.G. van den Bos, ”CantiClever: a new way to produce cantilevers for scanning probe microscopy”, oral presentation at the MESA$^+$ colloquium on June 17, 2003.